Advanced polymer-based microfabricated neural probes using biologically driven designs

by

John P. Seymour

A dissertation submitted in partial fulfillment
of the requirements for the degree of
Doctor of Philosophy
(Biomedical Engineering)
in The University of Michigan
2009

Doctoral Committee:
Professor Daryl R. Kipke, Chair
Emeritus Professor David J. Anderson
Professor Khalil Najafi
Associate Professor Joerg Lahann
Associate Professor Shuichi Takayama

DEDICATION

For my wife, Jeni, who has lovingly, optimistically endured a true test of faith

ACKNOWLEDGMENTS

First, I want to thank my family. My parents worked hard to give me more options than they had. Congratulations, Mom and Dad. Pride and love of family has motivated and grounded me. I cannot recall my folks saying “work hard”, “be honest” but that is the example they always set for me. I cannot help but say the Seymour’s, Smiley’s, Emch’s, and Diamond’s are the folks that make this world so incredibly wonderful. Thank you.

Next, I have to thank my undergraduate research advisor, Dr. Mardi Hastings. Your faith in my ability and words of admonishment were the seeds that grew into this endeavor. Without those few words I would have never dreamed of the possibility.

All the important things one might want in an advisor, a recognized voice in science, money to see a project through, and the self-confidence to let his/her students think independently, my advisor provided. I also want to thank my advisor for believing in these ideas before anyone else. It goes without saying, these would never have seen fruition if it were not for his vision and trust.

I’d also like to thank my committee members, Dr. Anderson, and Dr. Lahann, Dr. Najafi, and Dr. Takayama. Convincing one smart person that you have matured into a productive scientist is plausible; convincing five is a great source of pride and self-confidence. So thank you for your time and effort.

There are many individuals in the Neural Engineering Lab I would like to thank. Kip Ludwig, Jey Subbaroyan, Matt Gibson, Nick Langhals, Hirak Parikh, Erin Purcell, Matt Johnson, Greg Gage, Tim Marzullo, Eugene Daneshvar, Mohammad Abidian, “TK” Yoshida, Pratik Rohatgi, Taegyun Moon, Mike Joseph, Azadeh Yazdan, and Rachel Miriani—to each of you, thank you. Kip was a sounding board and voice of reason. Jey

was a true friend. Matt was a confidant and comrade. Nick was a collaborator and more than anyone makes the NEL run smoothly. The NEL was the physical vehicle for my progress and those friends, colleagues were the metaphysical. Also, a debt of gratitude to the previous generation of NELers—Ruben, Dave, Rio, Otto, Liz, Tim, and Justin who motivated us to succeed by example. To Ruben Rathnasingham a special thanks, because you always gave an encouraging word and the time to help when I was my most desperate. To Dave Pellinen, many thanks for sharing your microfabrication expertise and patient training.

Over the years I've been fortunate to have undergraduates and graduates help along the way. Many thanks to Luis Salas, David Sullivan, Joshua Jackson, Tanmay Aggarwal, Marc Kaplan, and Samana Ghimire for their technical assistance in a variety of tasks.

Finally and foremost, I want to thank my wife, Jeni. I asked you to sell our house, quit a great job, and take off with me into the unknown. While every married graduate student will naturally thank their spouse, you deserve so much more and I hope to express it over the years to come. No song or poem could adequately convey my joy and gratitude, but, it will be worth trying.

TABLE OF CONTENTS

LIST OF FIGURES

LIST OF APPENDICES

ABSTRACT

This research presents new designs and materials for neural recording and stimulation technology. Greater electrode density is enabling neuroscientists to study larger neuronal populations, but even higher signal stability and electrode density are needed. Addressing these issues is critically important for neuroprostheses in the treatment of spinal cord injury, ALS, or limb loss. Stimulating electrodes have already improved quality of life for those with Parkinson's and dystonia and this technology has many new indications on the horizon. Smaller stimulating electrodes with reduced glial encapsulation would reduce the power requirements of these applications. I will discuss how our research impacts neurotechnology by enabling reduced glial encapsulation, greater design options, and improved electrical insulation.

Our first study introduced a novel neural probe with reduced chronic cellular encapsulation. We hypothesized that if a structural feature size is smaller than a reactive cell body (<7 μm), the resulting encapsulation would be mitigated by the prevention of cellular spreading. We investigated this relationship between size and tissue reactivity using a microfabricated parylene structure. Probes were implanted in the rat neocortex for four weeks followed by histological analysis. We found the non-neuronal density around the sub-cellular feature was less than half of that around the probe shank.

The objective of our second study was to identify a parylene process that would enable long-term bioelectrical insulation. We contrasted parylene-C with an alternative parylene material using electrical and mechanical tests. We present a reactive parylene (complementary layers of PPX-CHO and PPX-CH_2NH_2) that can be used in conjunction with parylene-C but has improved electrical insulation and wet metal adhesion.

In our third study, a new parylene-based microfabrication process is presented for neural recording, stimulation, and drug delivery applications. We introduce a large design space for electrode placement and structural flexibility with a six mask process. By using chemical mechanical planarization, electrodes may be created top-side, back-side, or on edge having three sides. Poly(3,4-ethylenedioxythiophene) (PEDOT) modified edge electrodes having an 85 μm^2 footprint (smallest reported to date) resulted in an impedance of 200 kΩ at 1kHz. Edge electrodes successfully recorded single unit activity in acute animal studies.

CHAPTER 1 Introduction

1.1 Overview

Neuroscience research, neuroprostheses, and neuromodulation are driven by the set of engineering tools we collectively call neurotechnology. Research on the sensors, actuators, packaging, and communication technology that encompass neurotechnology is progressing rapidly in both academia and industry. The research presented here focused on the distal end of neurotechnology—the neural device-tissue interface. We sought to improve this interface by discovering materials and designs that maximized function in neural recording and stimulating devices. Our research regarding novel device geometry and material selection can also be applied to drug delivery (Pathan, Iqbal et al. 2009) or chemical sensing (Dale, Hatz et al. 2005) devices in the brain. In fact, these issues are equally relevant in the peripheral nervous system (Branner, Stein et al. 2004) and in completely different modalities, e.g. biosensors (Gilligan, Shults et al. 2004), that share the common denominator of a microscale electrode interfacing tissue. Chronic, implantable microelectrode devices share two fundamental needs: (1) the mitigation of cellular and acellular encapsulation which reduces device sensitivity over time, and (2) the long-term electrical viability of the sensor or actuator itself. Our research provides potential solutions to these two abiding problems at least in the context of microfabricated neural probes and hopefully beyond.

1.2 Neurotechnology Applications

Understanding the broad applications of neurotechnology is necessary to judge the relevance and scope of our research into the neural device-tissue interface. Neurotechnology was once the sole domain of neuroscientists before it became embraced by technologists from all fields. Now entrepreneurs are pushing the limits of its application and making neurodevices one of the fastest growing sectors in healthcare (22% growth rate in 2007) (NeuroInsights 2008). Two driving forces behind the current advancement of neurotechnology are as follows: (1) fundamental neuroscience and disease-specific research is making exponential improvements in our understanding of what is the single, most complex system in science; and (2) the healthcare challenge of treating neurologic disease is increasing due to changing demographics and better treatment of simpler disease models (e.g. cardiac, vasculature disease). This combination of opportunity and demand has sparked a rapid growth of research and investment into neuromodulation, neuroprostheses, and neuroscience (Fig. 1.1).

In neuromodulation applications, most clinical devices use electrical stimulation to act on cell bodies, nerves, and muscles. Neuromodulation, also called neurostimulation, is currently FDA approved for therapeutic applications in the treatment of Parkinson's, dystonia, and pain management. New indications are growing and those in clinical trials in 2007 include cluster headaches, epilepsy, depression, obesity, Tourette syndrome, and drug addiction (Sakas, Simpson et al. 2007). Neuromodulation devices have either external or implanted electrodes. The two common external electrode methods are

electromuscular stimulation (EMS) and transcutaneous electrical nerve stimulation (TENS), which both use external electrodes. Deep brain, spinal cord, and vagus nerve stimulation rely on implanted electrodes. For external type electrodes, there are a number of energy sources that are being considered and include optical (Zhang, Aravanis et al. 2007), ultrasonic (Tyler, Tufail et al. 2008), and magnetic (Wagner, Valero-Cabre et al. 2007). The great challenge of neuromodulation is to understand how it impels beneficial effects in a given application (Sakas, Simpson et al. 2007).

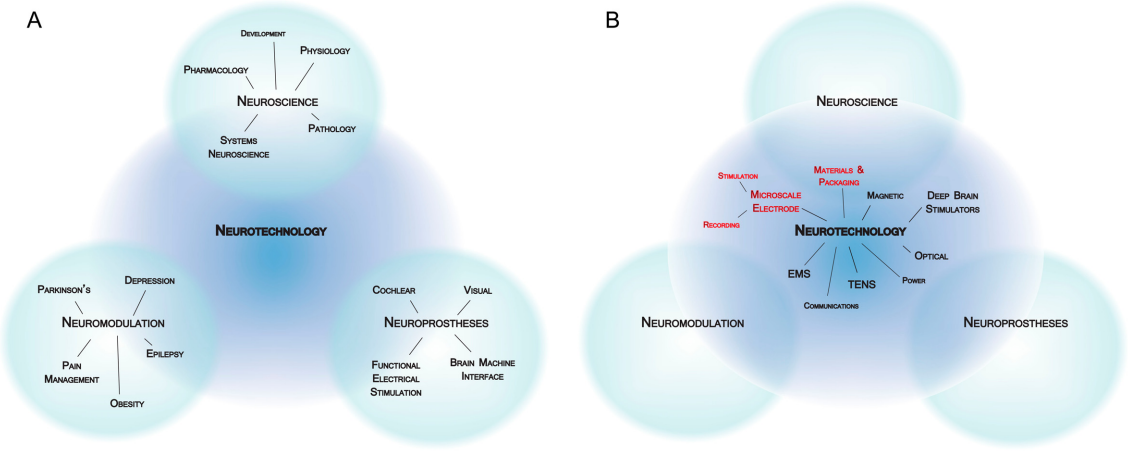

Figure 1.1. (A) Neurotechnology applications space. (B) Neurotechnology design space employs an array of engineering tools. Microscale electrodes and materials are the focus of this thesis (shown in red).

Our research is relevant to neuromodulation using implantable electrodes in chronic applications because changes at the device-tissue interface over time affects performance. Given that tissue encapsulation increases the electrical impedance, higher current is needed to have the same therapeutic effect (Grill WM 1994; Grill and Mortimer 1998).

This may be mitigated with larger electrodes but at the cost of tissue damage during insertion and spatial selectivity. Also, the power dispensation with a larger current has direct implications on device lifetime. In Chapter 2 we present a design that mitigates tissue encapsulation and so may provide a preferable solution.

Neurotechnology in the form of neuroprosthetic devices provide augmentation to lost neurologic function. Neuroprostheses can achieve augmentation with either functional electrical stimulation (FES) or electrophysiological sensing. FES refers to techniques that replace natural nerve functions with electrical stimulations. Examples of FES include cochlear ear implants that assist individuals with hearing impairment (McCreery, Lossinsky et al. 2007) and electrical impulses to allow shoulder and elbow movement in quadriplegic patients (Hincapie and Kirsch 2009). Electrophysiological sensing monitors signals from surviving nerve endings in an amputee, for example, where the signal is used to activate a prosthetic limb. The most intriguing example of electrophysiological sensing is the brain-machine interface (BMI) where implantable microelectrodes record neural activity in the brain (either single cell or population signals, i.e. local field potentials) to sense the intention of movement (Fig. 1.2). These control signals are then used to drive any number of actuators, from an on-screen cursor to a motorized wheelchair. Implantable neural prostheses that allow for the augmentation of lost limb movement damaged by ALS, spinal cord injury, stroke, or amputation have recently made progress in human clinical trials (Bartels, Andreasen et al. 2008; Truccolo, Friehs et al. 2008).

Figure 1.2 A brain-machine interface device implanted into a human with tetraplegia. A version of the "Utah" array developed by Cyberkinetics and implanted for one year was used to create a "neural cursor". (Images taken from Hochberg et al. 2006, their Figure 1).

The common technological denominators of neuromodulation and neuroprostheses are electrodes (either implanted or external), an energy source, electronic control, and packaging. The device-tissue interface is a critical junction in applications using implanted microelectrode because of the inherent limitations (discussed in section 1.4). New modalities such as ultrasound, magnetic, and optical are attractive because they can function beyond the local tissue interface but cannot, as of yet, replace the spatial selectivity of the microelectrode.

1.3 Review of Microelectrodes

Microwires were the first microelectrodes and have been an effective research tool at least since they were introduced into hibernating squirrels to collect chronic neural signals (Strumwasser 1958). Microwires have evolved into stereotrodes and tetrodes (Buzsaki and Draguhn 2004) with a variety of insulating and conductor materials that

vary depending on the recording or stimulation requirements. The first major advancement in microelectrode technology was the pioneering work of Kensall Wise at Stanford (Wise, Angell et al. 1970) and later at the University of Michigan that developed the microfabricated silicon electrode array. Photolithographic techniques were applied for unprecedented geometric precision of electrode design, and the "dissolved wafer process" created needle-like structures ideal for minimal tissue damage. This core technology became known in the field as the "Michigan" array and has evolved over the years to include integrated interconnects (Hetke, Lund et al. 1994), active electronics (Wise, Anderson et al. 2004), cochlear implants (Wans, Gulari et al. 2005), polytrodes (Blanche, Spacek et al. 2005), and three dimensional arrays (Ying, Gulari et al. 2007) just to name a few. The large design space afforded by a microfabricated device have enabled many basic neuroscience experiments that could not have been conducted otherwise because of the electrode density and geometric precision (Wise, Sodagar et al. 2008).

Besides microwires and the "Michigan" probe, another probe technology that has shaped the field of microelectrodes is the "Utah" array originally developed by Richard Normann at the University of Utah (Campbell, Jones et al. 1991). The "Utah" array is fabricated as an array of tines machined from a block of silicon. These tines are then anisotropically etched and doped to form an array of conductive needles. The manufacturing is not photolithographic in nature so each tine can correspond with only one electrode, but this alternative design provides a unique set of mechanical properties. More recently, this technology has been the basis of human trials using a brain machine interface (Donoghue,

Nurmikko et al. 2007) and is being adapted for wireless integration (Kim, Bhandari et al. 2008).

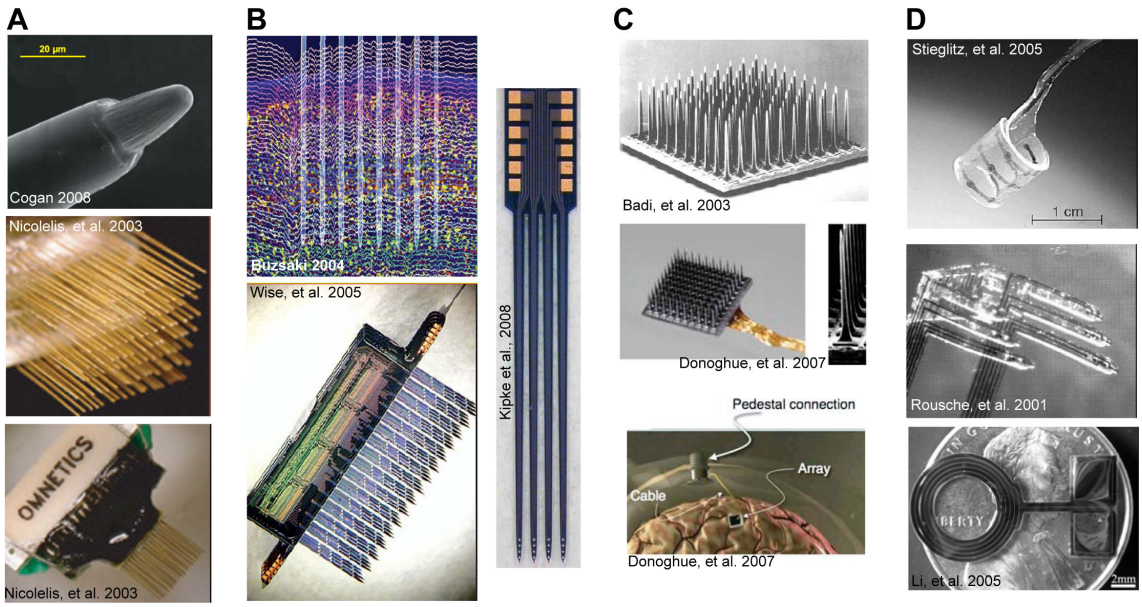

Figure 1.3 Example microelectrode technology of (A) microwires, (B) "Michigan" devices, (C) "Utah" arrays, and (D) polyimide and parylene devices.

Polymer-based neural probes have had limited impact on microelectrode technology since there has been little use by neuroscientists. Whether the lack of "technology acceptance" is an issue of supply or quality is not clear. Polyimide microelectrode arrays have been fabricated by several groups (Stieglitz and Meyer 1999; Rodriguez, Ceballos et al. 2000; Rousche, Pellinen et al. 2001) with limited data on functional performance. In a recent example, a polyimide device was tested alongside a Michigan array and found it to have 'comparable results' in an 8 week test, although no data on signal amplitude, number of single units, or noise levels was presented (Cheung 2007). A few groups have

fabricated parylene-based neural probes. Microfluidic neural probes were designed and verified as functional in an acute surgery (Takeuchi, Ziegler et al. 2005). Y.C. Tai's group at the California Institute of Technology has contributed greatly to parylene-C microfabrication techniques and has developed a retinal stimulation platform (Li, Rodger et al. 2005; Rodger and Tai 2005; Weiland, Fink et al. 2005). This group provides the only long-term electrical soak testing of a polymer neural device in publication. Direct current (DC) accelerated soak tests of a parylene insulated radio frequency coil measured transverse resistance (i.e. through the parylene and not along the interfacial plane of the device) (Li, Rodger et al. 2005). They discovered that heating at 200°C in a vacuum oven for 2 days greatly improved resistivity and longevity. We also tested the heat treatment of parylene structures in Chapter 4 with results that partly agreed with the findings of Li and colleagues. We believe our experimental design using lateral impedance measurements over a broad spectrum range adds to the understanding regarding parylene-C microfabricated bioelectrical sensors.

1.4 Microelectrode Performance and Tissue Response

The chronic performance of each probe technology has been well characterized and with similar results. "Michigan", "Utah", and microwire arrays have each had at least one published example of long-term performance with little degradation over time (Taylor, Tillery et al. 2002; Vetter, Williams et al. 2004; Suner, Fellows et al. 2005). Most experiments, however, report mixed results. The "Michigan" arrays have been extensively used in the rat model and typically show a performance decline by two

months (Kipke, Vetter et al. 2003; Schwartz 2004; Ludwig, Uram et al. 2006; Otto, Johnson et al. 2006). The "Utah" array has had greater use in large animal models such as cat and monkey but has also shown declining performance in long-term studies (Rousche and Normann 1998; Maynard, Fernandez et al. 2000; Branner, Stein et al. 2004). Microwires also show heterogeneity in recording performance (Schmidt, Bak et al. 1976; Schwartz 2004; Liu, McCreery et al. 2006), including wire to wire heterogeneity within the same bundle (Schmidt, McIntosh et al. 1988; Williams, Rennaker et al. 1999). Brain-machine interfaces in human patients were only efficacious over a short period of time (Kennedy and Bakay 1998; Hochberg, Serruya et al. 2006; Donoghue, Nurmikko et al. 2007), although a more recent patient is performing well after a year with a modified version of the Utah array (Truccolo, Friehs et al. 2008).

In summary, microelectrode recording performance does not always work long-term, but it is an oversimplification to state that performance will always falter. Day to day variation in neural activity may be as much of issue as longevity in the neural interface. Instability is cited as a critical challenge of a BMI technology (Donoghue, Nurmikko et al. 2007) and similarly in cats (Liu, McCreery et al. 1999; Liu, McCreery et al. 2006). Instability may have the same underlying failure mechanism as limited longevity. The challenge for device designers is clear, even if the degree of importance is debatable: increase the quality, consistency, and longevity of the neural recordings.

Research of the reactive tissue response to implantable probes began thirty years ago and has continued to progress (Stensaas and Stensaas 1978; Edell, Toi et al. 1992; Turner,

Shain et al. 1999; Szarowski, Andersen et al. 2003; Biran, Martin et al. 2005). Tissue encapsulation of the probe coupled with neuronal death in the vicinity of the recording electrode have been implicated as two important factors negatively impacting the stability and longevity of long-term neural recordings (Szarowski, Andersen et al. 2003; Biran, Martin et al. 2005). Another factor hypothesized to affect recording longevity is neuronal silencing (Merrill and Tresco 2005) , which is the cessation of spiking activity from a given neuron in response to either the initial trauma of insertion or glial hypertrophy (astrocytes) and reactivity (microglia). A difficulty of conducting and interpreting research of reactive tissue response is the number of variables likely to influence the tissue response. The mechanical properties of the device, the location of implant, material properties, surgical technique, and animal model can all be implicated as influencing biocompatibility.

Approaches to improve the neural device-tissue interface are numerous and reviewed in section 2.1. Our own published work (Seymour and Kipke 2007) discussed an approach based on a novel geometry of the neural device, research that also contributed to the general understanding of the tissue response by providing greater spatial detail and quantification. More recent unpublished work that I performed in collaboration with Erin Purcell, Chris Bjornsson (Rensselaer Polytechnic Institute) and Jey Subbaroyan shows rich spatial detail of a fully intact “Michigan” array after 18 months in a guinea pig (Fig. 1.4). The probe was left in place and sectioned parallel to the face. Immunohistochemistry and multi-photon or confocal microscopy allowed us to image

cellular structure when sampling in fine increments from healthy tissue to the intact electrode interface. From this approach, two aspects of the device-tissue interface can be analyzed with greater accuracy—(1) the morphological change of encapsulating cells as a function of distance from the interface and (2) local cellular heterogeneity from electrode to electrode (Fig. 1.4). Stark differences of encapsulation density were measurable from electrode to electrode in our analysis. In one animal, we counted as few as 22 cells in a 25 µm radius from an electrode and as many as 99 in another. This preliminary data suggests that a direct correlation between electrode performance and local tissue response is both possible and desirable.

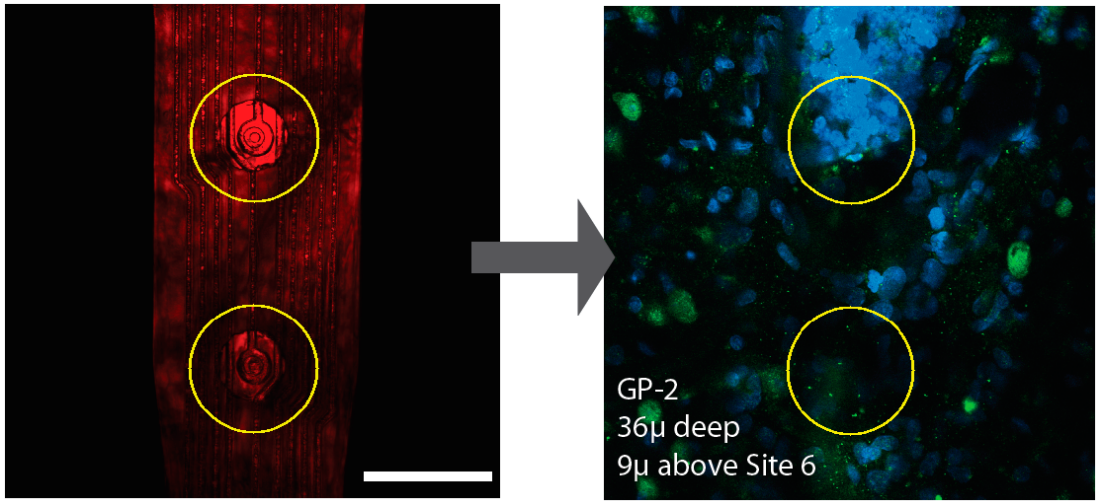

Figure 1.4. Confocal microscopy of an intact "Michigan" neural probe in a guinea pig after 18 months. (A) Reflective mode image of the device embedded in tissue. Yellow circle defines a 25 µm radius from center of electrode. (B) Confocal image of same location and 9 µm above the bottom site, Site 6. Notice heterogeneity of cellular density.

1.5 Scope of This Research

The overarching theme of the research presented in this dissertation was the design and microfabrication of neural probes that address the issue of reliable long-term sensing in the brain. A sub-theme became the use of parylene-C because of its accepted biocompatibility and ease of microfabrication. This work provides new device designs driven in large part by the biological response discussed in Chapter 2. The aims of this work were defined as follows including references to the resulting academic presentations and publications:

Aim 1. Design, fabricate, and evaluate sub-cellular neural probe geometry for reduced cellular encapsulation. (Seymour and Kipke 2006; Seymour and Kipke 2007)

Aim 2. Evaluate the interfacial and bulk electrical properties of parylene-C versus reactive parylene materials to be used in an implantable microfabricated sensor. (Seymour, Chen et al. 2008; Seymour, Elkasabi et al. In Preparation)

Aim 3. Develop a parylene-based technology platform that enables greater design space for neural probes, including implementation of the sub-cellular edge electrode. (Seymour, Langhals et al. 2008; Seymour, Langhals et al. In Preparation)

Based on our original hypothesis regarding probe geometry and results from Aim 1, we sought to develop a technology platform in Aim 3 that met these design rules:

- Physically displace the electrode sites from the large penetrating shank
- Minimize the electrode and surround substrate to achieve sub-cellular dimensions to reduce cellular adhesion
- Reduce the transfer of mechanical tethering forces from probe to tissue through flexible components of the probe
- Maintain adequate stiffness in the shank for straight insertion through the pia mater
- Provided high quality long-term electrical insulation to minimize noise

In an effort to execute these design principles we chose to develop a functional parylene-based neural probe. Parylene was originally chosen for its biocompatibility, mechanical flexibility (Young's modulus of 3 GPa compared to 150 GPa for silicon), ease of microfabrication, and many other desirable qualities (see section 4.1). Aim 2 was defined to address concern over the insulation properties of parylene-C. This work contrasted parylene-C with reactive parylene films developed in the laboratory of Joerg Lahann at the University of Michigan (Chen, McClelland et al. 2008). Using mechanical and electrical soak tests we discovered the reactive parylene indeed had better electrical insulation (Chapter 3). With the core insulation and metallization layers chosen, we could then proceed with microfabrication of our novel sub-cellular edge electrode and neural probe design. Aim 3 also required we solve several new technical problems related to the creation of a double-sided electrode in parylene. Chapter 4 describes our implementation of the sub-cellular edge electrode and variety of other designs that naturally arise from this novel process. A conclusion to this body of work and future directions are provided in Chapter 5.

References

Bartels, J., D. Andreasen, et al. (2008). "Neurotrophic electrode: method of assembly and implantation into human motor speech cortex." J Neurosci Methods **174**(2): 168-76.

Biran, R., D. C. Martin, et al. (2005). "Neuronal cell loss accompanies the brain tissue response to chronically implanted silicon microelectrode arrays." Exp Neurol **195**(1): 115-26.

Blanche, T. J., M. A. Spacek, et al. (2005). "Polytrodes: high-density silicon electrode arrays for large-scale multiunit recording." J Neurophysiol **93**(5): 2987-3000.

Branner, A., R. B. Stein, et al. (2004). "Long-term stimulation and recording with a penetrating microelectrode array in cat sciatic nerve." IEEE Trans Biomed Eng **51**(1): 146-57.

Buzsaki, G. and A. Draguhn (2004). "Neuronal oscillations in cortical networks." Science **304**(5679): 1926-9.

Campbell, P. K., K. E. Jones, et al. (1991). "A silicon-based, three-dimensional neural interface: manufacturing processes for an intracortical electrode array." IEEE Trans Biomed Eng **38**(8): 758-68.

Chen, H.-Y., A. A. McClelland, et al. (2008). "Solventless adhesive bonding using reactive polymer coatings." Analytical chemistry **80**(11): 4119-4124.

Cheung, K. C. (2007). "Implantable microscale neural interfaces." Biomed Microdevices **9**(6): 923-38.

Dale, N., S. Hatz, et al. (2005). "Listening to the brain: microelectrode biosensors for neurochemicals." Trends Biotechnol **23**(8): 420-8.

Donoghue, J. P., A. Nurmikko, et al. (2007). "Assistive technology and robotic control using motor cortex ensemble-based neural interface systems in humans with tetraplegia." J Physiol **579**(Pt 3): 603-11.

Edell, D. J., V. V. Toi, et al. (1992). "Factors influencing the biocompatibility of insertable silicon microshafts in cerebral cortex." IEEE Trans Biomed Eng **39**(6): 635-43.

Gilligan, B. C., M. Shults, et al. (2004). "Feasibility of continuous long-term glucose monitoring from a subcutaneous glucose sensor in humans." Diabetes Technol Ther **6**(3): 378-86.

Grill WM, M. J. (1994). "Electrical properties of implant encapsulation tissue." Ann Biomed Eng **22**: 22-23.

Grill, W. M. and J. T. Mortimer (1998). "Stability of the input-output properties of chronically implanted multiple contact nerve cuff stimulating electrodes." IEEE Trans Rehabil Eng **6**(4): 364-73.

Hetke, J. F., J. L. Lund, et al. (1994). "Silicon ribbon cables for chronically implantable microelectrode arrays." IEEE Transactions on Biomedical Engineering **41**(4): 314-21.

Hincapie, J. G. and R. F. Kirsch (2009). "Feasibility of EMG-based neural network controller for an upper extremity neuroprosthesis." IEEE Trans Neural Syst Rehabil Eng **17**(1): 80-90.

Hochberg, L. R., M. D. Serruya, et al. (2006). "Neuronal ensemble control of prosthetic devices by a human with tetraplegia." Nature **442**(7099): 164-71.

Kennedy, P. R. and R. A. Bakay (1998). "Restoration of neural output from a paralyzed patient by a direct brain connection." Neuroreport **9**(8): 1707-11.

Kim, S., R. Bhandari, et al. (2008). "Integrated wireless neural interface based on the Utah electrode array." Biomed Microdevices.

Kipke, D. R., R. J. Vetter, et al. (2003). "Silicon-substrate intracortical microelectrode arrays for long-term recording of neuronal spike activity in cerebral cortex." IEEE Trans Neural Syst Rehabil Eng **11**(2): 151-5.

Li, W., D. Rodger, et al. (2005). "Integrated Flexible Ocular Coil for Power and Data Transfer in Retinal Prostheses." Conf Proc IEEE Eng Med Biol Soc **1**(1): 1028-1031.

Liu, X., D. B. McCreery, et al. (2006). "Evaluation of the stability of intracortical microelectrode arrays." IEEE Trans Neural Syst Rehabil Eng **14**(1): 91-100.

Liu, X., D. B. McCreery, et al. (1999). "Stability of the interface between neural tissue and chronically implanted intracortical microelectrodes." IEEE Transactions on Rehabilitation Engineering **7**(3): 315-26.

Ludwig, K. A., J. D. Uram, et al. (2006). "Chronic neural recordings using silicon microelectrode arrays electrochemically deposited with a poly(3,4-ethylenedioxythiophene) (PEDOT) film." J Neural Eng **3**(1): 59-70.

Maynard, E. M., E. Fernandez, et al. (2000). "A technique to prevent dural adhesions to chronically implanted microelectrode arrays." J Neurosci Methods **97**(2): 93-101.

McCreery, D., A. Lossinsky, et al. (2007). "Performance of multisite silicon microprobes implanted chronically in the ventral cochlear nucleus of the cat." IEEE Trans Biomed Eng **54**(6 Pt 1): 1042-52.

Merrill, D. R. and P. A. Tresco (2005). "Impedance characterization of microarray recording electrodes in vitro." IEEE Trans Biomed Eng **52**(11): 1960-5.

NeuroInsights (2008). Neurotechnology Industry 2008 Report: Drugs, Devices and Diagnostics for the Brain and Nervous System. San Francisco, NeuroInsights.

Otto, K. J., M. D. Johnson, et al. (2006). "Voltage pulses change neural interface properties and improve unit recordings with chronically implanted microelectrodes." IEEE Trans Biomed Eng **53**(2): 333-40.

Pathan, S. A., Z. Iqbal, et al. (2009). "CNS drug delivery systems: novel approaches." Recent Pat Drug Deliv Formul **3**(1): 71-89.

Rodger, D. C. and Y. C. Tai (2005). "Microelectronic packaging for retinal prostheses." IEEE Eng Med Biol Mag **24**(5): 52-7.

Rodriguez, F. J., D. Ceballos, et al. (2000). "Polyimide cuff electrodes for peripheral nerve stimulation." J Neurosci Methods **98**(2): 105-18.

Rousche, P. J. and R. A. Normann (1998). "Chronic recording capability of the Utah Intracortical Electrode Array in cat sensory cortex." Journal of Neuroscience Methods **82**(1): 1-15.

Rousche, P. J., D. S. Pellinen, et al. (2001). "Flexible polyimide-based intracortical electrode arrays with bioactive capability." IEEE Trans Biomed Eng **48**(3): 361-71.

Sakas, D. E., B. A. Simpson, et al. (2007). Operative neuromodulation. Wien New York, Springer.

Schmidt, E. M., M. J. Bak, et al. (1976). "Long-term chronic recording from cortical neurons." Exp Neurol **52**(3): 496-506.

Schmidt, E. M., J. S. McIntosh, et al. (1988). "Long-term implants of Parylene-C coated microelectrodes." Med Biol Eng Comput **26**(1): 96-101.

Schwartz, A. B. (2004). "Cortical neural prosthetics." Annu Rev Neurosci **27**: 487-507.

Seymour, J. P., H. Chen, et al. (2008). Bioelectrical Performance of Microfabricated Parylene Substrates. Materials Research Society, San Francisco, CA.

Seymour, J. P., Y. Elkasabi, et al. (In Preparation). "Improved insulation performance in bioelectrical devices with a reactive parylene interface." Biomaterials.

Seymour, J. P. and D. R. Kipke (2006). "Fabrication of polymer neural probes with sub-cellular features for reduced tissue encapsulation." Conf Proc IEEE Eng Med Biol Soc **1**: 4606-9.

Seymour, J. P. and D. R. Kipke (2007). "Neural probe design for reduced tissue encapsulation in CNS." Biomaterials **28**(25): 3594-607.

Seymour, J. P., N. Langhals, et al. (2008). Sub-cellular edge electrode increases viewing angle and decreases arbor damage. Society for Neuroscience, Washington, D.C.

Seymour, J. P., N. Langhals, et al. (In Preparation). "Advancing microfabricated neural technology using chemical mechanical polishing to create a multi-sided electrode on a parylene structure " Biomedical Microdevices.

Stensaas, S. S. and L. J. Stensaas (1978). "Histopathological evaluation of materials implanted in the cerebral cortex." Acta Neuropathol (Berl) **41**(2): 145-55.

Stieglitz, T. and J. U. Meyer (1999). "Implantable microsystems. Polyimide-based neuroprostheses for interfacing nerves." Med Device Technol **10**(6): 28-30.

Strumwasser, F. (1958). "Long-term recording' from single neurons in brain of unrestrained mammals." Science **127**(3296): 469-70.

Suner, S., M. R. Fellows, et al. (2005). "Reliability of signals from a chronically implanted, silicon-based electrode array in non-human primate primary motor cortex." IEEE Trans Neural Syst Rehabil Eng **13**(4): 524-41.

Szarowski, D. H., M. D. Andersen, et al. (2003). "Brain responses to micro-machined silicon devices." Brain Res **983**(1-2): 23-35.

Takeuchi, S., D. Ziegler, et al. (2005). "Parylene flexible neural probes integrated with microfluidic channels." Lab Chip **5**(5): 519-23.

Taylor, D. M., S. I. Tillery, et al. (2002). "Direct cortical control of 3D neuroprosthetic devices." Science **296**(5574): 1829-32.

Truccolo, W., G. M. Friehs, et al. (2008). "Primary motor cortex tuning to intended movement kinematics in humans with tetraplegia." J Neurosci **28**(5): 1163-78.

Turner, J. N., W. Shain, et al. (1999). "Cerebral astrocyte response to micromachined silicon implants." Exp Neurol **156**(1): 33-49.

Tyler, W. J., Y. Tufail, et al. (2008). "Remote excitation of neuronal circuits using low-intensity, low-frequency ultrasound." PLoS ONE **3**(10): e3511.

Vetter, R. J., J. C. Williams, et al. (2004). "Chronic neural recording using silicon-substrate microelectrode arrays implanted in cerebral cortex." IEEE Trans Biomed Eng **51**(6): 896-904.

Wagner, T., A. Valero-Cabre, et al. (2007). "Noninvasive human brain stimulation." Annu Rev Biomed Eng **9**: 527-65.

Wans, J., M. Gulari, et al. (2005). A cochlear electrode array with built-in position sensing, Piscataway, NJ, USA, IEEE.

Weiland, J., W. Fink, et al. (2005). "Progress towards a high-resolution retinal prosthesis." Conf Proc IEEE Eng Med Biol Soc **7**: 7373-5.

Williams, J. C., R. L. Rennaker, et al. (1999). "Long-term neural recording characteristics of wire microelectrode arrays implanted in cerebral cortex." Brain Res Brain Res Protoc **4**(3): 303-13.

Wise, K. D., D. J. Anderson, et al. (2004). "Wireless implantable microsystems: high-density electronic interfaces to the nervous system." Proceedings of the IEEE **92**(1): 76-97.

Wise, K. D., J. B. Angell, et al. (1970). "An integrated-circuit approach to extracellular microelectrodes." IEEE Transactions on Biomedical Engineering **17**(3): 238-47.

Wise, K. D., A. M. Sodagar, et al. (2008). "Microelectrodes, microelectronics, and implantable neural microsystems." Proceedings of the IEEE **96**(7): 1184-202.

Ying, Y., M. N. Gulari, et al. (2007). "A microassembled low-profile three-dimensional microelectrode array for neural prosthesis applications." Journal of Microelectromechanical Systems **16**(4): 977-88.

Zhang, F., A. M. Aravanis, et al. (2007). "Circuit-breakers: optical technologies for probing neural signals and systems." Nat Rev Neurosci **8**(8): 577-81.

CHAPTER 2 Neural Probe Design for Reduced Tissue Encapsulation

2.1 Abstract

This study introduces a novel neural probe design with reduced chronic cellular encapsulation. We hypothesized that if a structural feature size is smaller than a reactive cell body (<7 μm), the resulting cellular encapsulation would be mitigated by the prevention of cellular spreading. We investigated this relationship between size and tissue reactivity using a microfabricated parylene structure. Devices were implanted in the rat neocortex for four weeks before immunostaining for neurons, astrocytes, microglia, fibronectin, laminin, and neurofilament. We found the nonneuronal density around the sub-cellular structure was less than one-half of the density around the device shank (129% versus 425% increase relative to control tissue, respectively). Moreover, neuronal density around the platform lateral edge was about one-third higher than at the shank (0.70 and 0.52 relative to control, respectively). Also, microglia reactivity and extracellular protein deposition was reduced at the lateral edge. There were no significant differences among platform designs. These results suggest that neural probe geometry is an important parameter for reducing chronic tissue encapsulation.

2.2 Introduction

Implantable chronic microelectrode arrays for neural recording are an important neurotechnology for systems neuroscience (Buzsaki 2004), with several emerging applications in neuroprosthetics (Schwartz 2004; Hochberg, Serruya et al. 2006). While there are a number of studies reporting long-term recording properties of varied types of

devices (Rousche and Normann 1998; Williams, Rennaker et al. 1999; Vetter, Williams et al. 2004; Santucci, Kralik et al. 2005; Suner, Fellows et al. 2005; Liu, McCreery et al. 2006), central issues of recording stability, signal quality, and longevity remain. Reactive tissue response to the implanted device is considered to be a primary factor in the long-term performance of the devices. Probe treatments or designs that elicit reduced chronic tissue responses are of high interest.

Histological examination of intracortical devices has consistently shown that a glial sheath forms around the probe tract (Maynard, Fernandez et al. 2000; Szarowski, Andersen et al. 2003; Biran, Martin et al. 2005). Cellular components of the glial sheath consist of activated microglia and hypertrophied astrocytes, and likely also include meningeal cells (Shearer and Fawcett 2001; Kim, Hitchcock et al. 2004), and oligodendrocyte precursors (Hampton, Rhodes et al. 2004). These cell types produce extracellular proteins that hinder local nerve regeneration (Fawcett and Asher 1999; Shearer and Fawcett 2001). In addition, a neuronal "kill zone" has been reported around neural probes (Edell, Toi et al. 1992; Biran, Martin et al. 2005). After an injury, tissue encapsulation modifies the extracellular space as evidenced by mass transport (Roitbak and Sykova 1999) and impedance spectroscopy studies (Williams, Rennaker et al. 1999; Johnson, Otto et al. 2005; Ludwig, Uram et al. 2006). Injured CNS tissue loses volume fraction and gains tortuosity (Nicholson and Sykova 1998). Tissue encapsulation is also concomitant with a decrease in the signal quality of neural recordings in the brain and the periphery (McCreery, Agnew et al. 1987; Schmidt, McIntosh et al. 1988; Lefurge,

Goodall et al. 1991; Rousche and Normann 1998; Liu, McCreery et al. 1999; Williams, Rennaker et al. 1999; Ludwig, Uram et al. 2006). These studies have motivated the pursuit of several approaches to reduce tissue encapsulation around implantable devices, including surface modification (Cui, Lee et al. 2001; He and Bellamkonda 2005) and local drug delivery (Shain, Spataro et al. 2003; Zhong and Bellamkonda 2005; Kim and Martin 2006).

Modified microscale geometry may provide an alternative means of minimizing reactive cell responses. In vitro work has shown that macrophages do not adhere to or spread on polymer fibers ranging in diameter from 2 to 12μm (Bernatchez, Parks et al. 1996). In vivo, single polymer fiber strands (diameters between 2.1 and 5.9 μm) in the rat subcutis have been shown to elicit decreased capsular thickness compared to larger diameter strands (Sanders, Stiles et al. 2000). Additionally, substrate geometry and feature size has been associated with cellular mechanotransduction in studies of adhesive substrate patterns looking at apoptosis and cellular spreading (Chen, Mrksich et al. 1997; Turner, Dowell et al. 2000; Chen, Tan et al. 2004).

These studies helped to motivate our hypothesis that a subcellular-sized lateral edge will have less tissue encapsulation relative to the larger probe shank. To test this hypothesis, we implemented a probe design with a conventional, thick shank that supported a 5-μm thick lateral platform. The thicker shank provided the structural strength to penetrate the rat pia matter and advance straight into the cortex. Furthermore, three of the four platforms were lattices of varying lattice width. The smallest lattice width was also

hypothesized to induce less tissue encapsulation than the larger lattice width. The objective of this study was to investigate the relationship between probe size and shape and the reactive tissue responses in a chronic animal preparation. Whereas other studies have investigated differences of larger structures (Szarowski, Andersen et al. 2003), we specifically considered probe elements on the subcellular level (5 μm). Encapsulation and neuronal loss were correlated with the different probe geometries by employing high resolution confocal images to determine neuronal and nonneuronal cell densities. Double labeling with a variety of immunostains around the intact neural probe provided additional qualitative analysis of the device-tissue microenvironment, including astrocytes, microglia and several extracellular matrix proteins.

2.3 Materials and Methods

2.3.1 Neural Probe Design and Fabrication

An SEM image and CAD layout of a lattice-like neural probe with subcellular features is shown in Fig. 2-1(a-b). This experiment tests four different platforms, one without a lattice and three with a lattice design of varying size (Fig. 2-1(b-e)). The specific dimensions chosen were greatly influenced by the size-dependent experiments discussed above. The shank dimensions were chosen to provide sufficient stiffness to penetrate the rat pia matter. To limit the number of variables, each design has identical outer dimensions and thus each design has an identical cross-sectional footprint. Each thin, lateral structure extends 100 μm and is 5 μm thick. Lattice size (4, 10, 30 μm, and 100 μm, the last being solid) and the percentage of open area is unique to each. All of the

probes had similar tip shapes (13 degrees, chisel-shaped). Probe shank dimensions were measured to be 68.0±1.1 µm wide by 48.2±2.5 µm thick. The lattice width was 4.0±0.2, 9.8±0.4, and 29.5±0.5 µm respectively.

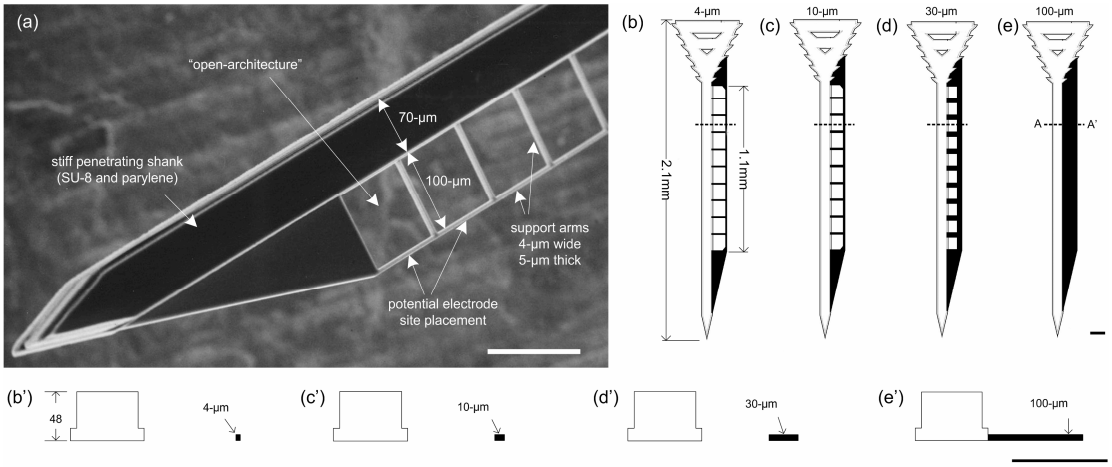

Figure 2.1. Neural probe design with subcellular dimensions. (a) An SEM perspective view of a parylene-based open-architecture probe used for in vivo testing. The tip of the probe is at the lower left. (b-d) CAD drawings of each probe design indicating overall length and width of three lattice platforms (4µm, 10µm, 30µm), and (e) one non-lattice platform (100µm wide). (b'-e') Cross-sectional view of line A-A' shown in (b-e). All probes have identical shank and outer dimensions. Scale bars = 100µm.

The probes were microfabricated in the Michigan Nanofabrication Facility. The fabrication did not include metallization. A sacrificial release layer of SiO2 was grown on a 4-inch Si wafer (Fig. 2-2(a)). Parylene-C was deposited (5-µm thick) via chemical vapor deposition using a PDS-2010 obtained from Specialty Coating (Indianapolis, IN). A Ti layer 1000Å was deposited and patterned for later use as a mask for the subcellular lattice structure (Fig. 2-2(b)). SU-8 2025 (Microchem, Newton, MA) was spin-coated to 38-µm (±2-µm) and patterned to create the core of the probe shank (Fig. 2-2(c)). Oxygen plasma RIE surface treatment was applied before and after the SU-8 layer to improve

interfacial adhesion. The second parylene layer was deposited 5-µm thick. This film conformed to the SU-8 backbone (Fig. 2-2(d)). We spun an 80-µm thick AZ-9260 resist layer to cover the SU-8 structures and mask the shank of the probe (Fig. 2-2(e)). Parylene was etched using oxygen plasma RIE. Probes were released using hydrofluoric acid and then thoroughly rinsed in DI water, ethanol, and acetone (Fig. 2-2(f)).

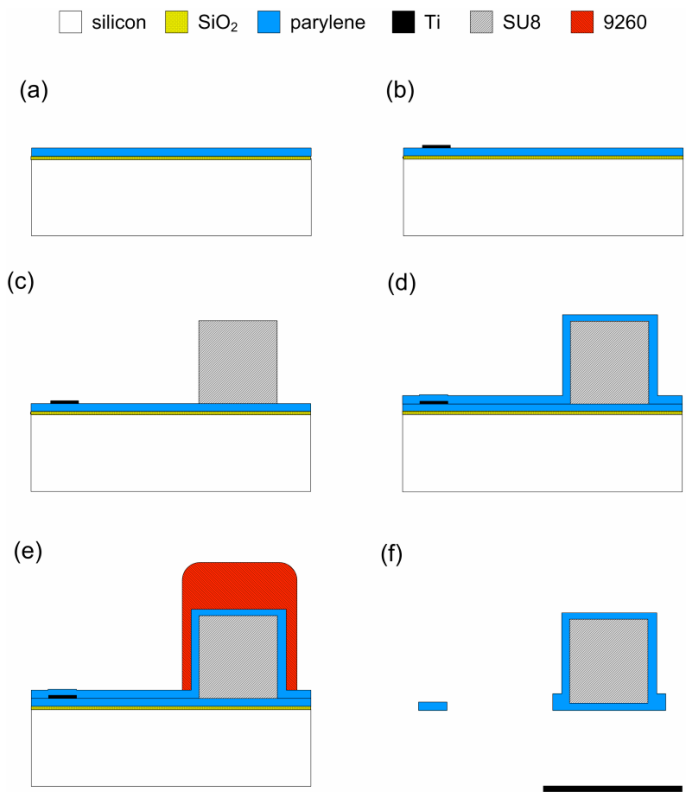

Figure 2.2. Cross-sectional view of wafer level fabrication. (a) Parylene deposited on SiO2 sacrificial layer. (b) Patterned titanium to mask parylene. (c) SU-8 patterned shank. (d) Parylene encapsulated SU-8 structure. (e) 9260 resist patterned to form thick mask over shank. (f) Etched and released cross-section. Three masks used for photolithography in (b, c, e). X-scale = 100µm (Y-scale approx.).

2.3.2 Neural Probe Assembly

A stereotaxic frame was used to insert each probe with a controlled trajectory to minimize insertion damage and variability (Edell, Toi et al. 1992; Rousche and Normann 1992). First a metal insertion plate (custom machined) placed on a glass slide is heated to ~50°C, and then the glass slide was placed on a dissecting microscope. The probe head was mounted in the notched region of the heated insertion plate using poly(ethylene glycol) or PEG (8000 M.W, Acros, Geel, Belgium). Rapid cooling prevented the PEG from wicking onto the shank of the probe.

The PEG and insertion plate were autoclaved separately prior to assembly. Probes were cleaned before and after assembly with 90% ethanol. Additionally, the probe and insertion plate assembly were sterilized with ethylene oxide (EtO) at ambient temperature and allowed to vent for 24 hours under vacuum. When EtO sterilization was unavailable, ultraviolet exposure in a sterile hood for 30 minutes was used instead (2 of 7 animals). All probes in a given animal used an identical sterilization technique.

2.3.3 Surgical Procedure

Multiple untethered probes were surgically implanted in male Sprague Dawley rats (300-350 grams). Anesthesia was administered using intra-peritoneal injections of a mixture of ketamine, xylazine, and acepromazine. The craniotomy spanned approximately 4mm in the anterior-posterior direction, and 3mm in the medial-lateral direction and was centered

over the M1 and M2 motor cortex. A ~3X stereoscope was used to ensure a nearly orthogonal trajectory and avoid any visible blood vessels. After a probe was inserted via a manual stereotaxic drive (coordinate range of 2.0-3.5 mm AP, 1.5-3.0 mm Lat), sterile artificial cerebral spinal fluid (Harvard Apparatus, Holliston, MA) was added to the craniotomy to release the probe from the insertion plate. By rotating the insertion plate and applying pressure to the probe head (height is 320-μm), the probe was then driven nearly flush with the brain surface to reduce transcranial tethering (Appendix A, Fig. A-1). Transcranial tethering would be expected to increase tissue reactivity (Kim, Hitchcock et al. 2004). Less than 200-μm of the probe was above the brain surface. Four probe types (Fig. 2-1(d-g)) were inserted in random order and orientation. One craniotomy contained all four neural probes, separated by a minimum of 0.5-mm. Surgical closure included a thin layer of purified calcium alginate followed by silicone and dental acrylic (Co-Oral-Ite Dental Mfg. Co., Diamond Springs, CA) (Vetter, Williams et al. 2004). All procedures strictly complied with the United States Department of Agriculture guidelines for the care and use of laboratory animals and were approved by the University of Michigan Animal Care and Use Committee.

2.3.4 Immunohistochemistry

Four weeks after implantation animals were terminally anesthetized. Transcardial perfusion with 100 mL of chilled PBS was followed by 450 mL of 4% (w/v) paraformaldehyde in PBS. The brain tissue was removed and immediately explanted and

postfixed overnight in 4% paraformaldehyde. Following postfixation, brain tissue was equilibrated in 30% sucrose in PBS and sectioned at 12-μm on a cryostat.

Tissue sections between cortical layers II and V were immunostained for each marker combination (see Table 1, 2) spanning approximately 1.1 mm of the cerebral cortex. The depth of interest was easily identified by the probe geometry seen in the transverse sections (see Fig. 2-1(b'-d')). Sections were not excluded or included based on the presence of a support arm. Sections were treated for 1 hour with blocking solution at room temperature. All antibodies were diluted in blocking solution consisting of 4% (v/v) normal goat serum and 0.3% (v/v) Triton-X-100 for 6-10 hours at room temperature. Alexa-488 and Alexa-568 labeled secondary antibodies (Invitrogen, Carlsbad, CA) were diluted in blocking solution to a concentration of 10 μg/mL. Secondary antibodies were incubated for 2 hours at room temperature. All sections were counterstained with 2 μg/mL Hoechst 33342 (Invitrogen) for 10 minutes. After washing with PBS, sections were mounted with a coverglass using the antifade reagent Prolong Gold (Invitrogen).

Table 1. Summary of Antibodies

Antibody	*Antigen*	*Cell type(s)*	*Isotype*	*Dilution*	*Vendor*
GFAP	Glial fibrillary acidic protein	Astrocytes	IgG (rabbit)	1:400	Sigma
Fibronectin	Fibronectin	Fibroblasts	AI (rabbit)	1:800	Sigma
Laminin	Laminin	—	AI (rabbit)	1:400	Sigma
NeuN	Neuronal nuclei	Neurons	IgG1 (mouse)	1:1000	Chemicon
Neurofilament	NF-M intermediate filaments	Neurons	NA (rabbit)	1:1000	Novus
OX-42	CR3 on cd11b integrin	Microglia, macrophages	IgG2a (mouse)	1:200	Serotec

AI=affinity isolated, NA=not applicable

Table 2. Double Label Combinations

Double Label	*Number of Animals*	*Minimum number of sections per animal*
OX-42, GFAP	3	12
NeuN, GFAP	7	8
NeuN, Laminin	7	8
OX-42, Fibronectin	7	3
NeuN, Neurofilament	3	4

Hoechst counterstain used with all

2.3.5 Cell Counting and Statistical Analysis

Eight transverse tissue sections spanning the length of the probe lattice structure (1.1mm) were randomly chosen for cell counting. Confocal images were collected for these NeuN and Hoechst labeled sections using an Olympus FV500 (40X, oil immersion, NA=1.3). A MatLAB graphical user interface was developed for off-line cell selection. First an outline of the intact probe or device-tissue interface was defined by a combination of a differential interference contrast (DIC) and UV fluorescence image (Fig. 2-3a). Small void spaces occasionally present between the probe and tissue as a result of tissue processing were included within the device-tissue interface boundary. A technician (blinded from study) selected all nuclei as either neuronal (NeuN+, Hoechst+) or nonneuronal (Hoechst+ only) from defined regions (lateral edge or probe shank). The technician was presented one optical slice at a time for each physical section, and four optical images per physical section (3 μm step size spanning 9 μm of tissue). Cells selected on the first optical image were clearly marked on the second image and so on until the fourth image was analyzed to prevent double counting (Fig. 2-3b shows the fourth optical section with the cumulative cell selection). Ultrathin optical sections (0.4

μm) greatly improved the user's ability to uniquely identify cells. Two regions were bounded with a radius of 75-μm from the device-tissue boundary (Fig. 2-3b). The probe shank region only included the three outside faces in order to avoid overlap with the lateral edge region. The lateral edge region also included the three outside faces, but only the first 5 μm from the lateral-most point—regardless of the lattice feature size (4, 10, 30, 100 μm). This rule ensured that all regions of interest were equidistant from one another.

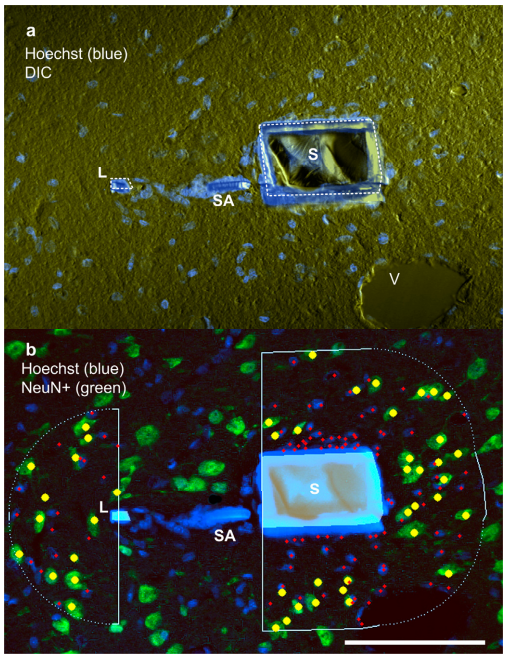

Figure 2.3. Example images illustrating counting method. (a) Hoechst and differential interference contrast (DIC) image (4-μm probe) used to define the device-tissue interface, showing both lateral edge (L) and probe shank (S). This transverse section has a similar cross-section as shown in Fig. 1(b'). Portion of support arm (SA) was captured in section, as well as a large vessel (V). (b) Screen shot of technician-interface illustrating counting method. Red and yellow dots indicate selection of nonneuronal (Hoechst+, NeuN-) and neuronal cells (NeuN+) respectively. White borders are generated automatically and mark the 75-μm radius from the device-tissue boundary defined in (a). Left and right semi-circular regions represent the lateral edge (L) and probe shank (S) response regions. Scale=100μm. 40X Obj.

After cell selection, the cell coordinates and device-tissue boundary coordinates were stored. A software algorithm used the center of each nucleus (user-selected) to calculate the shortest distance to the probe boundary, bin the counts by distance and region, and calculate the sampling area of each bin to form the processed data set.

Each count by bin and region (lateral edge or probe shank) was converted to density using area. Each density value was normalized by the mean contralateral density to produce unitless values. Contralateral tissue images were identically processed using the cell selection user-interface and a generic device-tissue boundary overlay. Cells beneath the overlay were not counted.

A linear mixed effects model was used to evaluate the normalized responses of neuronal density, nonneuronal density, and the ratio of the two. The fixed effects were the location (lateral edge or probe shank), the probe type (4, 10, 30-μm lattice designs, and a 100-μm solid design), and the interaction of location and probe type. The random effect in the model was the subject (N=7). The model was fit by maximizing the restricted log-likelihood. Analysis was performed using the statistical package R 2.4.1 (www.r-project.org). Statistical significance was defined at the 5% level. We used a one-sided t-test to determine if cell densities around the probe types were different than the contralateral tissue, and whether an inherent bias existed in the contralateral control tissue (lateral edge or probe shank) (significance threshold of $p<0.05$, N=7 subjects).

2.4 Results

Seven male Sprague Dawley rats (300-350 grams) were implanted with the four designs described above (Fig. 2-1(b-e)). There were no mechanical failures during insertion of these 28 probes. Dimpling rarely occurred during insertion. When dimpling did occur (possibly due to the presence of blood vessels near the pial surface (Bjornsson, Oh et al. 2006)), the mild depression did not produce excessive bleeding. High resolution images of the intact probes (transverse cryosections) revealed structural integrity out to 4-weeks post implant (Fig. 2-3(a)).

The success of these surgeries and post-implant imagery showing structural preservation indicated that the tip angle, shank stiffness, and leading edge were sufficiently designed to pierce the rat neocortex in a straight trajectory and prevent damage to the fine 4-µm x 5-µm x 100-µm parylene lattice. Larger lattice platforms also maintained their integrity.

2.4.1 Quantitative Cell Density as a Function of Probe Geometry

Cellular encapsulation was hypothesized to be dependent on the size and shape of a given probe structure. In this context, we compare the cellular density by both lattice size (4, 10, 30-µm lattice structures, and 100-µm solid structure, all 5-µm thick) and the lateral edge (L) versus the probe shank (S).

Cell Density in the Contralateral Hemisphere

Counting in the contralateral hemisphere of neuronal and nonneuronal cells defined the baseline for changes around the device-tissue interface. As expected, no significant differences between the lateral edge and probe shank control regions existed for neuronal or nonneuronal cell density (N=7 subjects).

Cellular Encapsulation

A significant improvement in cellular response was found between the shank and lateral structure within the first 25 μm for all probe geometries. Fig. 2-4 provides four representative confocal images for each probe type. NeuN immunolabeling identified neurons and Hoechst counterstain identified nonneuronal cells (not NeuN+). A linear mixed effects model was used to evaluate the factors of probe type (4, 10, 30-μm lattice designs, and a 100-μm solid design) and location (lateral edge, probe shank) (Table 3). Only the location factor was significant. Beyond the 0-25 μm bin there was no significance for any factor. Interaction terms between the two factors was also tested but were not significant (data not shown).

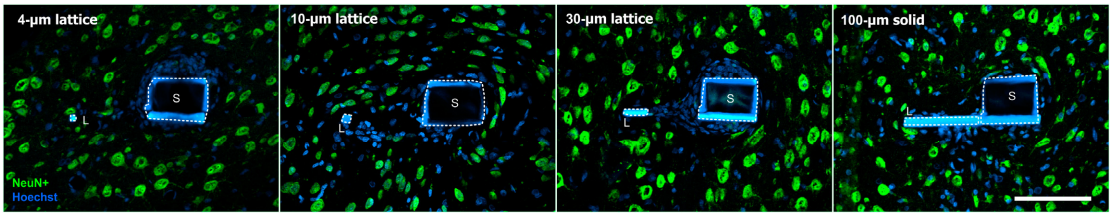

Figure 2.4. IHC images showing NeuN+ reactivity (green) and Hoechst counterstain (blue) for each probe type. Probe type from left to right: 4 µm, 10 µm, 30 µm, 100 µm. Parylene auto-fluorescence has greatest intensity in violet spectrum where the lateral edge (L) and shank (S) are easily identifiable. Scale = 100 µm. 40X Obj.

Nonneuronal density for each probe geometry and distance bin was compared (Fig. 2-5). Encapsulation decreased dramatically around the shank beyond the 0-25 µm bin. When averaged across probe types (Fig. 2-5(b)) in the 0-25 µm bin, the nonneuronal density was 2.29±1.76 around the lateral edge compared to 5.25±2.66 around the shank. This corresponds to an increase of 129% and 425% relative to contralateral tissue for the lateral edge and probe shank respectively.

Table 3. Statistical Factors Influencing Cellular Density (0-25 µm bin[1])

Response		*Intercept*[2]	*10-µm Lattice*	*30-µm Lattice*	*100-µm Solid*	*Probe Shank*
Neuronal Density	Coefficient[3]	0.78	-0.21	-0.06	-0.05	-0.25
	P value	NA	0.082	0.582	0.671	**0.038**
Nonneuronal Density	Coefficient	1.91	1.83	-0.25	-0.06	3.68
	P value	NA	0.054	0.791	0.950	**0.0003**

1. No significance in factors beyond 0-25 µm bin.
2. Model intercept defined to be the lateral edge of the 4-µm lattice.
3. Coefficient values are relative to the intercept.

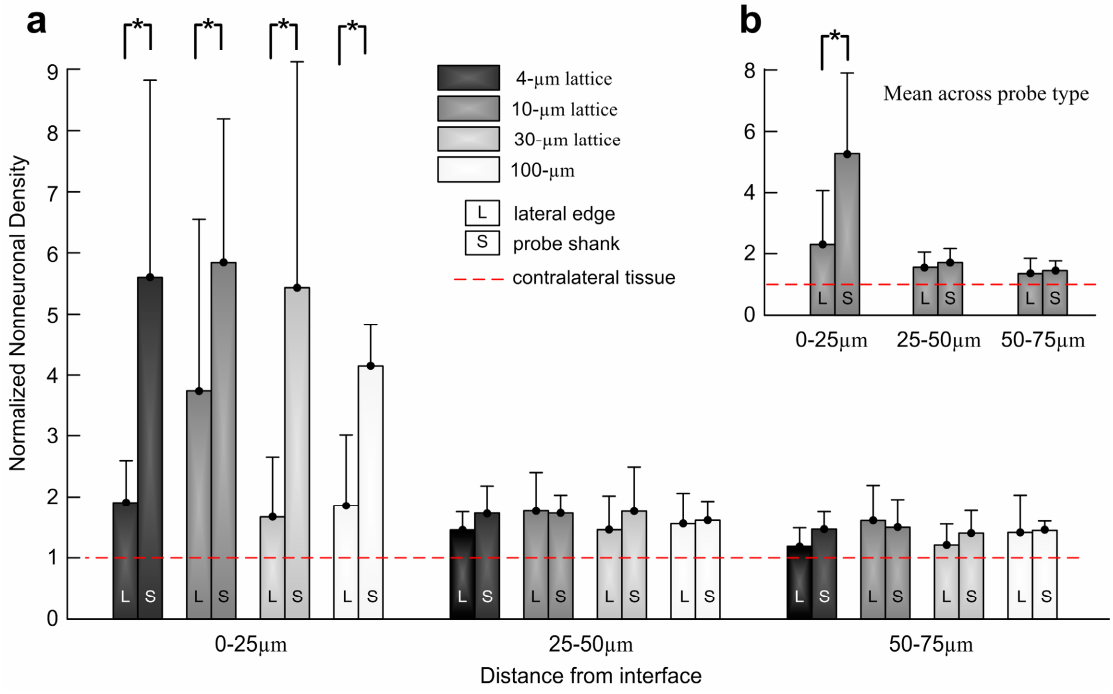

Figure 2.5. Normalized nonneuronal density (NND) as a function of distance. (a) NND around each probe type and location. Density at the lateral edge (L) and probe shank (S) regions are paired together. In 0-25µm bin, there was significance between lateral edge versus probe shank regions (p=0.0003). (b) Mean NND for all probe types. Error bars denote standard deviation (S.D.). (Linear mixed-effects model, level<0.05)

Neuronal Density

Normalized neuronal density for each probe type and location was compared (Fig. 2-6) The location was the significant factor in predicting neuronal density ($p<0.04$). Testing for significance between each platform type did not reveal a difference. Neuronal loss was greatest in the first distance bin where the immediate injury and secondary injury were expected to be foremost. When the normalized density was averaged for all probe types (Fig. 2-6(b)), the lateral edge value was 0.70±.33 and the probe shank was 0.58±.24

over the first 25 µm. This corresponds to a neuronal loss of 30% and 48%, respectively, relative to contralateral tissue.

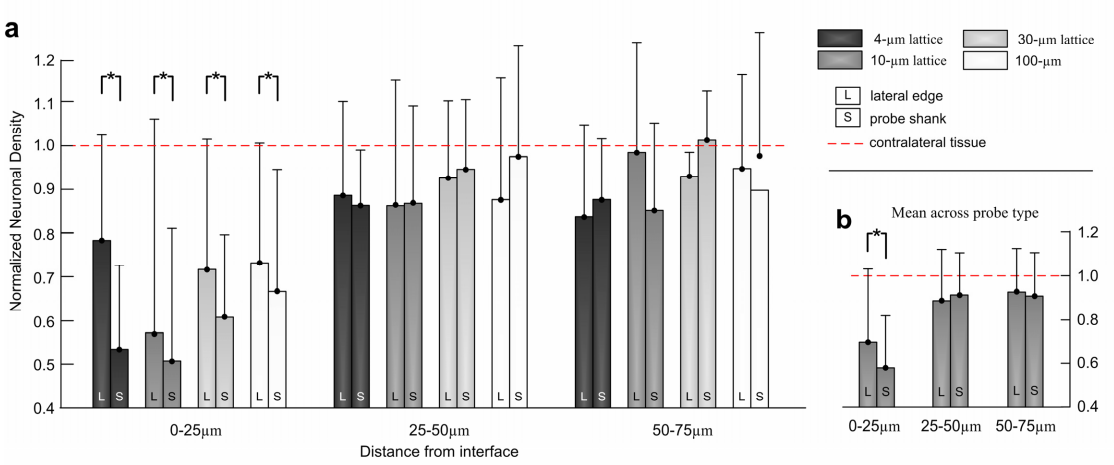

Figure 2.6. Normalized neuronal density as a function of distance. (a) Neuronal density around each probe type and location. Density at the lateral edge (L) and probe shank (S) regions are paired together. In 0-25µm bin, there was significance between lateral edge versus probe shank regions. (b) Mean neuronal density for all probe types. Error bars denote S.D. (Linear mixed-effects model, level<0.05)

2.4.2 Qualitative Results: Double Label Immunostaining

Several double labels were used to investigate the complex foreign body response around the probe. Table 2 lists the number of animals and minimum number of sections for each combination. GFAP (astrocytes), OX-42 (microglia), NeuN (neurons), fibronectin, laminin, and neurofilament immunostain combinations improve our understanding of the cellular and extracellular protein interactions in the central nervous system (CNS). A description and figure for the combination of laminin-/NeuN, and neurofilament-/NeuN is provided as supplemental information (Appendix A, Fig. A-2, A-3).

To illustrate variations between the responses at the lateral edge location and the shank, we provide two columns of images that were selected by the degree of reactivity (Fig. 2-7, 2-8, 2-9). At the top of each column, the mean value of the nonneuronal density (NND) is provided. The histological responses and descriptions are representative of two extreme cases in the dataset. Note that the contrast in reactivity between the columns of images is not intended to compare lattice width. The greatest variation in NND occurred around the probe shank and not the lateral edge, where there were few examples of a high NND.

GFAP and OX-42

Two key cellular types in any CNS injury are astrocytes and microglia. GFAP+ tissue indicates astrocyte structure, and as seen in Fig.2-7, a stellate, intertwined morphology forms around the device-tissue interface. In the low NND example on the left, GFAP

reactivity was evident within several microns of both the lateral structure and shank, although less intense in the former. Around the high NND example (Fig. 2-7(d- f)), GFAP+ tissue circumscribed the probe shank and was approximately 10 μm distant from the shank. This demarcation between GFAP+ and densely packed nuclei (see Fig. 2-7(f)) was common wherever dense nuclei existed.

The OX-42 antigen is a CD11b integrin found on the surface of microglia and macrophages. Activated microglia exhibit an upregulation of CD11b and an ameboid shape with few processes. Microglia exhibit finely branched structures with little cytoplasm when unactivated (Schwartz, Butovsky et al. 2006). This study shows OX-42 reactivity was greatest at the interface, and the intensity and thickness of OX-42+ tissue corresponded well with dense capsular nuclei, consistent with previous studies (Szarowski, Andersen et al. 2003; Hampton, Rhodes et al. 2004; Biran, Martin et al. 2005). OX-42+ tissue around a low NND interface was characterized by a mildly intense, thin layer, and concomitant with GFAP+ tissue (arrow in Fig. 2.7). When the cellular encapsulation layer was dense, the intense OX-42+ region that dominates the interface was devoid of GFAP+ reactivity (* in Fig. 7).

The morphology of OX-42+ structures at the lateral edge (Fig. 2-7, 2-9) is important to note. Compact, ameboid structures were rarely observed at the outside lateral edge; instead, finely branched processes were evident. While microglia were present around the lateral structure, qualitatively these cells did not exhibit the same morphology and compactness as those around the probe shank.

In summary, the regions around the far lateral edge had less encapsulation and OX-42 reactivity relative to the shank. The morphology of OX-42+ structures also indicated a difference in phenotype between regions. GFAP+ tissue was always present at the lateral edge, but not always present immediately around the shank interface.

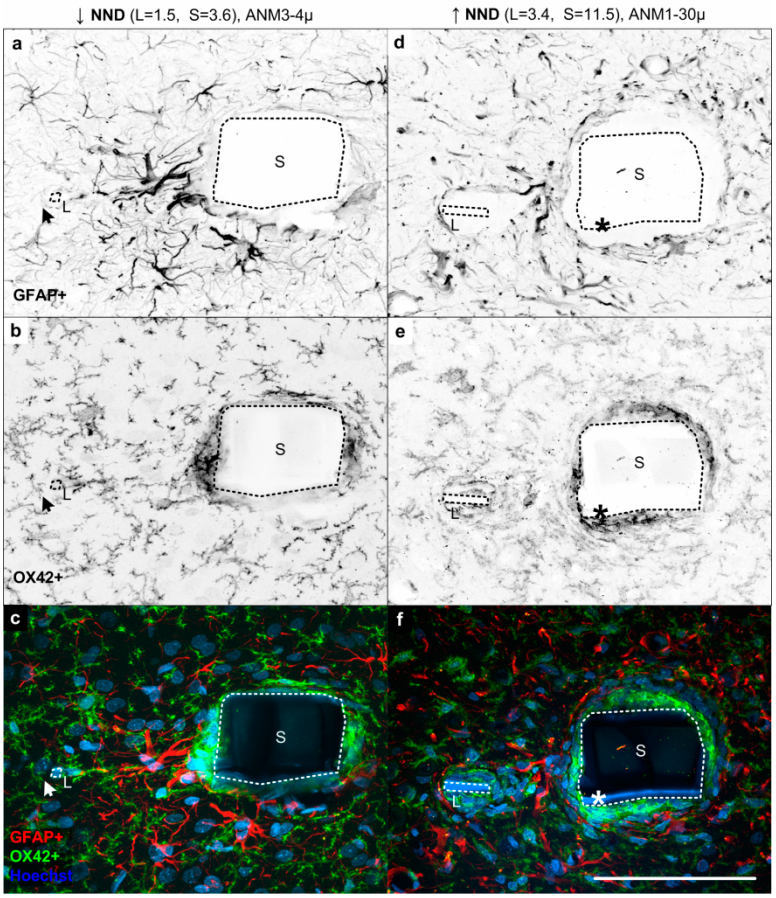

Figure 2.7 Inverted grayscale IHC images (a-b,d-e) showing GFAP (a,d) and OX-42 reactivity (b,e), and the corresponding RGB color image including Hoechst. (c,f). Mean value of nonneuronal density (NND) reported (N=8 sections). (a-c) An example of a low NND. Tissue response around this type of interface was characterized by mild OX-42 reactivity, nearby ramified microglia, and OX-42 concomitant with GFAP+ tissue (e.g. arrow). (d-f) A high NND interface was characterized by intense OX-42 with an ameboid morphology, and a demarcation of GFAP reactivity (* in d-f). Scale = 100 μm. 60X Obj.

GFAP and NeuN

GFAP was present at the interface when cellular encapsulation was sparse (Fig. 2-8(a,e)) and displaced when the capsular cells were dense (Fig. 2-8(b,f)). Only occasionally was GFAP+ tissue observed deeply penetrating pockets of dense nuclei. NeuN+ structures were commonly found in and around intense GFAP+ tissue. Hypertrophied astrocyte-like processes were noted to extend around NeuN+ tissue when neurons were near the probe surface. This colocation of astrocytes and neurons was expected (Fawcett and Asher 1999). In the two examples shown, neurons can be seen adjacent to the central lattice region and enveloped by GFAP+ filaments (* in Fig. 2-8). Incidences of neuronal survival within several microns of the lattice region occurred in only three of seven subjects.

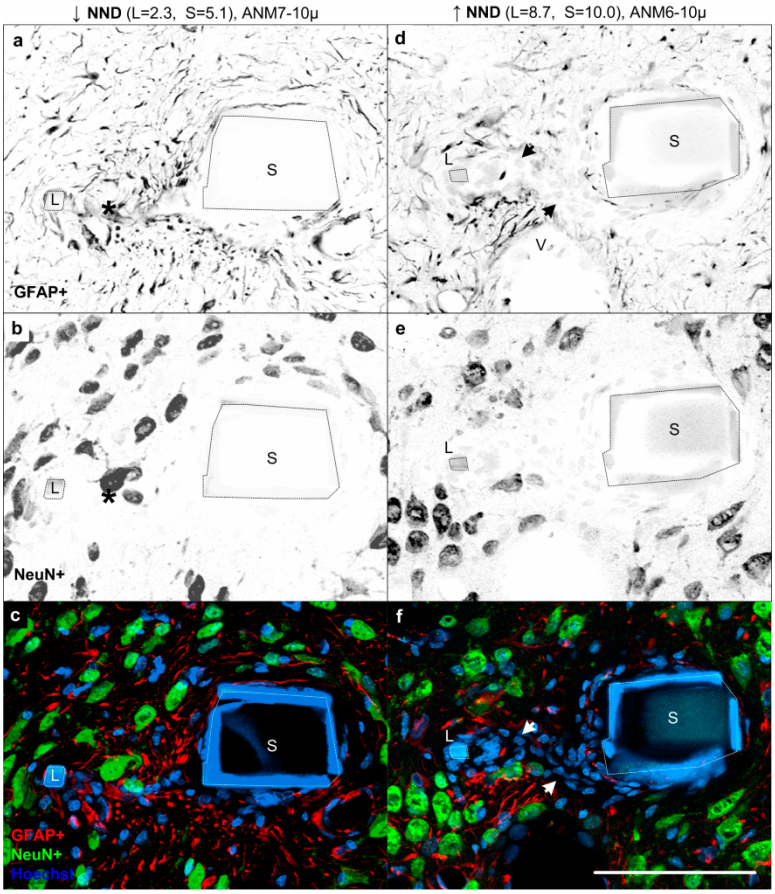

Figure 2.8 Inverted grayscale IHC images (a-b,d-e) showing GFAP (a,d) and NeuN reactivity (b,e), and the colocalization of these including Hoechst counterstain in RGB color (c,f). (a-c) A low NND was characterized by a concurrence of NeuN+ and GFAP+ tissue (* in a,b). (d-f) Few neurons were near the high NND interface. In these cases, GFAP- and dense encapsulating cells characterized the probe interface and open-architecture region (arrows, d, f). Scale = 100 µm. 60X Obj.

Fibronectin and OX-42

Fibronectin labels meningeal fibroblasts in the CNS (Shearer and Fawcett 2001; Bundesen, Scheel et al. 2003) and, like laminin, is a constituent of basal lamina. Fibronectin immunolabeling revealed a similar pattern of reactivity as observed with

laminin (Fig. A-2). In low NND examples (Fig. 2-9(a,c,e)), fibronectin+ tissue was limited to the immediate probe interface and the inside corner of the probe (* in Fig. 2-9(a-c)). The high NND example (Fig. 2-9(b,d,f)) has a wider tract of tissue reactivity around the probe shank. OX-42 reactivity was also most intense at the interface but was not limited to the immediate probe interface. Interestingly, in many cases where encapsulation was pronounced, OX-42+ and fibronectin+ reactivity was similar in pattern but not always overlapping (arrows in Fig. 2-9). In many other images (data not shown), fibronectin and laminin was not present. Again, a difference in microglia phenotype was apparent in tissue around the shank versus the lateral edge.

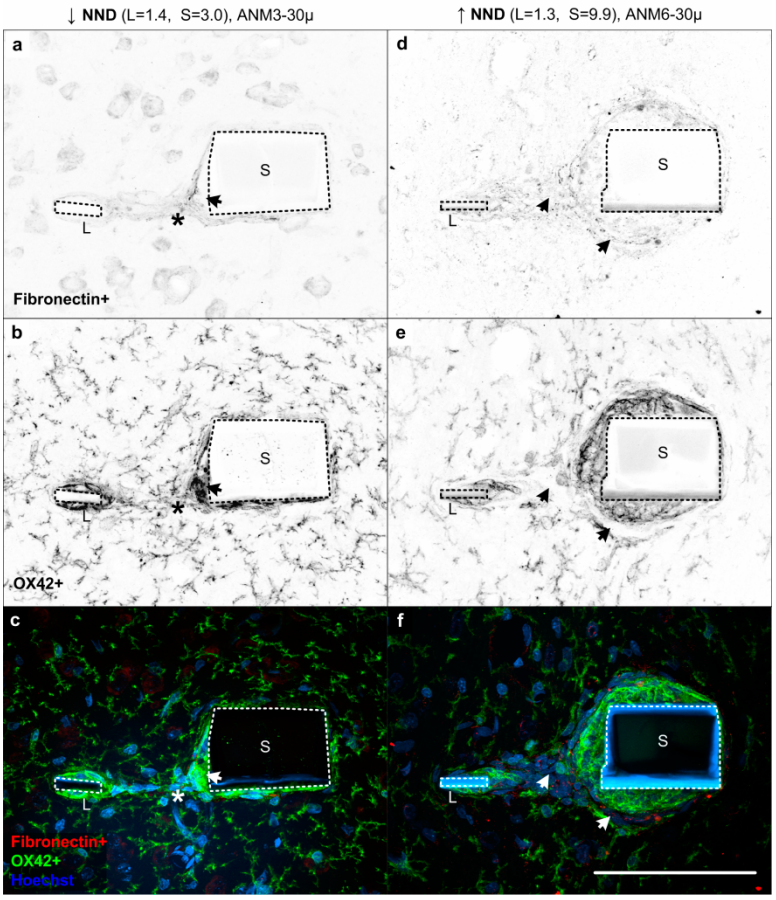

Figure 2.9 Inverted grayscale IHC images (a-b,d-e) showing fibronectin (a,d) and OX-42 reactivity (b,e), and the corresponding RGB color image including Hoechst (c,f). Fibronectin staining had a pattern similar to laminin (Suppl. Fig. 1). (a-c) The low NND response had only a thin band of intensely labeled cells surrounded by ramified microglia just several microns distant. The inside corner of shanks (all probe types) usually exhibited intense OX-42 staining (b,e). (d-f) Fibronectin deposition extended 5 to 15 µm from the shank interface and was located with densely packed nuclei. While OX-42+ and fibronectin+ tissue were often concordant (* in a-c), highly encapsulated interfaces have non-overlapping regions suggesting that not all cells were microglia (arrows, a-f). Scale = 100 µm. 60X Obj.

2.4.3 Reactivity in the Lattice Region

The reactivity in the inside corner (nearest the shank) is often intense (Fig. 2-7, 2-8, 2-9), and sometimes even greater than around the shank. In the middle of the lattice region we see a variety of responses—from highly OX-42 and fibronectin reactive to the other

extreme of GFAP and NeuN reactive. The presence of neurons was only occasionally seen and not necessarily "inside" the probe lattice. In general, the encapsulation and OX-42 reactivity of the lattice region was similar to that found around the shank of the probe, and with no apparent dependence on lattice size (data not quantified).

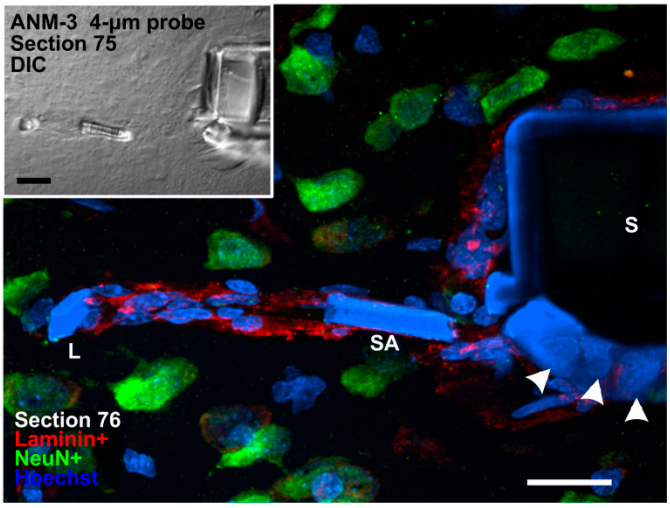

Figure 2.10 Reactivity around the support arm of a 4-µm lattice platform. Two consecutive sections are shown, a DIC and IHC color image. Given a slight offset in the transverse sectioning angle, only a portion of the support arm (SA) was embedded in each. The tight but intense laminin staining in section 76 formed an outline of the support arm. Contrastingly, a single nucleus at the outside lateral edge was more spherical in shape. Cells on the surface of the probe shank conformed to the flat surface in a disc-like pattern (arrows). Shapes were evaluated using three-dimensional confocal images (not shown). Scale = 20 µm.

An example confocal image showing a support arm segment succinctly captures a pattern found around the three regions of interest— probe shank, lattice region, and platform lateral edge (Fig. 2-10). The first layer of parylene around the shank has been rotated 90° due to cryosectioning or processing and effectively provides a coronal view of nuclei adhering to its surface (see arrows). The nuclei were disc-shaped and relatively large. Around the support arm, three-dimension confocal images (not shown) revealed the

nuclei to be elongated in one dimension—along the length of the support arm. The morphology of nuclei at the outside lateral edge were relatively small, spherical, and sparsely packed. These nuclei were rarely elongated or conformal to the edge despite this structure having identical dimensions as the support arm. Additionally, intense but narrow laminin+ tissue (Fig.A- 2) was outlining the shank and support arm structures, but not the outside edge.

2.5 Discussion

The contrast in encapsulation and neuronal loss between the shank and lateral edge described above demonstrates a differential chronic tissue response between the probe shank and the platform's lateral edge. The degree of neuronal loss reported here is smaller than two other quantitative reports on the biocompatibility of neural probes (Edell, Toi et al. 1992; Biran, Martin et al. 2005). Edell et al. reported significant loss (90% confidence level) in two rabbits out to 10 and 60 μm from the interface of silicon shanks (cross-section 40 by 60-μm). Using a slightly different metric, Biran et al. (2005) reported a loss of 40% around a silicon probe in a 100-μm radius from the interface at both 2 and 4 weeks (cross-section 15-μm by ~150-μm). When we averaged across all probes (N=28) for a 75-μm radius, the shank region had a loss of 17%, and in the lateral region the loss was only 12% (calculated from Fig. 2-6 and weighted by area). There was no significant loss beyond the first 25 μm for any probe type relative to the contralateral tissue. A number of differences between studies may account for our improved interface—we used a stereotaxic frame for insertion, intraparenchymal probes, and a

different substrate material. Nonetheless, we are encouraged by the comparatively healthy interface around the shank of parylene probes, and that despite this we found significant advantage at the lateral edge. A direct comparison of encapsulation density is not possible since prior studies have not quantified this effect, but the variability and extent of encapsulation seems comparable (Rousche and Normann 1998; Turner, Shain et al. 1999; Szarowski, Andersen et al. 2003; Biran, Martin et al. 2005).

These results support our first hypothesis—that the far lateral region on a 5-µm thick structure would have less encapsulation and neuronal loss because the reactive cells are presented with a narrow edge preventing the prototypical attachment and spreading seen in the foreign body response. More specifically, below a certain dimension a cell may not be able to attach and create tension in the cytoskeleton, which in turn disrupts the mechanotransduction pathway that may induce the unfavorable response (Chen, Mrksich et al. 1997; Sanders, Stiles et al. 2000; Chen, Tan et al. 2004). In addition to the quantitative evidence, we believe the altered morphology seen around the various probe regions (Fig. 2-7,2-9,2-10) supports this theory. Along the shank the nuclei were disc-like and spread out on the face of the probe (Fig. 2-10). At the lateral edge, there were rarely nuclei immediately present and nearby nuclei had smaller, spherical forms. However, our interpretation of these results is qualified by several possible confounding factors, namely flexibility, surface properties, and the influence of the lattice structure. The lateral edge not only presents a narrow feature, but also an increased flexibility relative to the probe shank. Surface properties on all outside or inside faces of the probe have a rough finish

due to the reactive plasma etch used to define them. Since the shank and the inside lattice faces also had similar properties, this factor is of small concern. The influence of the lattice structure was controlled for by the 100-μm solid design, which was not significantly different. Future studies are needed to verify the mechanism causing the improvement at the lateral edge.

Our hypothesis regarding the tissue reactivity around a lattice structure expected the smallest lattice size (4 by 5 μm) would induce the least encapsulation. Comparison between probe designs indicated differences in encapsulation and neuronal loss was insignificant. Also, the qualitative histology inside the lattice region usually had a similar response as found around the shank. Thus, we believe our hypothesis about the lattice size is incorrect in this application. While both hypotheses were founded on the same principal of a mitigation of mechanotransduction, the tissue reactivity inside the lattice region has several confounding factors. First we point out that the differences in lattice width also effected the flexibility and surface properties. Most importantly, however, we believe a lattice structure presents a very different mechanical interface than a solid structure (i.e., shank). The brain is continually pulsating due to vascular and respiratory oscillations, and so small relative movement (micromotion) between a probe and tissue induces some level of strain (Goldstein and Salcman 1973; Subbaroyan, Martin et al. 2005; Gilletti and Mushuswamy 2006). Recently it was reported that the pial surface in the rat oscillates by as much as 30 μm during respiration (Gilletti and Mushuswamy 2006). This evidence of micromotion suggests that compressive forces and not just shear

forces are at play within the lattice regions. Also, stress may be localized at inside edges and corners. The support arms and lateral edge were identical in size, but a consistent difference in reactivity was evident (Fig. 2-7,2-8, 2-9, 2-10), so more than size was influencing local reactivity. In brief, any benefits of the lattice and its small features could have been counterbalanced by the mechanical stresses due to micromotion. For future studies, longitudinal rather than transverse sections would provide improved visualization of the lattice structure and the resulting reactivity.

Despite considerable tissue reactivity inside the lattice region, several advantages may exist for an open-architecture design. The open-architecture may (1) provide improved tissue integration, (2) improve diffusion in local tissue, and (3) re-establish communication between either neurons or astrocytes that were initially severed during insertion. Liu and McCreery (1999, 2006) reported that neuronal stability increases with time post-implant and is believed to be the result of tissue encapsulation anchoring the probes in place (Liu, McCreery et al. 1999; Liu, McCreery et al. 2006). It is reasonable to suggest that a lattice design will quicken the stabilization process (normally 2-3 months), which is an important factor in brain-machine applications. Normal forces inside the lattice structure should reduce probe migration. Re-establishing more neuronal and astrocytic (Ca2+ gap junctions) communication after injury both around and through the probe may be important for maintaining functional neurons. The lattice design would, in theory, enable more cell-cell contact. These last two effects would ideally mitigate the loss in nearby neuronal activity that has been hypothesized to reduce electrode function

(Merrill and Tresco 2005). Further research is needed to characterize the mechanical and cellular interactions in and around a lattice structure especially when tethering is used, but this design concept is promising.

The double label immunostaining revealed two different types of glial reactivity. The first and more benevolent was a thin boundary of activated microglia at the interface intermingled with hypertrophied astrocytic processes. Unlike activated microglia, the hypertrophied astrocytes usually coexisted with neurons. This first type characterized the tissue about the lateral edge and only occasionally the region about the shank. The second type of reactive tissue was a noticeably thicker capsular region devoid of GFAP, neurofilament, and NeuN but always OX-42 positive and often fibronectin and laminin positive as well. Here the neuronal loss and nonneuronal encapsulation is most evident. However, the variability at the lateral edge of these probes was far less. The tissue around the lateral edge was consistently GFAP positive, and usually laminin negative and fibronectin negative. Further, microglia and other nonneuronal cells did not conform to the edge of the structure and thus may contribute less to the electrical impedance between this point on the probe and a distant neuron.

One theory that could explain the two types of glial tissue around the shank of the probe is the presence or lack of meningeal cells. Meningeal cells have been reported to play an active role in stab wound injuries and form an "accessory glia limitans" (Fawcett and Asher 1999; Shearer and Fawcett 2001; Bundesen, Scheel et al. 2003; Shearer, Niclou et al. 2003). Some have suggested their presence around neural probes (Cui, Lee et al. 2001;

Kim, Hitchcock et al. 2004). The presence of fibronectin+/OX-42- tissue suggests that some of the nonneuronal nuclei may be fibroblasts of meningeal origin. Their presence would explain why astrocytes seemingly circumscribe the tissue several to tens of microns from the shank, and why some tissue is fibronectin+ but not OX-42+ (Fig. 2-9). This is important because the existence of fibroblasts and the resulting astrocyte-menengial interface may further increase the impedance between the electrode and spiking neurons (Merrill and Tresco 2005).

Regarding the fabrication of these structures, we chose a substrate of poly-para-xylylene (specifically parylene-C) for several reasons: (1) microfabrication techniques are well established, (2) Class VI USP biocompatibility rating, (3) excellent insulating properties(Loeb, Peck et al. 1995), (4) low water uptake of 0.06%, (5) elongation at break is 200%(Fortin and Lu 2004), and (6) a polymer probe can be left in situ to improve the spatial resolution of the histological analysis. While the probe surface is parylene, the core of the shank consists of SU-8, an epoxy based photoresist that has been well characterized. This material can achieve thick layers in one application whereas parylene is typically deposited less than 10 μm each run. SU-8 is also reported to be non-cytotoxic (Kotzar, Freas et al. 2002; Voskerician, Shive et al. 2003). However, other non-cytotoxic materials such as silicon dioxide, silicon, and polyimide to name a few, would be expected to confer the same results if designed with similar dimensions.

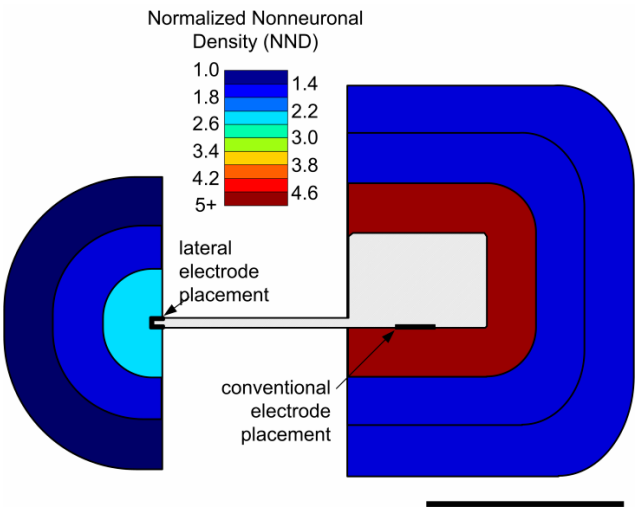

Figure 2.11 A graphical illustration of the importance of electrode placement. The graph shows the regions of tissue and the corresponding average nonneuronal density for all probe types (data taken from Fig. 5(b)). Regardless of probe type, the histological results indicated that the best electrode placement would be at the lateral edge. All probes tested had an identical footprint, as seen in a transverse cross-section. Scale = 100 µm.

The pattern of cellular encapsulation and neuronal loss suggests an electrode site design that wraps-around the perimeter. To effectively use the limited substrate at the perimeter around a neural probe or biosensor in the CNS, the electrode surface should be on three sides of the probe (Fig. 2.11, data taken from Fig. 2-6(b)). This would also maximize surface area facing healthy tissue. Another benefit of such a design would be an increase in the sensor viewing radius from 180 degrees to almost 360 degrees because there is less shielding (Moffitt and McIntyre 2005). However, there are two possible difficulties: (1) the fabrication complexity of creating a three dimensional electrode on a planar substrate, and (2) the size and surface limitation imposed may reduce sensitivity. In the case of a neural probe, we believe these are attainable engineering goals. Regarding the former concern, one may use electroplating to create a thick electrode, which is commonly done

with contact vias in integrated and printed circuits. To address the latter, the effective surface area can be greatly increased with the use of platinum black (Ilic, Czaplewski et al. 2000), oxidized iridium (Lee, Whang et al. 2002), or conductive polymers . In some applications, such as recording spike activity, sensitivity is expected to increase with decreased surface area.

2.6 Conclusions

Quantification of high resolution confocal images around intact probe structures revealed that encapsulating cell density within 25 μm of a thin lateral structure is reduced to almost one-third relative to the shank. The difference in neuronal loss was also significant. Furthermore, activated microglia and protein deposition is greatly reduced at this surface. Also, this study proves these probes are mechanically robust and practical as neural probes, despite utilizing a polymer substrate with subcellular dimensions.

We conclude that the ideal electrode placement for the tested probe designs is on the outermost edge of a 5-μm thick platform extending far from the probe shank. These results suggest it would be worthwhile to implement this alternative neural probe design in the CNS. Investigating the effect of subcellular dimensions and electrode placement in other biosensor designs should also be considered.

Acknowledgement

The authors acknowledge Dr. David Pellinen for fabrication advice and training and Dr. William Shain for reviewing the manuscript. The authors also thank Dr. Jeyakumar Subbaroyan, Erin Purcell, Kip Ludwig and other members of the Neural Engineering Laboratory and the Center for Neural Communication Technology for technical assistance and discussion. The staff at the Michigan Nanofabrication Facility and the Microscopy and Imaging Laboratory provided excellent support. Funding for this research was provided in part by the National Institute for Biomedical Imaging and Bioengineering (NIBIB) grant P41 EB002030 and by the Engineering Research Centers program of the National Science Foundation under NSF Award Number EEC-9986866.

References

Bernatchez, S. F., P. J. Parks, et al. (1996). "Interaction of macrophages with fibrous materials in vitro." Biomaterials 17(21): 2077-86.

Biran, R., D. C. Martin, et al. (2005). "Neuronal cell loss accompanies the brain tissue response to chronically implanted silicon microelectrode arrays." Exp Neurol 195(1): 115-26.

Bjornsson, C. S., S. J. Oh, et al. (2006). "Effects of insertion conditions on tissue strain and vascular damage during neuroprosthetic device insertion." J Neural Engineering 3(10): 196–207.

Bundesen, L. Q., T. A. Scheel, et al. (2003). "Ephrin-B2 and EphB2 regulation of astrocyte-meningeal fibroblast interactions in response to spinal cord lesions in adult rats." J Neurosci 23(21): 7789-800.

Buzsaki, G. (2004). "Large-scale recording of neuronal ensembles." Nat Neurosci 7(5): 446-51.

Chen, C. S., M. Mrksich, et al. (1997). "Geometric control of cell life and death." Science 276(5317): 1425-8.

Chen, C. S., J. Tan, et al. (2004). "Mechanotransduction at cell-matrix and cell-cell contacts." Annu Rev Biomed Eng 6: 275-302.

Cui, X., V. A. Lee, et al. (2001). "Surface modification of neural recording electrodes with conducting polymer/biomolecule blends." J Biomed Mater Res 56(2): 261-72.

Edell, D. J., V. V. Toi, et al. (1992). "Factors influencing the biocompatibility of insertable silicon microshafts in cerebral cortex." IEEE Trans Biomed Eng 39(6): 635-43.

Fawcett, J. W. and R. A. Asher (1999). "The glial scar and central nervous system repair." Brain Res Bull 49(6): 377-91.

Fortin, J. B. and T. M. Lu (2004). Chemical vapor deposition polymerization : the growth and properties of parylene thin films. Boston, Kluwer Academic Publishers.

Gilletti, A. and J. Mushuswamy (2006). "Brain micromotion around implants in the somatosensory corex of rats." J Neural Eng 3: 189-195.

Goldstein, S. R. and M. Salcman (1973). "Mechanical factors in the design of chronic recording intracortical microelectrodes." IEEE Trans Biomed Eng 20(4): 260-9.

Hampton, D. W., K. E. Rhodes, et al. (2004). "The responses of oligodendrocyte precursor cells, astrocytes and microglia to a cortical stab injury, in the brain." Neuroscience 127(4): 813-20.

He, W. and R. V. Bellamkonda (2005). "Nanoscale neuro-integrative coatings for neural implants." Biomaterials 26(16): 2983-90.

Hochberg, L. R., M. D. Serruya, et al. (2006). "Neuronal ensemble control of prosthetic devices by a human with tetraplegia." Nature 442(7099): 164-71.

Ilic, B., D. Czaplewski, et al. (2000). "Preparation and characterization of platinum black electrodes." Journal of Materials Science 35(14): 3447-57.

Johnson, M. D., K. J. Otto, et al. (2005). "Repeated voltage biasing improves unit recordings by reducing resistive tissue impedances." IEEE Trans Neural Syst Rehabil Eng 13(2): 160-5.

Kim, D. H. and D. C. Martin (2006). "Sustained release of dexamethasone from hydrophilic matrices using PLGA nanoparticles for neural drug delivery." Biomaterials 27(15): 3031-7.

Kim, Y. T., R. W. Hitchcock, et al. (2004). "Chronic response of adult rat brain tissue to implants anchored to the skull." Biomaterials 25(12): 2229-37.

Kotzar, G., M. Freas, et al. (2002). "Evaluation of MEMS materials of construction for implantable medical devices." Biomaterials 23(13): 2737-50.

Lee, I.-S., C.-N. Whang, et al. (2002). "Characterization of iridium film as a stimulating neural electrode." Biomaterials 23(11): 2375-80.

Lefurge, T., E. Goodall, et al. (1991). "Chronically implanted intrafascicular recording electrodes." Ann Biomed Eng 19(2): 197-207.

Liu, X., D. B. McCreery, et al. (2006). "Evaluation of the stability of intracortical microelectrode arrays." IEEE Trans Neural Syst Rehabil Eng 14(1): 91-100.

Liu, X., D. B. McCreery, et al. (1999). "Stability of the interface between neural tissue and chronically implanted intracortical microelectrodes." IEEE Transactions on Rehabilitation Engineering 7(3): 315-26.

Loeb, G. E., R. A. Peck, et al. (1995). "Toward the ultimate metal microelectrode." J Neurosci Methods 63(1-2): 175-83.

Ludwig, K. A., J. D. Uram, et al. (2006). "Chronic neural recordings using silicon microelectrode arrays electrochemically deposited with a poly(3,4-ethylenedioxythiophene) (PEDOT) film." J Neural Eng 3(1): 59-70.

Maynard, E. M., E. Fernandez, et al. (2000). "A technique to prevent dural adhesions to chronically implanted microelectrode arrays." J Neurosci Methods 97(2): 93-101.

McCreery, D. B., W. F. Agnew, et al. (1987). "Electrical characteristics of chronically implanted platinum-iridium electrodes." IEEE Transactions on Biomedical Engineering 34(9): 664-8.

Merrill, D. R. and P. A. Tresco (2005). "Impedance characterization of microarray recording electrodes in vitro." IEEE Trans Biomed Eng 52(11): 1960-5.

Moffitt, M. A. and C. C. McIntyre (2005). "Model-based analysis of cortical recording with silicon microelectrodes." Clin Neurophysiol 116(9): 2240-50.

Nicholson, C. and E. Sykova (1998). "Extracellular space structure revealed by diffusion analysis." Trends Neurosci 21(5): 207-15.

Roitbak, T. and E. Sykova (1999). "Diffusion barriers evoked in the rat cortex by reactive astrogliosis." Glia 28(1): 40-8.

Rousche, P. J. and R. A. Normann (1992). "A method for pneumatically inserting an array of penetrating electrodes into cortical tissue." Ann Biomed Eng 20(4): 413-22.

Rousche, P. J. and R. A. Normann (1998). "Chronic recording capability of the Utah Intracortical Electrode Array in cat sensory cortex." Journal of Neuroscience Methods 82(1): 1-15.

Sanders, J. E., C. E. Stiles, et al. (2000). "Tissue response to single-polymer fibers of varying diameters: evaluation of fibrous encapsulation and macrophage density." J Biomed Mater Res 52(1): 231-7.

Santucci, D. M., J. D. Kralik, et al. (2005). "Frontal and parietal cortical ensembles predict single-trial muscle activity during reaching movements in primates." Eur J Neurosci 22(6): 1529-40.

Schmidt, E. M., J. S. McIntosh, et al. (1988). "Long-term implants of Parylene-C coated microelectrodes." Med Biol Eng Comput 26(1): 96-101.

Schwartz, A. B. (2004). "Cortical neural prosthetics." Annu Rev Neurosci 27: 487-507.

Schwartz, M., O. Butovsky, et al. (2006). "Microglial phenotype: is the commitment reversible?" Trends Neurosci 29(2): 68-74.

Shain, W., L. Spataro, et al. (2003). "Controlling cellular reactive responses around neural prosthetic devices using peripheral and local intervention strategies." IEEE Trans Neural Syst Rehabil Eng 11(2): 186-8.

Shearer, M. C. and J. W. Fawcett (2001). "The astrocyte/meningeal cell interface--a barrier to successful nerve regeneration?" Cell Tissue Res 305(2): 267-73.

Shearer, M. C., S. P. Niclou, et al. (2003). "The astrocyte/meningeal cell interface is a barrier to neurite outgrowth which can be overcome by manipulation of inhibitory molecules or axonal signalling pathways." Mol Cell Neurosci 24(4): 913-25.

Subbaroyan, J., D. C. Martin, et al. (2005). "A finite-element model of the mechanical effects of implantable microelectrodes in the cerebral cortex." J Neural Eng 2(4): 103-13.

Suner, S., M. R. Fellows, et al. (2005). "Reliability of signals from a chronically implanted, silicon-based electrode array in non-human primate primary motor cortex." IEEE Trans Neural Syst Rehabil Eng 13(4): 524-41.

Szarowski, D. H., M. D. Andersen, et al. (2003). "Brain responses to micro-machined silicon devices." Brain Res 983(1-2): 23-35.

Turner, A. M., N. Dowell, et al. (2000). "Attachment of astroglial cells to microfabricated pillar arrays of different geometries." J Biomed Mater Res 51(3): 430-41.

Turner, J. N., W. Shain, et al. (1999). "Cerebral astrocyte response to micromachined silicon implants." Exp Neurol 156(1): 33-49.

Vetter, R. J., J. C. Williams, et al. (2004). "Chronic neural recording using silicon-substrate microelectrode arrays implanted in cerebral cortex." IEEE Trans Biomed Eng 51(6): 896-904.

Voskerician, G., M. S. Shive, et al. (2003). "Biocompatibility and biofouling of MEMS drug delivery devices." Biomaterials 24(11): 1959-67.

Williams, J. C., R. L. Rennaker, et al. (1999). "Long-term neural recording characteristics of wire microelectrode arrays implanted in cerebral cortex." Brain Res Brain Res Protoc 4(3): 303-13.

Zhong, Y. and R. V. Bellamkonda (2005). "Controlled release of anti-inflammatory agent alpha-MSH from neural implants." J Control Release 106(3): 309-18.

CHAPTER 3 Improved Insulation Performance in Bioelectrical Devices With a Reactive Parylene Interface

3.1 Abstract

Parylene-C (poly-chloro-p-xylylene) is almost an ideal material for use in an implantable, microfabricated device. It is hydrophobic, conformally deposited, has a low dielectric constant, and superb biocompatibility. Yet for many bioelectrical applications, its poor wet adhesion may be an impassable shortcoming.

This research contrasts parylene-C and reactive parylene (poly-X-p-xylylene or PPX-X) layers using long-term electrical soak and adhesion tests. The reactive parylene was made of complementary derivatives having aldehyde and aminomethyl side groups (PPX-CHO and PPX-CH_2NH_2 respectively). These functional groups have previously been shown to react covalently after heating. This is the first report of PPX-CHO or PPX-CH_2NH_2 in a bioelectrical application. Electrical testing was conducted in saline at 37°C on interdigitated electrodes with either parylene-C or reactive parylene as the metal layer interface. Electrochemical impedance spectroscopy results showed that reactive parylene devices maintained the highest impedance. The impedance of the heat-treated PPX-X devices was 800% greater at 10 kHz and 70% greater at 1Hz relative to heated parylene-C controls after 60 days. Heat treatment proved to be critical to the impedance of both parylene-C and the reactive parylene. Transverse impedance, unlike the inter-electrode or lateral impedance, remained high for all groups tested, which suggested good bulk properties and minimal or no defects. Adhesion measurements showed improved wet metal adhesion for PPX-X, which corresponds well with its excellent high frequency performance. We discuss the

implication of these results on testing, microfabrication, and long-term viability of an implantable bioMEMS device.

3.2 Introduction

Commercially available implantable electronics, e.g. pacemaker, stimulator, are typically packaged inside of a laser welded, inorganic canister (Bauer, Russek et al. 2004). Yet many applications require micro-scaled sensors and actuators and therefore are not afforded the luxury of hermetic packaging (Kotzar, Freas et al. 2002). Next generation implantable biosensors, smart drug delivery systems, and neuroprostheses, for example, will need to maintain long-term insulation using fully exposed microfabricated structures.

Interfacial boundary layers that form between each material in a well insulated structure should be clean, have similar surface energies, and possess adequate adhesion strength to withstand the intended environment (Yamagishi 1991). On one hand, polymers are attractive because of a diversity of bulk properties, and alterable surface chemistry. On the other, polymers are inherently leaky to water, oxygen, and salts compared to high temperature inorganics (Massey, Plastics Design Library. et al. 2003; Weaver, Kwong et al. 2006). As such, we must ensure polymer systems create interfacial boundaries that are stable in the presence of water, oxygen, and ions. This issue especially important for a microfabricated structure being used in a bioelectrical application. By way of illustration, first consider a polymer coating on two suspended metal wires that form an interconnect on a generic sensor or actuator (Fig. 3.1A). When this device is in biological fluid or

tissue, then two critical electrical measurements should be known—the lateral impedance, Z_{lat}, and transverse impedance, Z_{trans}. Z_{lat} is inversely related to crosstalk in this circuit. Z_{trans} is inversely related to signal loss via "shunting". Notice that one interfacial boundary exists for both measurements. By contrast, when a similar interconnect is created using planar microfabrication, another interfacial boundary is introduced (Fig. 3.1B). In the first example of coated metal wires, a poorly adhering interfacial boundary will only cause a dramatic decline in Z_{lat} or Z_{trans} if the metal begins to corrode. Otherwise, the impedance will be dominated by the geometry of the circuit and the bulk properties of the material. However, in the example of a bioMEMS interconnect, Z_{lat} in particular can have a striking decline in impedance if the polymer-metal and polymer-polymer boundaries are compromised, thereby enabling a low resistive pathway. This study used an interdigitated electrode to measure both Z_{lat} and Z_{trans}.

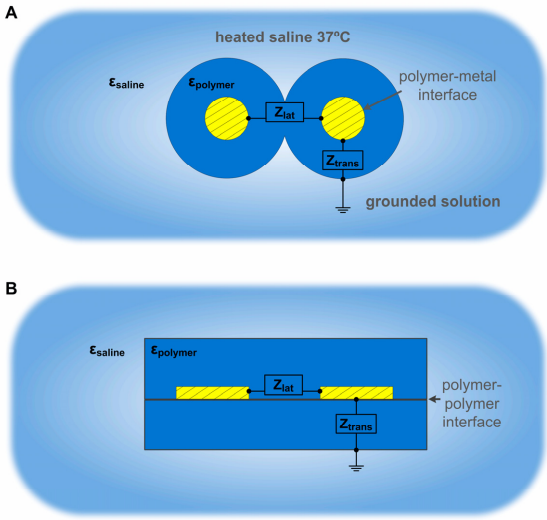

Figure 3.1 Challenge of using microfabricated implantable electronics. (A) Cross-section of a coating over two free standing metal wires. Lateral and transverse impedance in this example are predominantly sensitive to the bulk properties, such as $\varepsilon_{polymer}$. (B) A microfabricated polymer-metal-polymer structure. Z_{lat} will show far greater sensitivity to poor adhesion at the polymer-polymer or polymer-metal interface than Z_{trans}.

Parylene-C has a recognized issue of poor wet metal adhesion (Sadhir, James et al. 1981; Sharma and Yasuda 1982; Yamagishi 1991; Yasuda, Chun et al. 1996; Yasuda, Yu et al. 2001; Yu, Deffeyes et al. 2001), which should raise caution over its use in biomedical microdevices. Nonetheless, it still has many desirable properties. Parylene-C is chemically inert, has a low dielectric constant ($\varepsilon_r = 3.1$), and the highest biocompatibility certification, USP Class VI. It is synthesized from a low-molecular weight dimer, dichloro-di(pxylylene) using a solvent-less polymerization process. Critically important in microfabrication, one can generate conformal, pinhole free films that are subsequently dry-etched using an oxygen plasma.

Parylene-C has been used in implantable sensors and actuators. Most notably, parylene-C has been successfully used as a coating in neural recording arrays (Schmidt, McIntosh et al. 1988; Suner, Fellows et al. 2005). A few researchers have also used parylene in implantable microfabrication applications. One group used an oxygen plasma to clean and roughen between parylene deposition (Jun, Xing et al. 2001; Pornsin-Sirirak, Liger et al. 2002), and more recently used heat treatment to improve long-term electrical resistivity through the parylene-C film (Li, Rodger et al. 2005; Rodger and Tai 2005). Heat treatment combined with pressure was shown by other groups to improve parylene-parylene adhesion, which is believed to mechanically interlock polymer chains at the interface (Kim and Najafi 2005 ; Ziegler, Suzuki et al. 2006).

One author's research group (JL) has introduced novel "reactive parylene" films by functionalizing the paracyclophane dimer with a variety of molecules to modify interfacial properties (Jörg Lahann 1998; Lahann, Balcells et al. 2003; Lahann 2006). Recent research has used complementary reactive parylene films having aldehyde and aminomethyl groups, PPX-CHO and PPX-CH_2NH_2 respectively, to improve adhesion strength of PDMS on silicon (Chen, McClelland et al. 2008). Summed frequency generation (SFG) was used to verify that the functional bonds, C-N, N-H, and C=O, disappeared after heating at 140°C for 3 hours. We use these same complementary reactive parylene films (PPX-X) in electrical and mechanical test structures.

Wide spectrum impedance data for long-term soak tests using microfabricated parylene-C devices is lacking. This study compares a reactive parylene to parylene-C using long-

term electrical soak tests and adhesion tests. Two important techniques are utilized: (1) electrochemical impedance spectroscopy and (2) an interdigitated electrode sensor. EIS is also commonly used to evaluate the longevity and degradation kinetics of many polymer-metal systems (Akbarinezhad 2008), including paint and epoxy coatings. EIS is most effective when coupled with "under-coating" or interfacial measurements (Sheppard, Day et al. 1982; van Westing, Ferrari et al. 1994), which are possible with an interdigitated electrode. Broad frequency analysis provides greater relevance to a variety of bioelectrical applications, e.g. biosensors (<10 Hz frequency band) or neural recording and stimulation (500-5000 Hz frequency band).

This is the first report of a reactive or functionalized parylene material in a bioelectrical application. Reactive parylene was shown to be an improved electrical interface material relative to parylene-C (as used here) due to better wet metal adhesion. We are only beginning to understand and optimize the potential of reactive or functionalized parylene in implantable bioelectrical applications.

3.3 . Design and fabrication

3.3.1 Interdigitated electrode fabrication

The interdigitated electrode (IDE) structure consisted of long, widely spaced leads in a "Y" configuration (Fig. 3.3A). The large separation between bond pads was designed to reduce stray capacitance. The overlapping metal region was 5-mm tall x 700-µm wide. Each electrode tine was 1.5-µm wide and a 4.5-µm gap. The total length of the overlapping metal trace was 292,000 µm per half. Metal was buried in a parylene

substrate, similar to a stripline configuration in printed circuit boards. An alternative geometry was 3.0-µm track and a 3.0-µm gap. The results for the 3/3 geometry are discussed in section 3.4.

The microfabrication for these structures required two masks and was conducted on 4" silicon wafers in the Lurie Nanofabrication Facility. For simplicity, we describe the process in four major steps (Fig. 3.2A). **Fig. 3.2-A1**. One micron of SiO_2 was thermally grown on the wafer. An adhesion promoter A-174 was vaporized onto the wafer surface then parylene-C was CVD polymerized (PDS2010, Specialty Coating System) on the oxide. Deposition was 2.4-µm thick for experimental wafers, i.e. those to receive PPX-X, or 2.5-µm thick for control wafers. **Fig. 3.2-A2**. Next we briefly etched the parylene-C surface with an oxygen plasma for 30 sec at 80W (March Asher) in preparation for the next polymerization step. Oxygen plasma etching has been reported as a technique to clean and roughen a parylene undercoating (Jun, Xing et al. 2001; Pornsin-Sirirak, Liger et al. 2002). It has also been suggested as way to create free radicals on a polymer surface that can form covalent bonds during parylene polymerization (Yamagishi 1991). This plasma cleaning step occurred before each CVD step throughout the process to ensure consistency between layers. Poly(4-formyl-p-xylylene-co-p-xylylene), PPX-CHO, was CVD polymerized using custom built equipment described previously (Nandivada, Chen et al. 2005), although could be deposited with commercial equipment as well. 90-140 nm of PPX-CHO was deposited on the experimental wafers only. Precursor synthesis was conducted in an author's laboratory (JL) with further details described elsewhere

(Lahann, Klee et al. 1998; Nandivada, Chen et al. 2005). The strong carbonyl stretch at 1688 cm^{-1} in the IR spectrum was used to confirm the presence of the aldehyde group after deposition (Fig. B.S1A). Thickness was determined with a profilometer. Next, metal lift-off (SPR220) was used to pattern the Cr/Au/Cr (100/4000/100 Å). Metal was deposited with an e-beam evaporator (Enerjet). The resist was removed with 1112A (Shipley Microposit Remover). Following lift-off, wafers were immediately cleaned in acetone, IPA, then spin rinsed for 5 minutes. **Fig. 3.2-A3**. Poly(4-aminomethyl-p-xylylene-co-p-xylylene), PPX-CH_2NH_2, was CVD polymerized on experimental wafers. Precursor synthesis is described elsewhere (Klee, Weiss et al. 2004). Deposition of PPX-CH_2NH_2 was conducted using the same parameters as PPX-CHO, and profilometric measurements indicated film thicknesses of 90-130 nm thick. The peaks at 3361 and 3301 cm^{-1} in the IR spectrum were used to confirm the presence of the N-H bonds after deposition (Fig. 3.S1B). Next, parylene-C was deposited on experimental and control wafers either 2.4 µm or 2.5 µm, respectively. **Fig. 3.2-A4**. Titanium was deposited 1000-Å thick (evaporator) and patterned (SPR220) to define the structural mask during oxygen plasma etching (not shown). After O_2 plasma etching (Plasmatherm 790), chromium was removed from the exposed bond pads by a wet etch (Cyantek CR-14) for 8 sec. The titanium and SiO_2 (sacrificial release layer) were etched in DI:HF:H_2O_2 (3:3:1) for ~1 hour. Released test structures were filtered out and repeatedly rinsed with ~2L of DI until the pH of the rinse water was normal. Resulting devices were air dried and ready for assembly (Fig. 3.2-A4). The thickness of dielectric material over metal was 2.3 to 2.5 µm per side for all devices. **IDE Assembly and Preparation**. IDE test structures were

mounted on a custom PCB employing gold ball studs with thermosonic bonding (Meyer, Stieglitz et al. 2001). A protective coating of silicone (MED-4211, Nusil Technology) was carefully applied over each end of the IDE ball bond regions. An additional 100 nm of parylene-C was deposited onto all IDEs to coat any pinhole or edge defects. "Heated PPX-X" and "Heated CNTL" (parylene-C) samples were heated in an oven at 140°C for 3 hours.

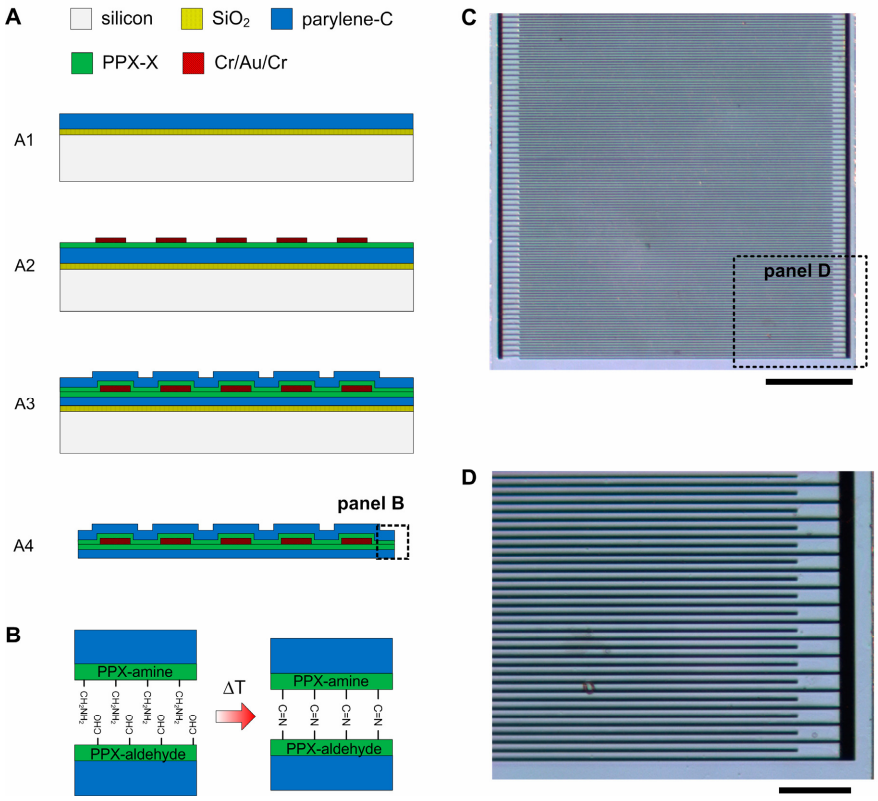

Figure 3.2. (A1-A4) Major microfabrication steps of a parylene interdigitated electrode or IDE with reactive parylene (PPX-X) nanofilms. (A4) Released crosssection of final device. The PPX-X layers were omitted in control devices (not shown). (B) Schematic of reaction using complementary PPX-CHO and PPX-CH_2NH_2 layers (Chen 2008). ΔT=140°C for 3 hrs. (C) Micrograph of the bottom half of an IDE. Scale = 200µm. (D) High magnification of IDE. Trace width = 1.5 µm, space = 4.5 µm. Scale = 50µm. Region beyond device in panels C, D cropped for contrast.

3.3.2 *Soak Testing*

The electrochemical impedance measurements were performed using an Autolab PGSTAT 12 (Eco Chemie) with associated Frequency Response Analyzer software. The spectral range was 100,000 to 1 Hz, except dry samples which were limited to 10 Hz given the high impedance of these devices. 5 frequencies were measured per decade on a logarithmic scale (26 frequencies total). A two electrode measurement was made by connecting the counter to the reference electrode input, and the working to the sense electrode. The sinusoidal voltage amplitude was 25 mV. A large platinum electrode was used as the counter electrode in measurements of Z_{trans}. All impedance measurements were carried out in a Faraday cage in order to minimize external interference. Transverse, Z_{trans}, and lateral impedance, Z_{lat}, testing was collected on the first hour, first day, and then every 5^{th} day or more. Given the low capacitance values of dry test structures (Table 3.3), care was taken to ensure cables were routed and spaced in a repeatable manner throughout the study. The baseline capacitance was determined to be 3.1 pF, which included cables, connectors, and a PCB (without the IDE).

A soak chamber was created using glass jars and a custom machined nylon lid to hold water above the IDE sensor level. Each lid was sealed from the outside onto the jar with gasket sealer. Assembled devices were mounted through openings in a custom soak chamber lid and sealed with silicone from the top (Fig. 3.3). The IDE active area was

completely submerged throughout the study. The soak chamber was filled with phosphate buffered saline (1X) with 0.1% sodium azide. The PBS solution was changed every twenty days to minimize the possible effects of evaporation, precipitation, and oxygen changes. Eight samples were loaded into each soak chamber. Multiple soak chambers were held at 37°C for 60 days in a large temperature-controlled water bath. Temperature range during data collection was 35-39°C.

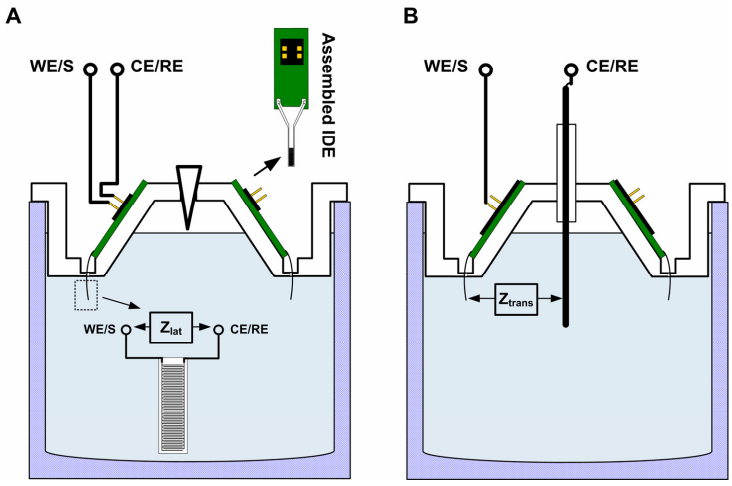

Figure 3.3 Soak test setup. Cross-section through a glass jar containing up to eight IDEs for long-term EIS measurements. (A) Lateral impedance configuration. Z_{lat} was the impedance of the interdigitated electrode. (B) Transverse impedance configuration. Z_{trans} was the impedance between one-half of the IDE and a large counter electrode in solution. Both Z_{lat} and Z_{trans} used a two electrode configuration.

3.3.3 Adhesion Testing

Two peel-test structures were fabricated and the resulting cross-section and angle of separation is illustrated in Fig. 3.4. Adhesion forces were measured quantitatively using a load cell (Sensotec Model 31, Honeywell). One half of each structure was fixed and the

other pulled apart using a programmable piezoelectric micromotor (M-230, Physik Instrumente) as illustrated (Fig. 3.S2). Optical examination and profilometric measurements were used to conclude the plane of separation.

Microfabrication of parylene-on-metal structures. Evaporate 500 Å of chromium on a 4" silicon wafer. CVD polymerization of parylene (PPX-CHO or parylene-C) 100-nm thick (actual 75 to 135 nm). Pattern a sacrificial separation layer of SPR220 photoresist. Surface cleaning in oxygen plasma (March Asher) for 30 sec at 80W. CVD parylene (PPX-CH_2NH_2 or parylene-C) 100-nm thick (actual 80 to 135 μm). Repeat oxygen plasma and then CVD parylene-C 5-μm thick four times until 20-μm thick. Repeated oxygen plasma treatment between each layer. This thickness was necessary to prevent breakage during the adhesion test. The wafer was diced into 7.5-mm wide pieces. The length was greater than 20 mm. Sacrificial photoresist was removed by dipping only the resist end of the sample into acetone for 2 hours then rinsed in IPA. Samples dried at least one day before testing.

Microfabrication of parylene-on-parylene structures. This structure was process was identical to the IDE structures except the inclusion of a Ti sacrificial layer and the omission of the metal electrode. After depositing the SiO_2 and first 5 μm of parylene-C, a parylene 100 nm film was deposited as before (PPX-CHO or parylene-C). Then a Ti sacrificial layer was deposited (1000 Å). Patterned the Ti using SPR220 and a wet etchant of 20:1:1 DI:HF:H_2O_2. Deposited another 100 nm parylene film (PPX-CH_2NH_2 or parylene-C) followed by another 5 μm of parylene-C. The final structure was defined by

a Ti mask, etched with an O_2 plasma, and then released in DI:HF:H_2O_2 (3:3:1) for ~1 hour. The peel test structures (3mm x 20mm) were air dried for several days.

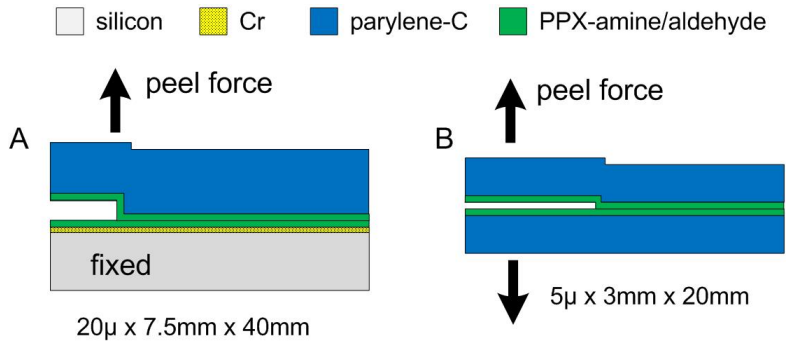

Figure 3.4 Two peel-test structures used to evaluate adhesion force. (A) Parylene-on-metal structure with a photoresist sacrificial layer (not shown) and peeled at 90 degrees. (B) Parylene-on-parylene structure with a titanium sacrificial layer (not shown) and peeled at 180 degrees. Fabrication details are in 2.2. Labeled dimensions are thickness x width x length. Control pull-test structures substituted parylene-C in place of PPX-amine and PPX-aldehyde.

3.3.4 Circuit Modeling

The impedance measurements were fitted using Boukamp's program, EQUIVCRT (Boukamp 1986). Analysis of the impedance measurements were performed between 1 Hz and 100 kHz. Extracted capacitance values were used to verify the test structures had similar geometries and thus useful for comparison (Table 3.3). Dry IDEs not heat treated fit best using a parallel resistor and capacitor. Heated IDEs were fit to a simple constant phase element (CPE). The impedance of a CPE is defined as:

$$Z_{CPE} = \frac{1}{Y(j\omega)^n}$$

where j is an imaginary number, ω is angular frequency (rad), n is the CPE power, and Y is the CPE constant.

3.4 3. Results

3.4.1 Lateral impedance

Lateral impedance, Z_{lat}, was first measured before soaking began. All dry measurements resulted in similarly high impedance (Fig. 3.5A, red). Capacitance of the dry IDEs was also determined to be similar (21.6 ± 5.4 pF, Table 3.3) after fitting to an equivalent circuit model. Dry IDEs that were not heat treated resulted in a semi-circular arc on a Nyquist plot and a modest phase shift on a Bode plot (Fig. 3.5A). This is indicative of a simple resistor and capacitor in parallel (average error of 6.6%). Heated IDEs resulted in a unchanging phase so a constant phase element was used to estimate capacitance (average error of 1.9%). Z_{lat} values of dry structures (Fig. 3.5A, red) and the modeled capacitance (Table 3.3) indicated all variables were of similar geometry.

The soak response of Z_{lat} was measured in PBS 1X at 37°C over 60 days (Fig. 3.5A). Within one hour, all variables showed a decline in impedance in at least the low frequency spectrum. For frequencies greater than 10 kHz, the heated PPX-X cohort resulted in little impedance change whereas all other variables fell to one-third of the dry value or less. The unheated parylene-C (CNTL) and unheated PPX-X cohorts fell most dramatically in the first hour. Heating the control and PPX-X devices had an immediate and long-term beneficial effect over the entire spectrum (1-100,000 Hz). Note the dynamic nature of the unheated PPX-X devices. The breakpoint frequency (45° phase)

shifts toward low frequencies as time progresses while impedance increases. This pattern is reverse of a typical organic coating on metal (Akbarinezhad 2008).

A direct contrast of each cohort is shown for 1 hour and day 60 and includes the standard error for each (Fig. 3.6). The highest impedance was found in the heated PPX-X cohort (N=5) after the 60 day soak test. However, the heated parylene-C cohort (N=3) initially had higher impedance below 10 Hz. Another consistent trend is a higher impedance at higher frequencies of PPX-X devices relative to controls. Even the unheated PPX-X devices, despite the rapid decline at 1 Hz, had an order of magnitude advantage over the unheated control between 10-100 kHz. The frequency-dependent contrast between materials and the dynamic nature of the unheated PPX-X provide important clues to interpreting the physical model and failure mechanism.

A small sample of devices were individually tested in PBS 1X at room temperature to measure the immediate temporal response. The decline in impedance could be tracked on the scale of minutes (Fig. 3.7) which explained the difference between dry samples and the 1-hour time point. As before, the decline in impedance magnitude is greater at lower frequencies.

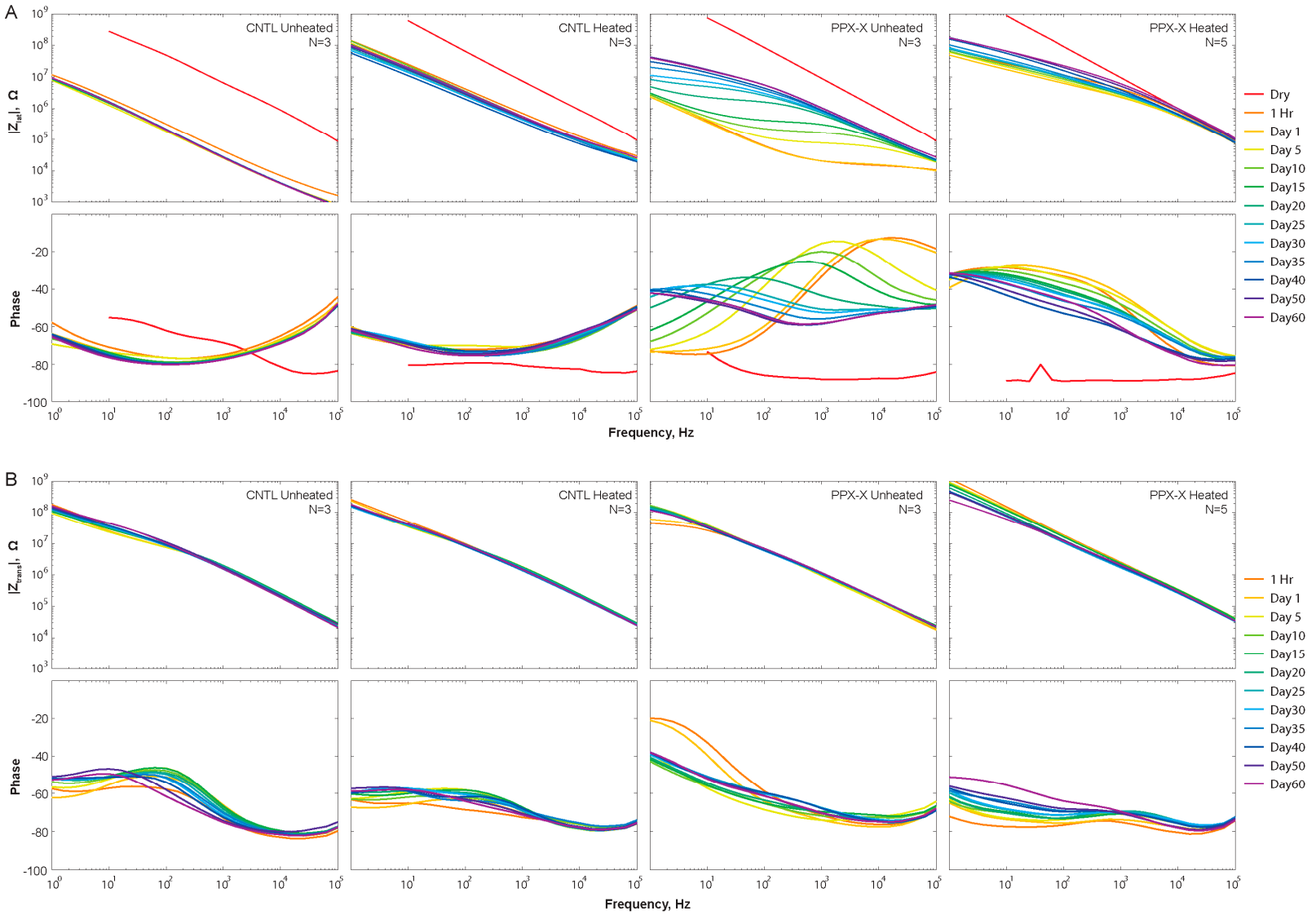

Figure 3.5. Bode plots displaying the temporal response to soaking in 1X PBS at 37°C. (A) Lateral impedance, Z_{lat}, and (B) transverse impedance, Z_{trans}. Variables from left to right are CNTL unheated, CNTL heated, PPX-X unheated, and PPX-X heated. Z_{lat} increased over time for unheated PPX-X although it never completely rebounded to the level of heated PPX-X.

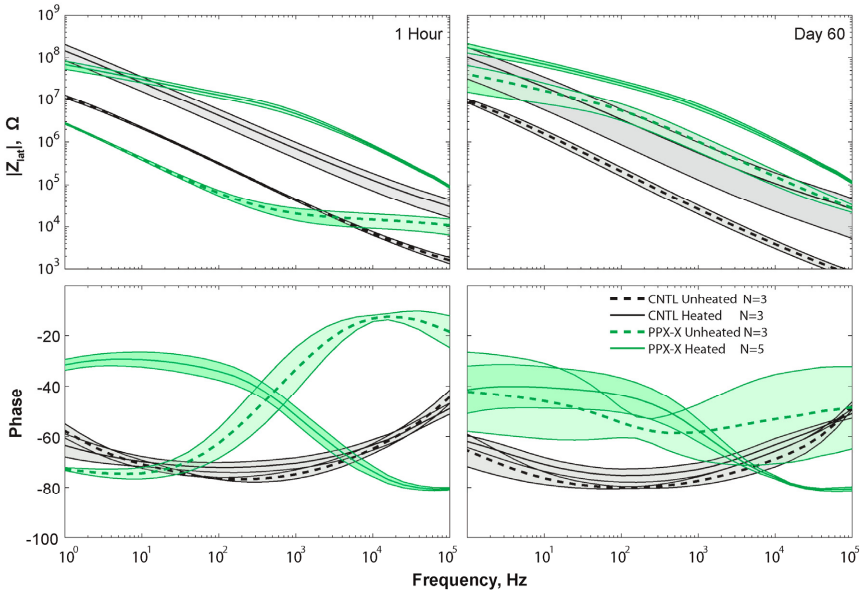

Figure 3.6 Single time point Bode plots of Z_{lat} at 1 hour and day 60. The shaded area around each variable represents standard error.

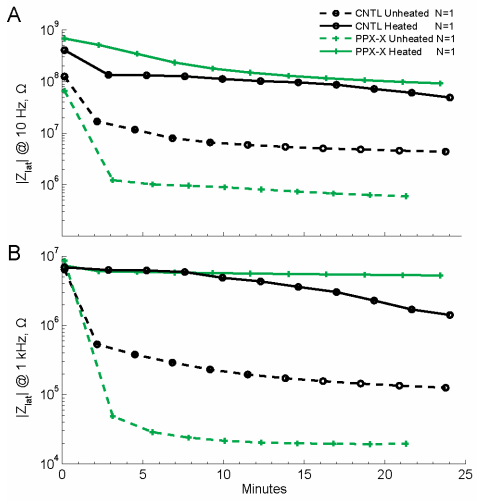

Figure 3.7 Example Z_{lat} impedance in first 20 minutes. (A) 10 Hz and (B) 1 kHz response of lateral impedance versus time while soaking at 22°C. First data point was the dry impedance magnitude.

3.4.2 Transverse impedance

Transverse impedance measured the resistivity and capacitance through the parylene coatings and saline to a large counter electrode. Z_{trans} was plotted below Z_{lat} with the same scale to allow for a contrast of these two measurements (Fig. 3.5B). The temporal changes were minute relative to Z_{lat}. These results show consistent, high impedance over time for each variable. Phase was also consistent and moderately capacitive for all variables. Unheated PPX-X initially had low impedance below 10 Hz but this rebounded to normal levels by day 5. It has been reported that a small defective area will produce a large decrease in impedance magnitude, i.e., defect area has a non-linear affect on impedance (Grundmeier, Schmidt et al. 2000). Therefore, transverse impedance results indicated that parylene formed a consistent coating with few or no defects. Z_{trans}, unlike Z_{lat}, showed no clear differentiation between variables.

3.4.3 Adhesion force testing

Two separate adhesion tests were performed. First we tested parylene-on-metal and then parylene-on-parylene (Fig. 3.4). Adhesion force was quantified by using a load cell in series with a programmable piezoelectric motor (Fig. 3.S2). The parylene-on-metal test included a stack of parylene deposited on chromium. Chromium, a commonly used adhesion layer, was also used as the metal adhesion layer in the interdigitated electrode. This test structure effectively measured the adhesion force of the weakest layer—either a parylene-parylene interface or a parylene-metal interface. Results are shown in Table 3.1 (N=5 for each cohort). All dry samples performed well. Samples were heated as before (3

hours at 140°C without oxygen purging) so increased brittleness was evident when the adhesion force was high. A significant difference became evident after soaking for 30 minutes in 1X PBS at 37°C. Soaked parylene-C samples could not be measured because the parylene-C stack separated from the chromium layer during handling. The wet PPX-X layers had improved adhesion, 2.4 g/mm when unheated and 14.9 g/mm after heating. Also, note that separation at the Cr/PPX-CHO interface only occurred in one of these samples. Optical images (Fig. 3.S3) and a profilometer were used to determine the plane of separation.

Table 3.1. Adhesion force of parylene stack on chromium (90° separation, N=5).

	Dry Force, g/mm	Separation[c]	Wet[a] Force, g/mm	Separation[c]
Parylene-C Unheated	24.1 ± 16.0	cohesive	0	Cr/ParC
Parylene-C Heated	>39.0 ± 9.1[b]	cohesive	0	Cr/ParC
PPX-X Unheated	33.6 ± 9.0	cohesive	2.4 ±1.8	CH_2NH_2/ParC
PPX-X Heated	>43.8 ± 8.8[b]	cohesive	14.9 ±13.9	CH_2NH_2/ParC or Cr/CHO

a: Wet adhesion protocol: soak structure in 1X PBS for 30 min at 37°C.
b: Tearing limited the adhesion force.
c: Images available in supplemental material, Fig. S3.

The second adhesion test was designed to isolate and measure the parylene-on-parylene interfaces. This test also differed from the first adhesion test in that the angle of separation was 180° and was exposed to hydrofluoric acid during processing. Wet adhesion strength was best for the heated parylene-C interface (Table 3.2). As before, brittleness of the sample increased presumably due to oxidation from the heat treatment. We would expect the adhesion force to be slightly underestimated when cohesive failure

occurred. Only heated parylene-C samples had a high, consistent adhesion strength. The heated PPX-X, had low adhesion strength but was stable whether dry or wet (0.3 g/mm). Determining the plane of separation was not possible for the parylene-on-parylene samples and therefore not reported.

Table 3.2. Adhesion force of parylene on parylene (180° separation).

	Dry Force, g/mm	N	Wet[a] Force, g/mm	N
Parylene-C Unheated	17.1 ± 0.9	4	1.22 ± 2.3	4
Parylene-C Heated	> 8.8 ± 8.7 [b]	3	> 10.5 ± 2.4 [b]	3
PPX-X Unheated	0.14 ± 0.01	4	0.16 ± 0.05	3
PPX-X Heated	0.3 ± 0.07	5	0.3 ± 0.02	3

a: Wet adhesion protocol: soak structure in 1X PBS for 30 min at 37°C.
b: Tearing limited the adhesion force.

3.4.4 Wet Etch Testing

Two wet etching methods of buried metal were performed during the normal course of fabrication, which provided a useful technique to compare the wettability at the polymer-metal interface. Following an 8 sec chromium wet etch (ceric and acetic acid in an aqueous solution) and 2 minute rinse, exposed metal at the bond pad region was imaged (Fig. 3.S4A). PPX-X interface had a chromium undercut of 9 µm, whereas the parylene-C interface was undercut by 40 µm indicating either greater wettability or poor adhesion.

The second wet etch test used DI:HF:H_2O_2 3:3:1 to undercut the titanium sacrificial layer used in the polymer-on-polymer test structure. Unheated parylene-C and unheated PPX-

X structures were removed from etchant then rinsed for 10 minutes in DI before imaging. The PPX-X and titanium interface resulted in an undercut of ~0.4 mm after 60 minutes. Parylene-C structures were undercut >1.5 mm after 10 minutes (Fig. 3.S4B). Similar to the chromium results, the parylene-C interface had either greater wettability or poor adhesion to titanium.

3.4.5 Affect of IDE Geometry

An alternative interdigitated electrode geometry was also tested that had a metal width of 3 µm and a gap of 3 µm. Z_{lat} and Z_{trans} soak test results are included in supplementary material (Fig. 3.S5). Given that there was a difference in geometry, fewer number tested, and some anomalies in the Z_{lat} soak test results, we could not average these results with the original geometry. Dry impedance measurements of the two IDE geometries were fit to simple equivalent circuits to extract the capacitance values (Table 3.3). The 3/3 µm metal/gap width had a 14% greater capacitance than the 1.5/4.5 µm metal/gap. After soaking, Z_{trans} for the 3 µm gap devices also suggested a robust, viable coating and with little differentiation between variables. Z_{lat} had similar trends as seen in the devices with the 4.5-µm gap, such as improved high frequency performance for the PPX-X devices. Unheated PPX-X devices also showed the similar "rebound" effect as before. The most noticeable drop in impedance was the heated parylene-C IDEs relative to the 4.5 µm geometry. The parylene-C 3-µm gap IDEs had an average 1 kHz impedance of 36 kΩ versus 328 kΩ, which cannot be explained by geometry alone (Table B.S1). All 3-µm

gap IDEs had a lower average impedance relative to the 4.5-µm gap. A suggested explanation for this is discussed below.

Table 3.3. Dry Capacitance and Geometry

	1.5 µm trace, 4.5 µm gap Dry Capacitance, pF N = 14	3.0 µm trace , 3.0 µm gap Dry Capacitance, pF N = 12
No Heat Treatment[a]	22.5 ± 6.1	25.4 ± 1.5
Heat Treatment[b]	21.0 ± 4.6	24.0 ± 2.3
Average Capacitance	21.6 ± 5.4	24.6 ± 2.0

a. Impedance fit to a parallel resistor and capacitory. Average error = 6.6%.
b. Impedance fit to a constant phase element. Average error = 1.9%.

3.5 Discussion

Heat treatment of either parylene-C or PPX-X devices had a beneficial and long-term effect. The mechanism by which heat treatment (3 hrs, 140°C) improved the insulation performance of parylene-C was not directly tested but the evidence suggests a polymer-polymer and not a polymer-metal interaction. According to Table 3.2, heat treatment directly improved the interfacial parylene-C adhesion. Conversely the adhesion tests of parylene-C on metal showed no wet adhesion with heating (Table 3.1) so a polymer-metal interaction is highly unlikely. Others have shown that heat treatment and pressure improves parylene-parylene bonding, and suggested the cause was polymer chain entanglement (Kim and Najafi 2005). Heating may also quench hydrophilic free radicals on cleaved chain ends left over from the oxygen plasma cleaning step.

As for the heat treated PPX-X, previous research on the complementary layers of PPX-CH_2NH_2 and PPX-CHO showed that 140°C for 3 hrs provided enough energy to create an

imine bond. This reaction likely occurred here as well, but given that the processing conditions (exposure to highly acidic and basic solutions) may interfere we cannot be certain. In addition to the imine bond at the polymer-polymer interface, the PPX-X may be reacting with the chromium or native chromium oxide to form a metal-oxygen-polymer complex. For example, metal deposited onto oxygen-treated polystyrene surfaces formed a metal-oxygen-polymer complex as seen in XPS data (Burkstrand 1979) and correlated to improved adhesion (Burkstrand 1981). Researchers have also shown that a polymer deposited onto chromium, then heated, improved adhesion strength (Uddin, Ho et al. 2007).The chemical mechanism was suggested to be an electron transfer from the Cr to hydrophilic groups, resulting in the formation of a charge transfer complex. It could also be the interdifusion of the chromium oxide and polymer layers, but this would not explain the poor wet adhesion of parylene-C. Our adhesion test results (Table 3.1) showed moderate dry and wet metal adhesion after heating, which is consistent with this mechanism. The high frequency response of PPX-X also supports the theory that improved metal adhesion has occurred, otherwise metal delamination would have increased the capacitance and reduced the high frequency impedance modulus (Fig. 3.5A). Finally, we see from the wet metal etch experiments (Fig. 3.S4), the polymer-metal interface has reduced susceptibility to hydrolysis. While these data lack direct chemical mechanisms, there was a clear indication of having an improved PPX-X-chromium interface relative to parylene-C and chromium.

Unheated PPX-X devices showed a surprising reverse delamination response while soaking at 37°C. This cohort shared the same test chamber with all other variables and an antibacterial (NaN_3) was added to the 1X PBS, so these results could not have been a contamination issue. The breakpoint frequency decreased and magnitude increased in time. Breakpoint frequency and magnitude are used in organic-metal coating studies to track the temporal response of debonding or delamination (Yasuda, Yu et al. 2001; Akbarinezhad 2008). Since the trend is in reverse for PPX-X, we interpret this as a bonding mechanism. Furthermore, PPX-CHO and PPX-CH_2NH_2 bonding alone (formation of an imine bond) would not account for a robust, high frequency impedance. We suggest the cause of the increasing impedance is due in part by an interaction at the polymer-metal interface. Analytical chemistry techniques should be used in future studies to prove this hypothesis and discover the exact nature of this reaction. Fitting the impedance spectra to an equivalent circuit model was conducted and is discussed in Appendix C.

Regarding the time course of these results, the rapid rate of lateral impedance decline was not initially expected. However, this response agrees with observations made by others (Yasuda, Yu et al. 2001). Yasuda et al. found that water penetrates parylene-C at a rate of 15 microns/minute. This report also notes that water saturation in a thin film will occur in the first day and salt intrusion occurs on a slower time scale of days. Therefore, the saturation we see within the first day is not unreasonable and implies that, particularly for unheated devices, hydrolysis is the primary cause of delamination.

The results for PPX-X adhesion in Table 3.2 are not entirely consistent with those seen in Table 3.1. The differences in testing were the angle of separation and the amount of chemical exposure. The parylene-on-parylene test structures were processed similar to the interdigitated electrodes, which included exposure to diluted hydrofluoric acid. This strong acid may affect the aminomethyl or the aldehyde functional groups and therefore may prevent or mitigate the imine bond from forming after heating. Further investigation is needed to identify any process interactions.

Two IDE geometries were also presented. Z_{lat} was considerable lower for the heated CNTL group in the 3-µm gap geometry compared to the 4.5-µm gap. Other variables also had a lower impedance, although this difference was less pronounced. What can account for this difference? Since Z_{trans} was normal for the 3-µm gap geometry, and the dry value of Z_{lat} was normal, we rule out processing defects as a cause. We do not believe the Z_{lat} difference can be accounted for by the small sample size either, especially for the heated CNTL group (N=5). We believe the ultra-flexible structures (5-µm total thickness) revealed a mechanical design limitation (not a chemical one) by creating considerable stress during handling. The smaller gap increased the likelihood of micro-delamination, i.e. polymer-polymer separation, because of increased local stress between metal tracks. Small regions of micro-delamination could then account for this difference. The flexible 5-µm parylene structures resulted in almost 50% loss of test structures due to open-circuit failure. These two issues, inconsistent Z_{lat} in the tightly spaced design and frequent open circuits, highlight the fragility of large 5-µm parylene structures. Several improvements

could be made in future applications: (1) thinner metal structures will reduce local stress, and (2) a thicker substrate will increase mechanical strength.

In a multi-channel bioMEMS device, a large decline of the trace-to-trace impedance, Z_{lat}, will cause an increase in crosstalk noise or, in the worst case, create an electrical short. Susceptibility to crosstalk can be mitigated by proper design rules. One may increase the gap between traces, add a ground plane (if possible), or increase capacitance to the externally grounded extracellular space. Capacitive and crosstalk theory of interconnects allows us to model a variety of configurations (Walker 1990) and thereby reduce susceptibility. However, those techniques limit our design space and do not address the failure mechanism. Ideally we can mitigate the decline of Z_{lat} by choosing materials and surface chemistry that minimize delamination at the interfacial boundaries (Fig 3.1B). Our results for reactive parylene showed improved electrical properties, but there was a still a decline in the low frequency impedance modulus and even poorer performance when using a smaller gap size. Nonetheless, we expect heat treated parylene-C or PPX-X devices will work for 60 days or more *in vivo* if the proper design rules are chosen. We suggest using a wider gap than trace width, minimize mechanical strain on the device, and design an electrode with several orders of magnitude lower impedance relative to Z_{lat} and Z_{trans} of the interconnect.

3.6 Conclusions

We utilized an interdigitated electrode and impedance spectroscopy to investigate sensitive interfacial changes of parylene-C and reactive parylene nanofilms. Reactive parylene and heated parylene-C films used here show dramatic improvement in impedance over a broad frequency range. Furthermore, the reactive parylene nanofilms (PPX-CH_2NH_2 and PPX-CHO) showed 3-10X improvement between 100-100,000 Hz relative to the heated parylene-C. The advantage of the reactive parylene, we suggest, is derived from improving the wet metal adhesion. Finally, the concept of a hydrophobic, biocompatible barrier layer (parylene-C) in combination with a reactive interfacial layer (e.g. PPX-X) provides a useful strategy for researchers when seeking to design more robust non-hermetic implants.

Acknowledgements

The authors would like to thank David Sullivan, Joshua Jackson, and Luis Salas for their skillful technical assistance with electrical and mechanical tests. The staff at the Lurie Nanofabrication Facility provided excellent fabrication support. Funding for this research was provided in part by the National Institute for Biomedical Imaging and Bioengineering (NIBIB) Grant P41 EB002030 (Center for Neural Communications Technology) and the Department of Defense Multidisciplinary University Research Initiative (MURI) grant no. W911NF0610218.

References

Akbarinezhad, E. (2008). "Different approaches in evaluating organic paint coatings with electrochemical impedance spectroscopy SURFACE ENGINEERING." Surface Engineering **24**(4): 280-286.

Bauer, I., U. A. Russek, et al. (2004). Laser microjoining of dissimilar and biocompatible materials. Photon Processing in Microelectronics and Photonics III, San Jose, Ca, USA, SPIE.

Boukamp, B. A. (1986). "NONLINEAR LEAST SQUARES FIT PROCEDURE FOR ANALYSIS OF IMMITANCE DATA OF ELECTROCHEMICAL SYSTEMS." Solid State Ionics **20**(1): 31-44.

Burkstrand, J. M. (1979). "Formation of metal-oxygen-polymer complexes on polystyrene with nickel and chromium." Journal of Vacuum Science and Technology **16**(4): 1072-4.

Burkstrand, J. M. (1981). "Metal-polymer interfaces: adhesion and X-ray photoemission studies." Journal of Applied Physics **52**(7): 4795-800.

Chen H-Y, McClelland AA, Chen Z, Lahann J. "Solventless adhesive bonding using reactive polymer coatings". Analytical Chemistry. 2008;80(11):4119-24.

Grundmeier, G., W. Schmidt, et al. (2000). "Corrosion protection by organic coatings: Electrochemical mechanism and novel methods of investigation." Electrochimica Acta **45**(15-16): 2515-2533.

Jun, X., Y. Xing, et al. (2001). Surface micromachined leakage proof Parylene check valve, Piscataway, NJ, USA, IEEE.

Kim, H. and K. Najafi (2005). "Characterization of low-temperature wafer bonding using thin-film parylene." Journal of Microelectromechanical Systems **14**(6): pp. 1347-1355.

Klee, D., N. Weiss, et al. (2004). Vapor-Based Polymerization of Functionalized [2.2]Paracyclophanes: A Unique Approach Towards Surface-Engineered Microenvironments. Modern Cyclophane Chemistry. Weinheim, Wiley-VCH**:** p.463.

Kotzar, G., M. Freas, et al. (2002). "Evaluation of MEMS materials of construction for implantable medical devices." Biomaterials **23**(13): 2737-50.

Lahann, J., D. Klee, et al. (1998). "Chemical vapour deposition polymerization of substituted [2.2]paracyclophanes." Macromolecular Rapid Communications **19**(9): 441-445.

Lahann, J. (2006). "Reactive polymer coatings for biomimetic surface engineering." Chemical Engineering Communications **193**(11): 1457-1468.

Lahann, J., M. Balcells, et al. (2003). "Reactive polymer coatings: a first step toward surface engineering of microfluidic devices." Anal Chem **75**(9): 2117-22.

Li, W., D. Rodger, et al. (2005). "Integrated Flexible Ocular Coil for Power and Data Transfer in Retinal Prostheses." Conf Proc IEEE Eng Med Biol Soc **1**(1): 1028-1031.

Massey, L. K., Plastics Design Library., et al. (2003). Permeability properties of plastics and elastomers a guide to packaging and barrier materials. PDL handbook series. Norwich, N.Y., Plastics Design Library : William Andrew Publishing**:** xiv, 601 p.

Meyer, J. U., T. Stieglitz, et al. (2001). "High density interconnects and flexible hybrid assemblies for active biomedical implants." IEEE Transactions on Advanced Packaging **24**(3): 366-74.

Nandivada, H., H.-Y. Chen, J. Lahann. (2005). "Vapor-Based Synthesis of Poly[(4-formyl-<I>p</I>-xylylene)-<I>co</I>-(<I>p</I>-xylylene)] and Its Use for Biomimetic Surface Modifications." Macromolecular Rapid Communications **26**(22): 1794-1799.

Pornsin-Sirirak, N., M. Liger, et al. (2002). Flexible parylene-valved skin for adaptive flow control, Piscataway, NJ, USA, IEEE.

Rodger, D. C. and Y. C. Tai (2005). "Microelectronic packaging for retinal prostheses." IEEE Eng Med Biol Mag **24**(5): 52-7.

Sadhir, R. K., W. J. James, et al. (1981). "The adhesion of glow--discharge polymers, Silastic and Parylene to implantable platinum electrodes: results of tensile pull tests after exposure to isotonic sodium chloride." Biomaterials **2**(4): 239-43.

Schmidt, E. M., J. S. McIntosh, et al. (1988). "Long-Term Implants of Parylene-C Coated Microelectrodes." Medical & Biological Engineering & Computing **26**(1): 96-101.

Sharma, A. K. and H. Yasuda (1982). "Effect of glow discharge treatment of substrates on parylene-substrate adhesion." Journal of Vacuum Science and Technology **21**(4): 994-8.

Sheppard, N. F., D. R. Day, et al. (1982). "Microdielectrometry." Sensors and Actuators **2**(3): 263-74.

Suner, S., M. R. Fellows, et al. (2005). "Reliability of signals from a chronically implanted, silicon-based electrode array in non-human primate primary motor cortex." IEEE Trans Neural Syst Rehabil Eng **13**(4): 524-41.

Uddin, M. A., W. F. Ho, et al. (2007). "Interfacial adhesion of polymeric adhesive film on different surfaces in the fabrication of polymer photonic devices." Journal of Materials Science: Materials in Electronics **18**(6): 655-63.

van Westing, E. P. M., G. M. Ferrari, et al. (1994). "Determination of coating performance using electrochemical impedance spectroscopy." Electrochimica Acta **39**(7): 899-910.

Walker, C. S. (1990). Capacitance, inductance, and crosstalk analysis. Boston, Artech House.

Weaver, M. S., R. C. Kwong, et al. (2006). "Recent advances in phosphorescent OLEDs for small- and large-area-display sizes." Journal of the Society for Information Display **14**(5): 449-452.

Yamagishi, F. G. (1991). "Investigation of plasma-polymerized films as primers for parylene-c coatings on neural prosthesis materials." Thin Solid Films **202**(1): 39-50.

Yasuda, H., B. H. Chun, et al. (1996). "Interface-engineered parylene C coating for corrosion protection of cold-rolled steel." Corrosion **52**(3): 169-176.

Yasuda, H., Q. S. Yu, et al. (2001). "Interfacial factors in corrosion protection: an EIS study of model systems." Progress in Organic Coatings **41**(4): 273-279.

Yu, Q., J. Deffeyes, et al. (2001). "Engineering the surface and interface of Parylene C coatings by low-temperature plasmas." Progress in Organic Coatings **41**(4): 247-253.

Ziegler, D., T. Suzuki, et al. (2006). "Fabrication of flexible neural probes with built-in microfluidic channels by thermal bonding of parylene." Journal of Microelectromechanical Systems **15**(6): 1477-82.

CHAPTER 4 Fabrication of Advanced Polymer-based Neural Probes

4.1 Abstract

A new parylene-based microfabrication process is presented for neural recording, stimulation, and drug delivery applications. We introduce a large design space for electrode placement and structural flexibility with a six mask process. By using chemical mechanical polishing, electrodes may be created top-side, back-side, or on the edge of the device having three sides. Poly(3,4-ethylenedioxythiophene) (PEDOT) modified edge electrodes having an 85 μm^2 footprint (smallest reported to date) resulted in an impedance of 200 kΩ at 1kHz. Edge electrodes were able to successfully record single unit activity in acute animal studies. In complement to the parylene-C barrier film covering these structures, we used reactive parylene to interface the metal layer. Reactive nanofilms, comprised of PPX-CH_2NH_2 and PPX-CHO, were previously shown to have improved high frequency electrical insulation, which was further verified in the present study using this process.

4.2 Introduction

Parylene-C (poly-chloro-p-xylylene) has a litany of desirable material properties for use in a microfabricated implantable device. First, it has the highest certification level of biocompatibility, USP Class VI. This biocompatibility results from it being chemically inert and synthesized using a solvent-less polymerization process (Gorham 1966). Critically important to microfabrication, one can generate conformal, pinhole-free barrier films that are subsequently dry-etched using an oxygen plasma. For these reasons,

parylene-C has long been used in neurotechnology. It has been successful in coating microwires (Loeb, Bak et al. 1977) and micro-machined silicon arrays (Kim, Bhandari et al. 2008). Researchers have also microfabricated planar devices with a parylene-C substrate for use as a microfluidic device with recording capabilities (Takeuchi, Ziegler et al. 2005) and retinal stimulation arrays (Li, Rodger et al. 2005; Rodger and Tai 2005).

High quality interconnect insulation on flexible, parylene substrates cannot be assumed given that water and salts will rapidly diffuse to the various interfacial boundaries (Yasuda, Yu et al. 2001). Interfacial delamination due to poor wet adhesion of parylene on metal (Sharma and Yasuda 1982; Yasuda, Chun et al. 1996) and mechanical stress may create low impedance pathways for cross-talk noise or shunt loss. However, research on alternative parylene materials have promising results. Complementary reactive parylene layers of poly(4-aminomethyl-p-xylylene-co-p-xylylene) and poly(4-formyl-p-xylylene-co-p-xylylene) were discovered and synthesized in the laboratory of Joerg Lahann and found to improve adhesion in microfluidic applications (Chen, McClelland et al. 2008). In another study we evaluated these same materials, PPX- CH_2NH_2 and PPX-CHO, and found they improved wet metal adhesion and maintained higher electrical impedance relative to parylene-C (Seymour, Elkasabi et al. In Submission).

Previously we also microfabricated a parylene-C structure for biocompatibility testing (Seymour and Kipke 2007). In that prior study, we hypothesized that if a structural feature size is smaller than a reactive cell body (<7 μm), the resulting encapsulation would be mitigated by the prevention of cellular spreading. We investigated this

relationship between size and tissue reactivity using these parylene structures and found the cellular density around the sub-cellular feature was less than half of that around the probe shank. The biological response indicated that an optimal electrode design is a three-sided microelectrode on the edge of thin parylene substrate (5 μm thick). Implementing this design could not be done using previously reported fabrication techniques.

The broad objective of this work was to develop a parylene-based technology platform that enabled a greater design space and long-term insulation. The platform needed a dynamic structural range including a thick shank for insertion strength or reservoir capabilities, as well as thin, flexible structures where electrodes could be positioned. Electrode placement needed to be top-side, bottom-side, and even a three-sided edge position. The two critical challenges for meeting these design goals were (1) finding a planarization process that would enable the design of a two-sided electrode, and (2) incorporating an alternative interfacial material with better metal adhesion than parylene-C.

Here we report a method that meets these objectives in an efficient 6 mask process. We used chemical mechanical polishing (CMP) of parylene-C over SiO_2 to construct a planar insulation layer with electrode openings facing the wafer. CMP of parylene is rare, but one investigation showed that it was possible with parylene-N and resulted in a small increase in oxygen content (Yang, Zhao et al. 1997). We found the most significant challenge in polishing parylene was the prevention of delamination, which is discussed in

detail. Finally, we provide evidence that the reactive parylene films adequately insulated the metal interconnects and recording electrodes successfully recording neural spike activity in the rat neocortex.

4.3 Experimental

4.3.1 Microfabrication

The microfabrication for these structures required two masks and was conducted on 4" silicon wafers in the Lurie Nanofabrication Facility. For simplicity, we describe the process in eight steps (Fig 4.1a-h). A variety of neural devices were included in the mask set but the cross-section shown in the illustrated process was taken from a polytrode recording array that included a face-down electrode and an edge electrode (Fig 4.3a). **Fig 4.1a.** Five microns of high temperature (910°C) SiO_2 was deposited on a clean Si wafer. This layer served a dual purpose—it provided a sacrificial release layer and formed the face-down electrode/bond pad place holders. The Al mask was patterned using standard lithography and a wet etchant. The SiO_2 was patterned using the Al mask and a dry C_2F_6 plasma etch (LAM 9400, ICP). The Al was removed and the wafer cleaned after an etch depth of 2.8 μm was achieved. **Fig 4.1b.** An adhesion promoter, A-174, was dip coated on the wafer surface and rinsed. Next parylene-C was CVD polymerized (PDS2010, Specialty Coating System) on the oxide. Deposition was 4-μm thick. **Fig 4.1c.** Chemical mechanical polishing of parylene-C was primarily mechanical in nature until the SiO_2 was exposed, it is important to minimize shear stress in the parylene film. We discovered the likelihood of film delamination was reduced by using short polish steps (less than 4

minutes), dehydration baking between polishing, minimal carrier down force, and the prior use of an adhesion promoter. CMP was carried out with an IPEC Avanti 472 using a KOH silica slurry (0.2μ, pH=10, 10% solid load). Down pressure and back pressure gradually increased to a maximum of 3.5 psi and 1.5 psi, respectively. Parylene thickness was measured using interferometry (Nanospec/AFT, Nanometrics) and the calculated polish rate at full force was 220 nm/min. Between polish runs, wafers were cleaned using a scrubber and NH_4OH solution (OnTrak Systems, Inc) then baked at 90°C for 10 min in a nitrogen purge. Planarization results on a variety of features and spacing were tested (Fig 4.2). We achieved 2 μm lines and larger with sufficient uniformity. Since our metallization layer was 4200 Å, the 200-1200 Å edge features were sufficiently small for this process. **Fig 4.1d.** An oxygen plasma was used to clean and roughen the parylene-C undercoating (Jun, Xing et al. 2001; Pornsin-Sirirak, Liger et al. 2002). This plasma cleaning step occurred before each CVD step throughout the process to promote cleanliness and adhesion between layers. The first interfacial parylene layer, PPX-CH_2NH_2 was polymerized using custom built CVD equipment described previously (Nandivada, Chen et al. 2005), although it could be deposited with commercially available equipment as well. The target thickness of PPX- CH_2NH_2 was 100 nm (80-130 nm typical). The precursor was provided by Joerg Lahann (University of Michigan) with synthesis details described elsewhere (Klee, Weiss et al. 2004). Peaks at 3361 and 3301 cm^{-1} in the IR spectrum were used to confirm the presence of the N-H bonds after deposition. Electrode or bond pad openings in the PPX-CH_2NH_2 layer were created with a photoresist mask and an oxygen plasma etch (Plasmatherm 790). **Fig 4.1e.** Next, metal

lift-off (SPR220) was used to pattern the Cr/Au/Cr (100/4000/100 Å). The SPR220 resist surface was treated with TMAH to create an inhibition layer (Redd, Spak et al. 1999). Metal was deposited using an e-beam evaporator (Enerjet). The resist was removed with acetone. Following lift-off, wafers were immediately cleaned in fresh acetone, IPA, then spin rinsed for 5 minutes. **Fig 4.1f.** The second complementary layer of reactive parylene, PPX-CHO, was then deposited (80-130 nm) using same equipment and parameters as the first layer. Precursor synthesis details are described elsewhere (Lahann, Klee et al. 1998; Nandivada, Chen et al. 2005). The strong carbonyl stretch at 1688 cm^{-1} in the IR spectrum was used to confirm the presence of the aldehyde group after deposition. Next, parylene-C was deposited 2.5-µm thick (PDS2010). **Fig 4.1g.** Titanium was deposited 1000-Å thick (evaporator) and patterned (20:1:1 DI:HF:H_2O_2) to provide a mask during the final oxygen plasma etch of each structure (performed in Fig 4.1h). SU8-2025 (Microchem) was spun on to 40 µm thick and patterned to create the core of the probe shank. The SU-8 was cured for 15 min at 150°C. A final parylene-C layer was CVD polymerized (2 µm) which encapsulated the SU-8. We then spun an 80-µm thick AZ-9260 layer (2 step spin) and patterned to create a mask for the thick shank structures. Fine features were achievable on the thin parylene platform (5 µm thickness) using the Ti mask while low resolution features were masked with 9260 resist.

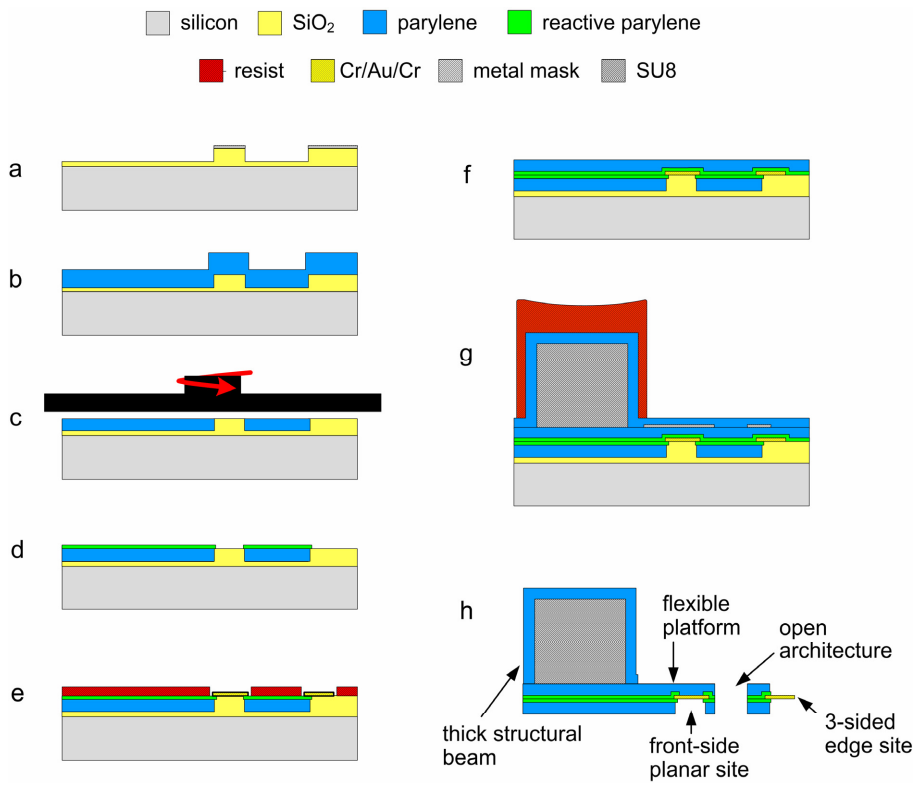

Figure 4.1 Microfabrication schematic of a parylene-based neural probe. (Cross-section is representative of device in Fig. 3a). (a) High temperature SiO_2 deposition. Pattern electrode openings with Al mask and dry etch. (b) Polymerize parylene-C. (c) CMP of parylene-C and SiO_2. (d) Polymerize thin layer of reactive parylene, PPX-CH_2NH_2. Pattern and etch electrode openings. (e) Liftoff metal deposition of Cr/Au/Cr. (f) Complementary layer of reactive parylene, PPX-CHO, and parylene-C. (g) Deposit Ti metal mask for fine structural features. Spin and pattern thick SU-8 structures. Deposit final parylene-C. Spin and pattern thick layer of 9260 resist. (h) O_2 plasma etch to define structures. Release devices in BHF. Key features of the design space are highlighted.

Fig 4.1h. The parylene stack was etched using an oxygen plasma to finalize the structural features. 9260 and the Ti mask were removed. Cr on the electrodes and bond pads was also wet etched to expose the Au beneath. Finally, the entire structure was released in buffered HF. SiO_2 removal required about 3 hours then devices were filtered and thoroughly rinsed.

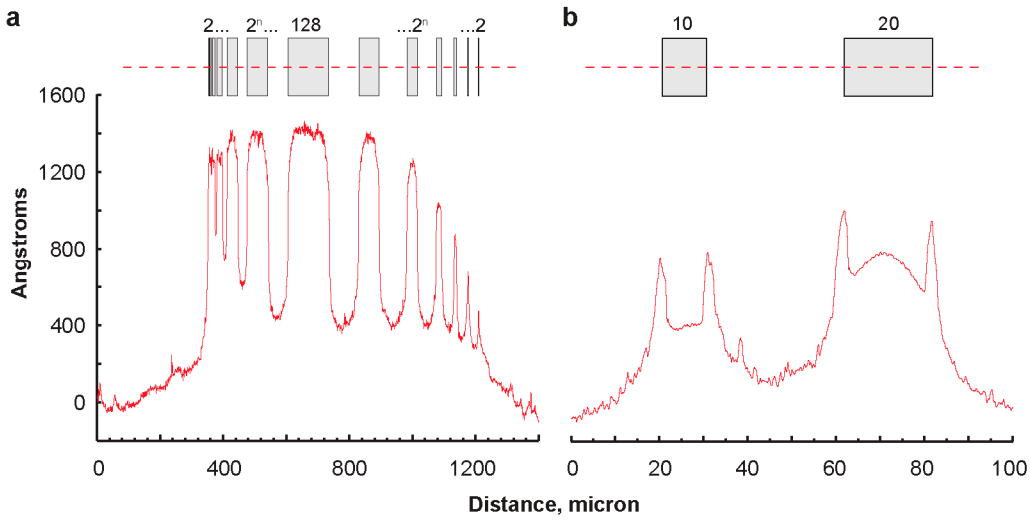

Figure 4.2 Chemical mechanical polishing of parylene over SiO_2. Profilometry results immediately after SiO_2 is exposed. (a) Profile of an increasing geometric series from 2 to 128 µm of the same track and space followed by the reverse series having wide spaces. Small isolated features achieved the greatest planarization. 2-µm features were achieved. (b) Profile of a 10 and 20-µm feature separated by 30 µm.

Heat Treatment and Assembly. Released devices were baked at 140°C for 3 hours to improve adhesion at the surface interfacial boundaries. This heat treatment was previously shown to create an imine bone at the PPX-CH_2NH_2 and PPX-CHO interface (Chen, McClelland et al. 2008) and to improve polymer-metal adhesion (Seymour, Elkasabi et al. In Submission). Neural devices were mounted on a custom PCB employing gold ball studs via thermosonic bonding (Meyer, Stieglitz et al. 2001). A protective coating of silicone (MED-4211, Nusil Technology) and epoxy were carefully applied to protect the bond region and PCB.

4.3.2 Electrode preparation and PEDOT-PSS electrodeposition

Variability in electrode impedance indicated organic residue or metal oxidation was an issue. We used chemical and electrochemical cleaning to lower impedance and reduce variability with a protocol developed for gold electrodes (Rafaela Fernanda Carvalhal 2005). Devices underwent a hot piranha etch for 10min followed by "electrochemical polishing" in a H_2SO_4 solution (0.5M). The polishing protocol called for 15 sweeps from -0.1 to 1.2V vs. SCE (100 mV/s). Finally each device was dipped into ethanol (95%) for 30 minutes before PEDOT deposition.

We selected poly(3,4-ethylenedioxythiophene) (PEDOT) and anion polystyrene sulfonate (PSS) to modify the microelectrodes and lower site impedance. Electropolymerization was carried out in a solution of 0.01M EDOT monomer (Sigma-Aldrich) and 0.1M PSSNa (Acros, M.W. 70000). A current density of 2 pA/μm^2 was applied (galvanostatic mode) until a charge density of 1 nC/μm^2 was achieved for each site. An Autolab PGSTAT 12 (Eco Chemie) with associated GPES software was used for electropolymerization control.

4.3.3 Electrochemical Impedance Spectroscopy

The electrochemical impedance measurements were performed using an Autolab PGSTAT 12 with associated FRA software. The spectral range used for testing interdigitated electrodes (Fig 4.6) was 100,000 to 1 Hz and with a single sinusoid at once.

When testing multiple electrode sites on a given device (Fig 4.5), 15 sinusoidal frequencies, spanning from 10,000 to 10 Hz, were applied at once to decrease measurement time. All voltage waveforms had an amplitude of 25 mV_{rms}. All impedance measurements were carried out in a Faraday cage in order to minimize external interference. Soak testing was conducted using phosphate buffered saline (PBS, 1X) between 55-65°C for one hour. The device under testing was lowered into a heated bath inside of the Faraday cage. Heated water was continually monitored and exchanged with water in a large bath surrounding the dish containing the saturated calomel (SCE) counter electrode, PBS, and test device.

4.3.4 Acute Surgery and Recordings

Neural probes were surgically implanted in male Sprague Dawley rats (300–400 g). Anesthesia was administered using intra-peritoneal injections of a mixture of ketamine, xylazine, and acepromazine. The craniotomy spanned approximately 4mm in the anterior–posterior direction, and 4 mm in the medial–lateral direction and was centered over the M1 and M2 motor cortex. A stereoscope was used to ensure a nearly orthogonal trajectory and avoid any visible surface blood vessels. Immediately before a probe was inserted via a manual stereotaxic drive, the anesthetized subject was moved to a Faraday cage, and then the probe tip was driven to a depth between 1 and 2 mm. All procedures strictly complied with the United States Department of Agriculture guidelines for the care and use of laboratory animals and were approved by the University of Michigan Animal Care and Use Committee.

Recorded neural signals were acquired using a TDT multi-channel acquisition system (Tucker-Davis Technologies). Neural electrophysiological recordings for all sixteen channels were amplified and bandpass filtered (450-5000 Hz) and sampled at 24 kHz. Objective classification of high speed neural activity was performed using an algorithm based on an automatic threshold and principal component analysis (Ludwig, Miriani et al. 2008).

4.4 Results and Discussion

4.4.1 Parylene-based neurotechnology platform

The CMP-parylene process we present above allowed us to create a variety of neural probes for recording, stimulation, drug delivery, and cell delivery (Fig 4.3a-d). The SU8 layer efficiently provides a third dimension to these structures, allowing for a stiff penetrating tine, large open channel, or small drug reservoir to be created in the SU8 lithography (Fig 4.3c,d,h). The large open channel may be used for passive drug delivery by loading with a degradable scaffold. Built-in electrodes on the channel-side may be used to electrically monitor the degradation rate of the scaffold (Fig 4.3c). As previously reported, the cell-delivery design can be used for stem-cell therapy (Purcell, Seymour et al. 2009). The parylene stack by itself created a thin, flexible structure for sensor placement or long interconnects. Highly flexible electrode arrays, such as electrocorticogram arrays, were also fabricated (not shown). An important goal of this research was to create an edge electrode effectively having three sides on a thin, flexible platform (Fig 4.3a,j). This feature allowed us to create the smallest footprint (85 μm^2) of

a functional recording electrode to date. This new electrode design should increase signal amplitude by reducing the spatial footprint while achieving a greater surface area than a conventional planar geometry would allow (Fig 4.3j). In addition to edge electrodes we provide several examples of single or double-sided electrode geometries (Fig 4.3e-i) that may also be useful when placed on a thin parylene platform.

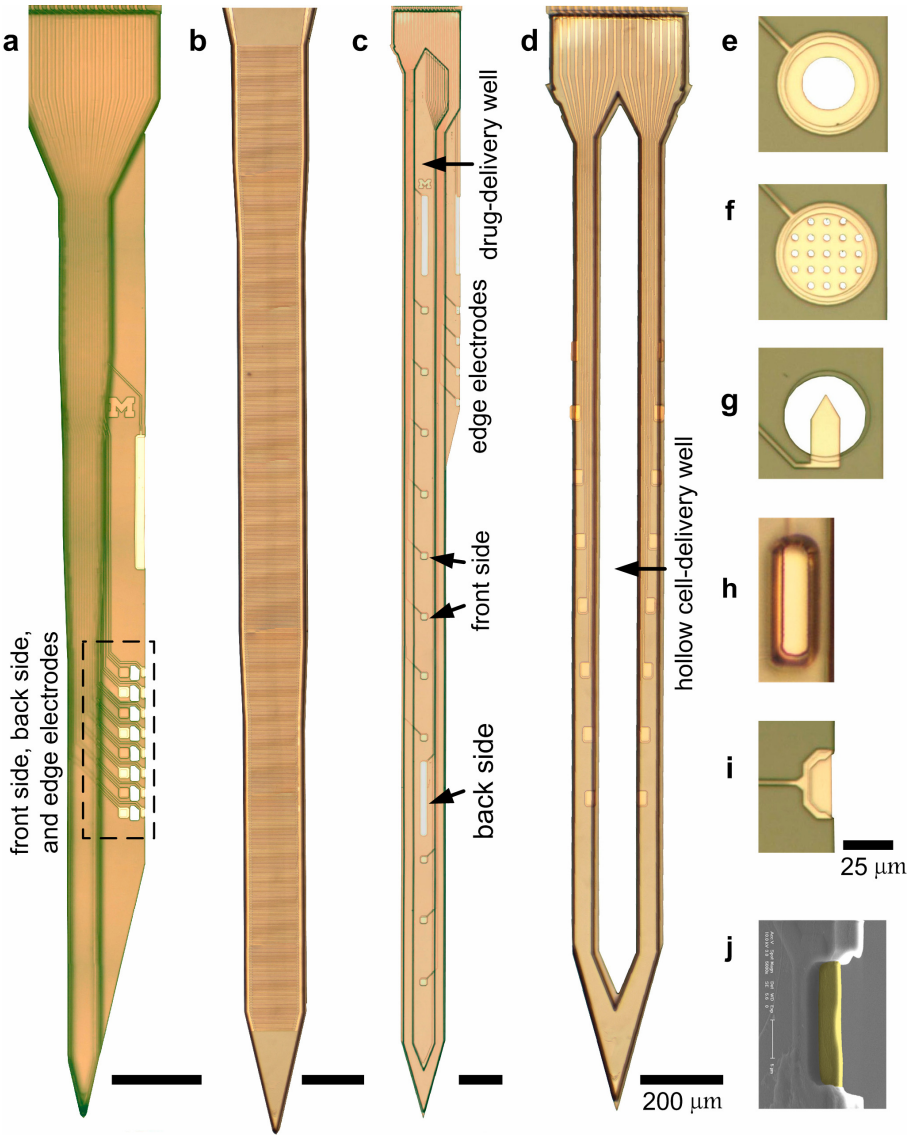

Figure 4.3 Illustration of the design space enabled by this novel parylene-CMP process. (a) Edge electrode array currently being tested for improved longevity based on sub-cellular geometry. (b) Interdigitated electrode used for EIS assessment of interconnect impedance or studying the time course of tissue encapsulation. (c) Open-channel design to be used for passive drug delivery. Channel can be loaded with drug scaffold. (d) Hollow-channel neural probe with 16 channels to be used for cell-based therapies. A wide variety of electrode options are available: (e) ring electrode, (f) sieve electrode, (g) cantilever electrode, (h) reservoir electrode, (i) large edge electrode, top-view, and (j) PEDOT-coated edge electrode, pseudo-colored SEM, viewed at 45°. 17 x 5 µm footprint. Scale = 200 (a-d) or = 25 µm (e-i). Background cropped for contrast (a-i).

4.4.2 Microelectrode Impedance

Previous work has shown that PEDOT can reduce the impedance modulus by nearly two orders of magnitude (Cui and Martin 2003). Our data show a similar reduction after PEDOT-PSS electrochemical polymerization. Gold microelectrodes had an average impedance modulus of 6.0 MΩ (at 1 kHz) which was reduced to 210 kΩ (Table 4.1). As expected, PEDOT electropolymerization also changed the morphology of the electrode surface. Surface roughness increased relative to gold thereby increasing the electrochemical surface area (Fig 4.4). A low charge density was chosen (1nC/μm^2 or 100mC/cm^2) because we observed an asymptotic decline of the impedance magnitude for larger charge densities, especially on planar sites. The ratio of impedance magnitude before and after PEDOT polymerization was greater with the edge geometry (Table 4.1). This is expected because the exposed edge thickens as more PEDOT is polymerized. The edge thickness increased from 0.4 μm to 1.1 μm after applying a charge density of 1nC/μm^2. After applying 2.5 nC/μm^2 on one site, the edge was measured to be 1.9 μm using electron microscopy. This represents a 20% increase in geometric surface area over the original 170 μm^2 (85 μm^2 per side). We expect a thicker edge dimension to be achievable, if desired, since charge densities between 1.3 and 28 nC/μm^2 have been reported (Cui and Martin 2003; Ludwig, Uram et al. 2006; Abidian and Martin 2008).

Table 4.1 Electrode Geometry and Impedance (1 kHz)

Geometry	Au Site[a], MΩ N = 48	PEDOT/PSS[b], kΩ N = 33	Post Implant[c], kΩ N = 15
Planar 17 x 17 µm	5.4 ± 3.7	240 ± 110	380 ± 82
Edge 17 x 5 x2 µm	6.0 ± 3.1	210 ± 64	460 ± 72

a. Electrodes cleaned using piranha etch, H_2SO_4 polishing, and EtOH
b. Galvanostatic deposition, current density = 2.5pA/µ^2, charge density = 1nC/µ^2
c. Cleaned in a proteolytic enzyme detergent

The increase in geometric and electrochemical surface area is critically important on this size scale. Thermal noise is proportional to the square root of the impedance modulus, so a surface modification technique is required to decrease the noise level in the recordings to discriminate unit activity. A number of other techniques to increase the electrochemical surface area of an electrode have been reviewed (Cogan 2008). In a few attempts to record single units with bare gold sites of either 280 µm^2 or 170 µm^2, we found the thermal noise to be dramatically higher than PEDOT modified sites.

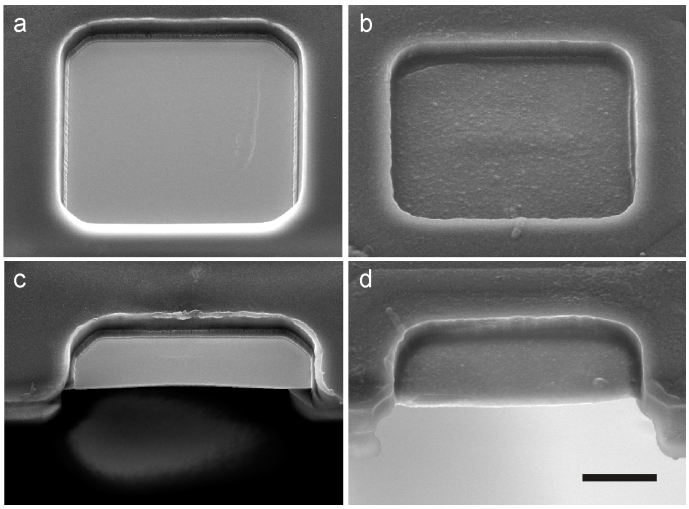

Figure 4.4 Example gold electrodes before and after PEDOT electrochemical deposition. (a) 280 μm^2 Au sites. (b) 280 μm^2 PEDOT/PSS grown at 2.5 $pA/\mu m^2$ for a total of $1nC/\mu m^2$. (c) 170 μm^2 three-sided Au electrode. Thickness was 0.5 µm. (d) PEDOT/PSS on a three-sided edge electrode (same current and charge density). Resulting thickness was 1.1 µm. Images taken at ~45°. Scale = 5µm.

Impedance spectroscopy was also performed on a PEDOT-modified neural recording array (N=11). Since the initial impedance values are so low (dominated by the electrode surface), this test would unlikely detect capacitive losses in the interconnects but is useful for determining the robustness of the PEDOT-PSS coatings. We performed a soak test in 1X PBS at 60°C over one hour. Results suggest the PEDOT-PSS is highly temperature dependent given the marked decline in modulus along with an accompanying phase shift (Fig 4.5). These values return to normal immediately following the test when impedance is measured at room temperature. These preliminary results on PEDOT-PSS stability are encouraging and agree well with previous work testing stability with CV sweeps (Cui and Martin 2003).

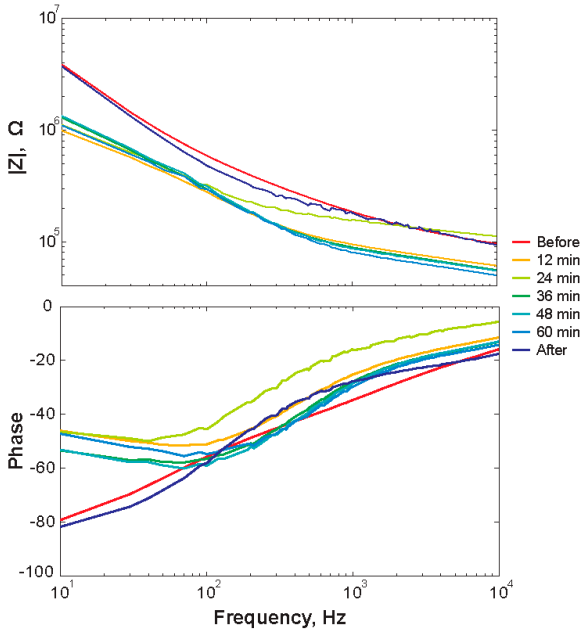

Figure 4.5 Bode plot over time for PEDOT-PSS electrodes before and during a 60°C soak in 1X PBS over one hour, N=11 . PEDOT/PSS electrodes were highly temperature sensitive. Before and after soak results were taken at 22°C within minutes of test.

4.4.3 Interconnect Impedance

High impedance electrical insulation was also investigated using a high temperature soak test (Fig 4.6). Impedance spectroscopy was used to measure the lateral or interfacial impedance of an interdigitated device (Fig 4.3b). Unlike the transverse impedance measurement through the parylene film, this measurement is highly sensitive to interfacial delamination (Sheppard, Day et al. 1982; van Westing, Ferrari et al. 1994). Bode plots show the response over one hour of soaking at 60°C and include the dry impedance values as well (Fig 4.6). As expected, the dry interfacial impedance was marked by a large modulus and a flat negative phase indicating a purely capacitive

response. The impedance modulus declines rapidly at low frequencies once the soak test begins, but still maintains a high value. The decline is asymptotic and the final magnitude at 60 minutes and 60°C remains much higher than the electrode impedance (Fig 4.5). The phase and the high frequency shift of the breakpoint indicate either micro-delamination or pores in the film being filled with water and salts. These results were as expected.

In a previous study, we presented soak data at 37°C for 60 days using the same parylene-C barrier layer and reactive parylene interfacial layers tested here albeit with a greatly simplified process. After one hour the impedance nearly dropped to its minimum value (Seymour, Elkasabi et al. In Submission) and actually increased slightly over the 60 day period. Other researchers have estimated that water molecules will diffuse 15-μm/min in parylene (Yasuda, Yu et al. 2001). Our results here also show a rapid, asymptotic decline of low frequency impedance as well. While the magnitude of the low frequency change is large, the final modulus remains stable and much higher than the electrode impedance. In the frequency range critical for neural recording and stimulation, 500-5000 Hz, the impedance modulus decline was small.

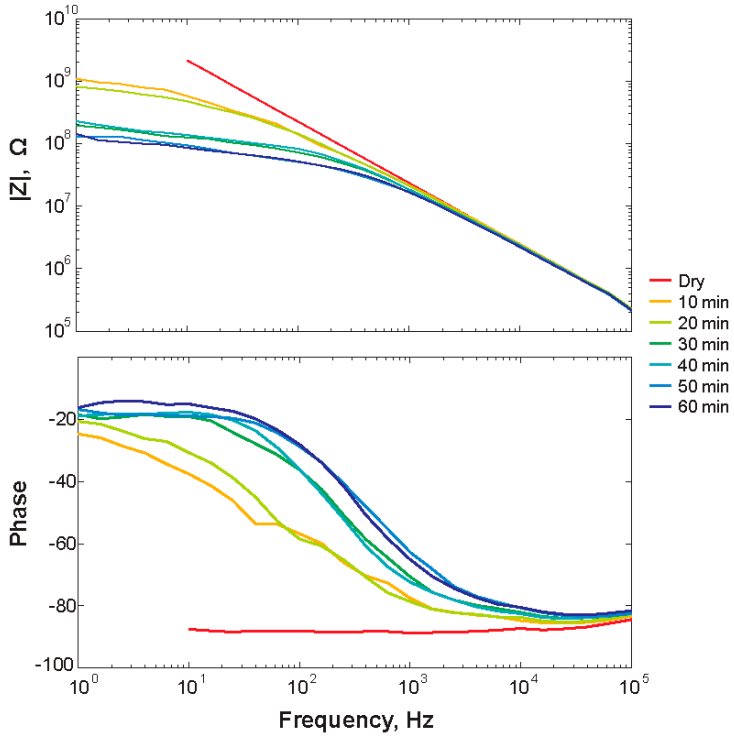

Figure 4.6 Bode plot over time for interconnects during a 60°C soak in 1X PBS. Interdigitated electrode response over one hour, N=3. IDE track and space was 2 µm wide. Length and width was 3 mm x 165 µm.

4.4.4 Neural Recordings

Acute animal recordings were conducted to evaluate the mechanical robustness and electrical function of the edge electrode design. A polytrode array (45-µm pitch) having electrodes on the face, back, and edge (Fig 4.7a) was tested for single unit activity and noise levels. Several planar and edge electrodes were tested without PEDOT polymerization and these had noticeably higher noise levels (55µV peak-peak). PEDOT-modified microelectrodes had an average noise level of 22µV peak-peak. Single unit activity was isolated with automated principal component analysis (Ludwig, Miriani et al.

2008). Planar sites had 25 isolatable units on 49 channels while edge electrodes had 57 units on 49 channels. Data was analyzed from 7 insertions in 2 animals using 2 separate arrays. These preliminary results also indicated a higher signal amplitudes on the edge electrodes relative to the conventional planar sites (Fig 4.7b, c). These devices remained functional and with low impedance (Table 4.1) following multiple insertions.

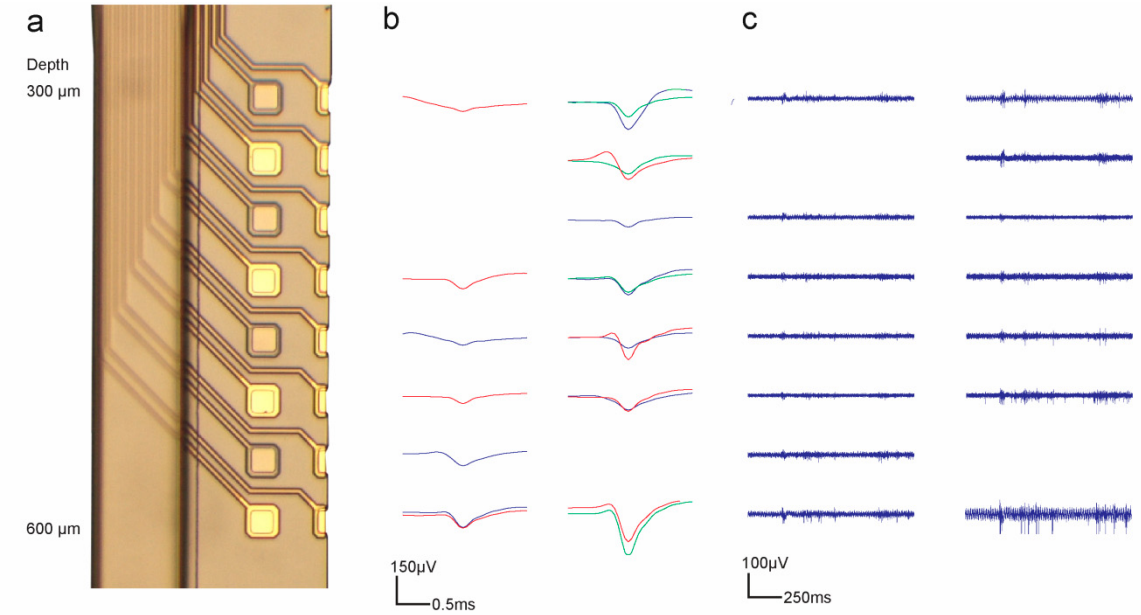

Figure 4.7 Sample in vivo data of planar and edge electrodes. (a) Edge array design has 8 planar sites (4 top-side, 4 back-side) and 8 edge sites on a 45-µm pitch. (b) Snippets extracted using an automated, objective sorted algorithm. (c) High-speed data filtered from 300 to 5000 Hz. PEDOT-PSS was deposited onto all sites (not shown).

4.5 Conclusion

We present a CMP-parylene process that was successfully employed for the microfabrication of a variety of neural probe designs. A large design space was created most notably by providing a dynamic range of structural stiffness and enabling electrode

placement on the front, back, or edge. Electrical spectroscopy data of the interconnects and microelectrodes resulted in stable impedance values in a high temperature soak test. Preliminary recording data indicates that the “subcellular” edge electrode design is functional and may be an improved alternative to the conventional planar microelectrode.

Acknowledgements

We are grateful to Prof. Joerg Lahann and Yaseen Elkasabi for providing the reactive parylene dimer and for conducting the CVD polymerization in their laboratory. Ning Gulari provided the critical idea of using CMP in this process and other helpful conversations. Dr. Hung-Chin Guthrie, Dr. Ramin Emami, and Dr. Pilar Herrera-Fierro shared their considerable CMP expertise which proved to be so vitally important. Dr. Kip Ludwig shared his method and software for automatic neural spike sorting. Dr. Mohammad Abidian and Eugene Daneshvar engaged in many helpful discussions regarding conductive polymers. We gratefully acknowledge support from the NIH P41 Center for Neural Communication Technology (EB002030) through the NIBIB.

References

Abidian, M. R. and D. C. Martin (2008). "Experimental and theoretical characterization of implantable neural microelectrodes modified with conducting polymer nanotubes." Biomaterials **29**(9): 1273-83.

Chen H-Y, McClelland AA, Chen Z, Lahann J. "Solventless adhesive bonding using reactive polymer coatings". Analytical Chemistry. 2008;80(11):4119-24.

Cogan, S. F. (2008). "Neural stimulation and recording electrodes." Annu Rev Biomed Eng **10**: 275-309.

Cui, X. and D. C. Martin (2003). "Electrochemical deposition and characterization of poly(3,4-ethylenedioxythiophene) on neural microelectrode arrays." Sensors and Actuators B (Chemical) **B89**(1-2): 92-102.

Gorham, W. F. (1966). "A New General Synthetic Method for Preparation of Linear Poly-P-Xylylenes." Journal of Polymer Science Part a-1-Polymer Chemistry **4**(12PA): 3027-&.

Jun, X., Y. Xing, et al. (2001). Surface micromachined leakage proof Parylene check valve, Piscataway, NJ, USA, IEEE.

Kim, S., R. Bhandari, et al. (2008). "Integrated wireless neural interface based on the Utah electrode array." Biomed Microdevices.

Klee, D., N. Weiss, et al. (2004). Vapor-Based Polymerization of Functionalized [2.2]Paracyclophanes: A Unique Approach Towards Surface-Engineered Microenvironments. Modern Cyclophane Chemistry. Weinheim, Wiley-VCH**:** p.463.

Lahann, J., D. Klee, et al. (1998). "Chemical vapour deposition polymerization of substituted [2.2]paracyclophanes." Macromolecular Rapid Communications **19**(9): 441-445.

Li, W., D. Rodger, et al. (2005). "Integrated Flexible Ocular Coil for Power and Data Transfer in Retinal Prostheses." Conf Proc IEEE Eng Med Biol Soc **1**(1): 1028-1031.

Loeb, G. E., M. J. Bak, et al. (1977). "Parylene as a Chronically Stable, Reproducible Microelectrode Insulator." Ieee Transactions on Biomedical Engineering **24**(2): 121-128.

Ludwig, K. A., R. Miriani, et al. (2008). "Employing a Common Average Reference to Improve Cortical Neuron Recordings from Microelectrode Arrays." J Neurophysiol.

Ludwig, K. A., J. D. Uram, et al. (2006). "Chronic neural recordings using silicon microelectrode arrays electrochemically deposited with a poly(3,4-ethylenedioxythiophene) (PEDOT) film." J Neural Eng **3**(1): 59-70.

Meyer, J. U., T. Stieglitz, et al. (2001). "High density interconnects and flexible hybrid assemblies for active biomedical implants." IEEE Transactions on Advanced Packaging **24**(3): 366-74.

Nandivada, H., H. Y. Chen, J. Lahann (2005). "Vapor-based synthesis of poly [(4-formyl-p-xylylene)-co-(p-xylylene)] and its use for biomimetic surface modifications." Macromolecular Rapid Communications **26**(22): 1794-1799.

Pornsin-Sirirak, N., M. Liger, et al. (2002). Flexible parylene-valved skin for adaptive flow control, Piscataway, NJ, USA, IEEE.

Purcell, E., J. Seymour, et al. (2009). "In vivo evaluation of a neural stem cell-seeded probe." Journal of Neural Engineering (In Press).

Rafaela Fernanda Carvalhal, R. Sanches F. Lauro T. K. (2005). "Polycrystalline Gold Electrodes: A Comparative Study of Pretreatment Procedures Used for Cleaning and Thiol Self-Assembly Monolayer Formation." Electroanalysis **17**(14): 1251-1259.

Redd, R., M. A. Spak, et al. (1999). Lithographic process for high-resolution metal lift-off, SPIE.

Rodger, D. C. and Y. C. Tai (2005). "Microelectronic packaging for retinal prostheses." IEEE Eng Med Biol Mag **24**(5): 52-7.

Seymour, J. P., Y. Elkasabi, et al. (In Submission). "Improved insulation performance in bioelectrical devices with a reactive parylene interface." Biomaterials.

Seymour, J. P. and D. R. Kipke (2007). "Neural probe design for reduced tissue encapsulation in CNS." Biomaterials **28**(25): 3594-607.

Sharma, A. K. and H. Yasuda (1982). "Effect of glow discharge treatment of substrates on parylene-substrate adhesion." Journal of Vacuum Science and Technology **21**(4): 994-8.

Sheppard, N. F., D. R. Day, et al. (1982). "Microdielectrometry." Sensors and Actuators **2**(3): 263-74.

Takeuchi, S., D. Ziegler, et al. (2005). "Parylene flexible neural probes integrated with microfluidic channels." Lab Chip **5**(5): 519-23.

van Westing, E. P. M., G. M. Ferrari, et al. (1994). "Determination of coating performance using electrochemical impedance spectroscopy." Electrochimica Acta **39**(7): 899-910.

Yang, G. R., Y. P. Zhao, et al. (1997). "Chemical-mechanical polishing of parylene N and benzocyclobutene films." Journal of the Electrochemical Society **144**(9): 3249-3255.

Yasuda, H., B. H. Chun, et al. (1996). "Interface-engineered parylene C coating for corrosion protection of cold-rolled steel." Corrosion **52**(3): 169-176.

Yasuda, H., Q. S. Yu, et al. (2001). "Interfacial factors in corrosion protection: an EIS study of model systems." Progress in Organic Coatings **41**(4): 273-279.

CHAPTER 5

Conclusions and Future Directions

5.1 Conclusions

Each of our Aims made progress in the ultimate goal of using microelectrodes for long-term, stable recording in the brain and may someday be extended to improve neural stimulation devices, peripheral devices, and biosensors. A brief summary of specific conclusions from the Aims is compiled here:

Aim 1. Design, fabricate, and evaluate sub-cellular neural probe geometry for reduced cellular encapsulation. (Seymour and Kipke 2006; Seymour and Kipke 2007)

- Microfabricated a novel parylene structure that introduced a "sub-cellular edge electrode" concept
- Presented the concept of an "open-architecture" neural probe but found little improvement in the tissue response inside the lattice structures
- Sub-cellular edge structure had less than half the cellular encapsulation measured at the shank

Aim 2. Evaluate the interfacial and bulk electrical properties of parylene-C versus reactive parylene materials to be used in an implantable microfabricated sensor. (Seymour, Chen et al. 2008; Seymour, Elkasabi et al. In Preparation)

- Heat treatment of parylene-C and reactive parylene greatly improved insulation of microfabricated bioelectrical devices
- Impedance of the heat-treated PPX-X devices was 800% greater at 10 kHz and 70% greater at 1Hz relative to heated parylene-C controls after 60 days
- Heated PPX-X devices had greater wet adhesion to metal

Aim 3. Develop a parylene-based technology platform that enables greater design space for neural probes, including implementation of the sub-cellular edge electrode. (Seymour, Langhals et al. 2008; Seymour, Langhals et al. In Preparation)

- Developed a novel technology platform for parylene-based neural probes enabling 3-dimensional structures and an edge electrode geometry
- Validated interconnect and electrode functionality in high temperature soak tests
- Validated the viability of sub-cellular edge electrodes in acute surgeries

5.2 Future Directions

In addition to the direct scientific and engineering findings highlighted above, the impact of this work was to lay the groundwork for many new experiments. Key future experiments include (1) long-term testing of the sub-cellular geometry (experimental details discussed below), and (2) validate the combination of passive drug-delivery with neural recordings as a new tool for reducing glial encapsulation or improving pharmaceutical drug screening. Other parylene-based neural probes such as cell-delivery devices (Purcell, Seymour et al. 2009) and ECoG arrays have also been fabricated and hopefully can be used as neuroscience research tools. Regarding Aim 2, we also believe the optimization of the materials and fabrication has only just begun. Analytical studies into the underlying chemical reaction of the polymer-metal boundary should provide further guidance regarding interfacial polymer materials. An even more robust non-hermetic packaging of bioMEMs devices is possible and likely to have high commercial and academic value.

Briefly, three important experimental designs are offered here that can validate the full potential of the sub-cellular electrode design. These experiments were designed with the assistance of Dr. Kip Ludwig (University of Michigan).

Experiment 1. Evaluate the recording performance and tissue response of the sub-cellular edge electrode (SEE) probe in chronic animal preparations. Using currently fabricated SEE probes, we will evaluate the recording performance of the SEE probe in chronic animal preparations. This study will evaluate the edge electrodes relative to nearby planar sites on a single multi-channel device (8 edge sites, 8 controls, 45-μm pitch). Histological evaluation will be conducted of each probe which will be left intact in the brain. This will also enable correlation testing between the electrophysiological metrics (SNR, number of units per channel, etc) and histological metrics (non-neuronal count, neuronal count, etc.).

Experiment 2. Evaluate the recording performance and stability of the open-architecture probe in chronic animal preparations. Using a similar probe design as in Experiment 1, this aim has a lattice design that is expected to improve tissue integration. This design will alter the mechanical device-tissue interface by lowering the structural stiffness of the lateral edge, decrease surface area, and redistribute tissue strain. As a result micromotion and the mechanical interface should be significantly improved, which will result in stable single unit activity (tested with cross-correlation of resolvable units). This will be the first study to evaluate functional response and tissue response to an "open" geometry.

Experiment 3. Evaluate the stimulation performance of the SEE probe in a long-term psychophysical study. Stimulation electrodes are geometrically large to reduce electrical impedance which lowers the power necessary to create a threshold current. New electrode materials have the capability to greatly reduce electrode impedance, however chronic tissue encapsulation is the limiting factor (Ludwig, Uram et al. 2006). Given the reduced tissue encapsulation evident by this design, we expect lower impedance when using the SEE in a chronic experiment. We will test current threshold in a psychophysical auditory study comparing our edge electrodes to nearby planar sites. This collaborative study with auditory experts (also at our institution) will test the SEE design in the central nucleus of the inferior colliculus (ICC) of the geunia pig. Outcome metrics will include electrical psychophysical detection thresholds, impedance spectroscopy, electrophysiology, and best frequency maps over time.

5.3 Concluding Remarks

Regardless of what future "displacing technologies" may arise, the microscale electrode will remain an important component of neuroscience research. The ability to batch fabricate high density devices for recording, stimulation, chemical sensing, and drug delivery will continue to be used in animal research, which requires low cost technology and large scale experiments. The microscale electrode is still maturing, and I believe will remain cheaper and more accessible than external modalities (e.g. optical, ultrasound, magnetic) for many years to come.

Nonetheless, today's principal investigators and graduate students must imagine what tomorrow's clinicians will be using to treat disease and augment lost function. Will neurotechnology be driven by new optical or chemical modalities, or will it simply be an evolution of current electrical devices? What materials will be used? How long will devices last? We hope that the scientific and engineering research presented here contribute to the ongoing debate of cause, effect, and progress.

References

Ludwig, K. A., J. D. Uram, et al. (2006). "Chronic neural recordings using silicon microelectrode arrays electrochemically deposited with a poly(3,4-ethylenedioxythiophene) (PEDOT) film." J Neural Eng **3**(1): 59-70.

Purcell, E., J. Seymour, et al. (2009). "In vivo evaluation of a neural stem cell-seeded probe." Journal of Neural Engineering(In Press).

Seymour, J. P., H. Chen, et al. (2008). Bioelectrical Performance of Microfabricated Parylene Substrates. Materials Research Society, San Francisco, CA.

Seymour, J. P., Y. Elkasabi, et al. (In Preparation). "Improved insulation performance in bioelectrical devices with a reactive parylene interface." Biomaterials.

Seymour, J. P. and D. R. Kipke (2006). "Fabrication of polymer neural probes with sub-cellular features for reduced tissue encapsulation." Conf Proc IEEE Eng Med Biol Soc **1**: 4606-9.

Seymour, J. P. and D. R. Kipke (2007). "Neural probe design for reduced tissue encapsulation in CNS." Biomaterials **28**(25): 3594-607.

Seymour, J. P., N. Langhals, et al. (2008). Sub-cellular edge electrode increases viewing angle and decreases arbor damage. Society for Neuroscience, Washington, D.C.

Seymour, J. P., N. Langhals, et al. (In Preparation). "Advancing microfabricated neural technology using chemical mechanical polishing to create a multi-sided electrode on a parylene structure " Biomedical Microdevices.

APPENDIX A

Supplemental Material for Chapter 2

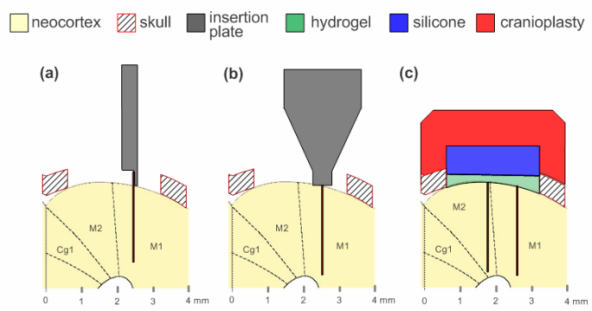

Fig. A-1. Illustration of surgical insertion method in a coronal cross-section. (a) The pre-assembled probe and insertion plate was mounted on a stereotaxic frame and manually driven into the target tissue. The probe head was secured with poly(ethyl glycol) and released with artificial cerebrospinal fluid. (b) The insertion plate was rotated and drove the probe head until approximately flush with brain to prevent tethering to the skull. (c) Surgical closure included a hydrogel (calcium alginate), followed by silicone (medical grade), and cranioplasty (PMMA).

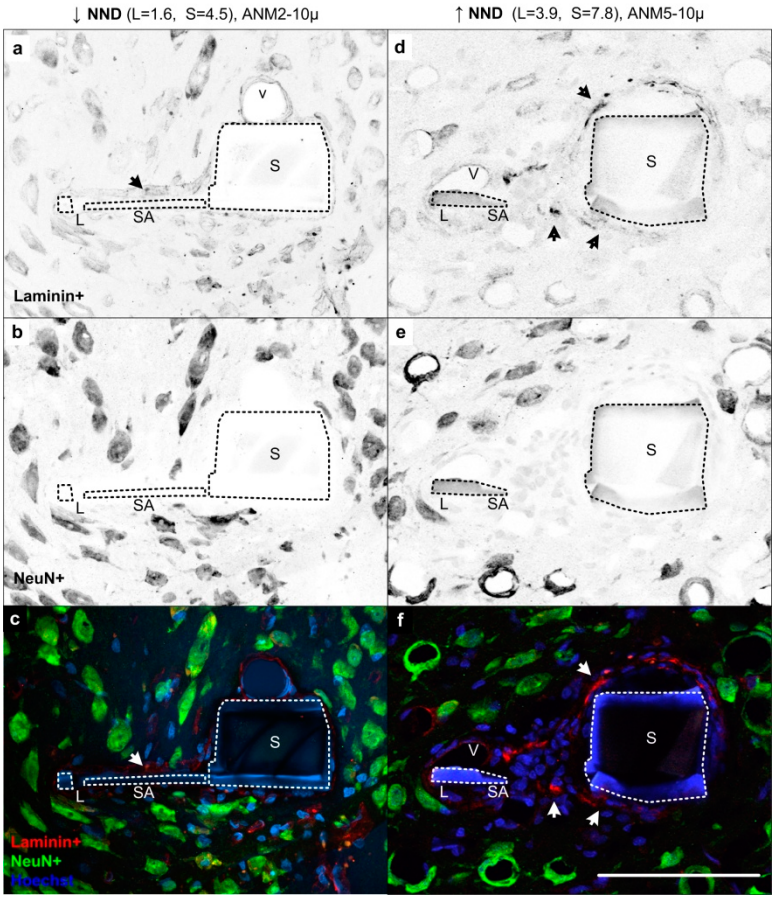

Fig. A-2. Inverted grayscale IHC images (a-b,d-e) showing laminin (a,d) and NeuN reactivity (b,e), and the corresponding RGB color image including Hoechst (c,f). (a-c) A low NND was characterized by faint or non-existent laminin staining. Laminin intensity was only mild, even in the presence of a support arm (SA) (arrow in a,c). (d-f) A high NND response typically had a wide band of laminin deposition at the probe interface but not at the lateral edge. Most characteristic of intense laminin staining was the presence of densely packed nuclei (arrows in d,f). Scale = 100 μm. 60X Obj.

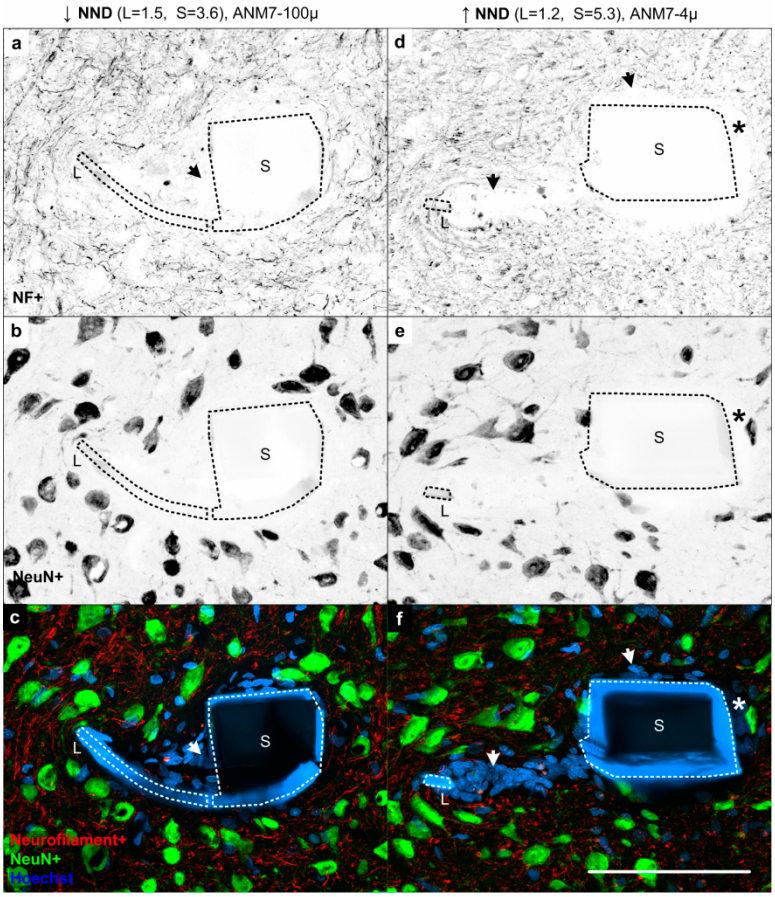

Fig. A-3. Inverted grayscale IHC images (a-b,d-e) showing neurofilament+ or NF (a,d) and NeuN reactivity (b,e), and the corresponding RGB color image including Hoechst counterstain (c,f). NF+ tissue was generally in closer proximity to the device interface than neuronal nuclei. NF staining formed a band around dense nonneuronal nuclei (arrows a-f). Elongated neuronal nuclei were common when nuclei were adjacent to the structure (* in d-f). Scale = 100 µm. 60X Obj.

APPENDIX B

Supplemental Material for Chapter 3

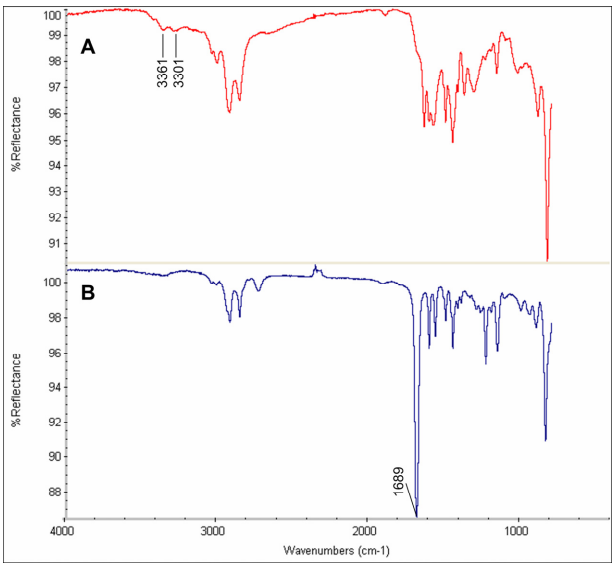

Fig. B.S1. Fourier Transform Infrared Spectroscopy of PPX-X nanofilms after deposition. (A) The C-NH_2 bonds in PPX-CH_2NH_2 were identified by 3361 and 3301 cm^{-1} peaks, and (B) The C=O bond in PPX-CHO was identified by a 1688 cm^{-1} peak. Note the absence of the C-Cl aromatic bond at 1060 cm^{-1}, which is characteristic of parylene-C.

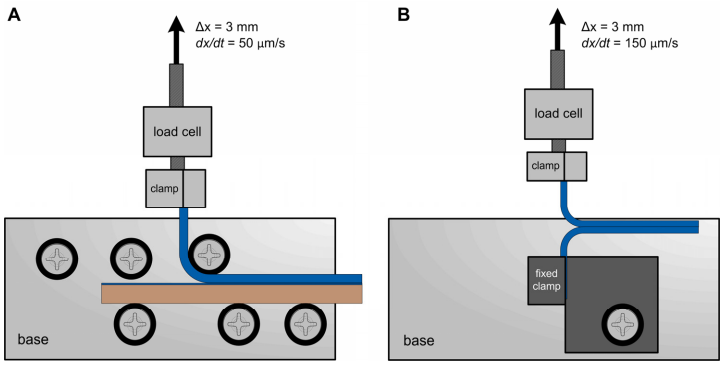

Fig. B.S2. Pull-test apparatus. (A) Parylene-on-metal structure was peeled at 90 degrees. (B) Parylene-on-parylene structure was peeled at 180 degrees.

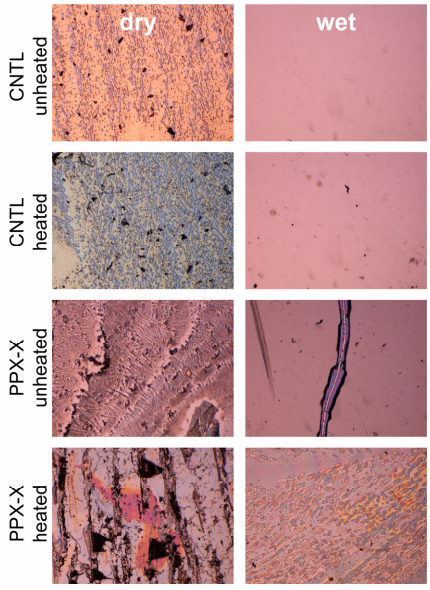

Fig. B.S3. Images of remnant films after adhesion testing.

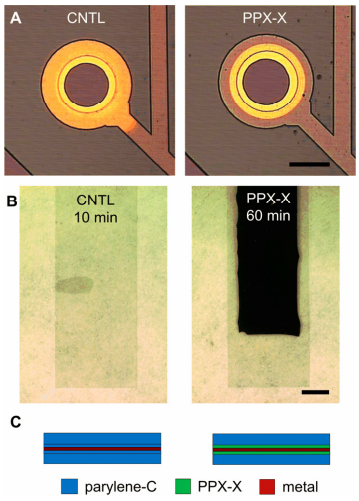

Fig B.S4. Wet etch testing. (A) Chromium undercut of a parylene-C interface (left) and a PPX-X interface (right). Image taken after 8 sec wet etch in CR-14. Scale = 50 µm. (B) Titanium undercut of a parylene-C after 60 min (left) or PPX-X interface after 10 min in HF acid solution. Scale = 1 mm. (C) A cross-section of materials in each sample is shown. Samples were not heated.

Table B.S1. 1kHz Impedance of Variables by Geometry Before and After Soaking

		1.5/4.5 µm trace/gap		3/3 µm trace/gap	
		N	Dry 1kHz $\|Z_{lat}\|$, MΩ	N	Dry 1kHz $\|Z_{lat}\|$, MΩ	Ratio
Before Soak	Parylene-C Unheated	3	6.5 ± 3.3	3	6.4 ± 0.6	1.0
	Parylene-C Heated	3	7.4 ± 4.0	5	7.2 ± 0.3	1.0
	PPX-X Unheated	5	9.6 ± 1.5	2	6.9 ± 0.1	1.4
	PPX-X Heated	3	9.1 ± 2.4	2	6.0 ± 0.2	1.5
	Average	14	8.4 ± 2.7	12	6.8 ± 0.6	1.2
1Day after Soak	Parylene-C Unheated	3	.026 ± .005	3	.017 ± .007	1.6
	Parylene-C Heated	3	.328 ± .586	5	.036 ± .015	9.2
	PPX-X Unheated	5	2.28 ± .93	2	.952 ± 1.11	2.4
	PPX-X Heated	3	.021 ± .012	2	.005 ± .001	4.3
	Average	14	.937 ± 1.21	12	.179 ± .492	5.2

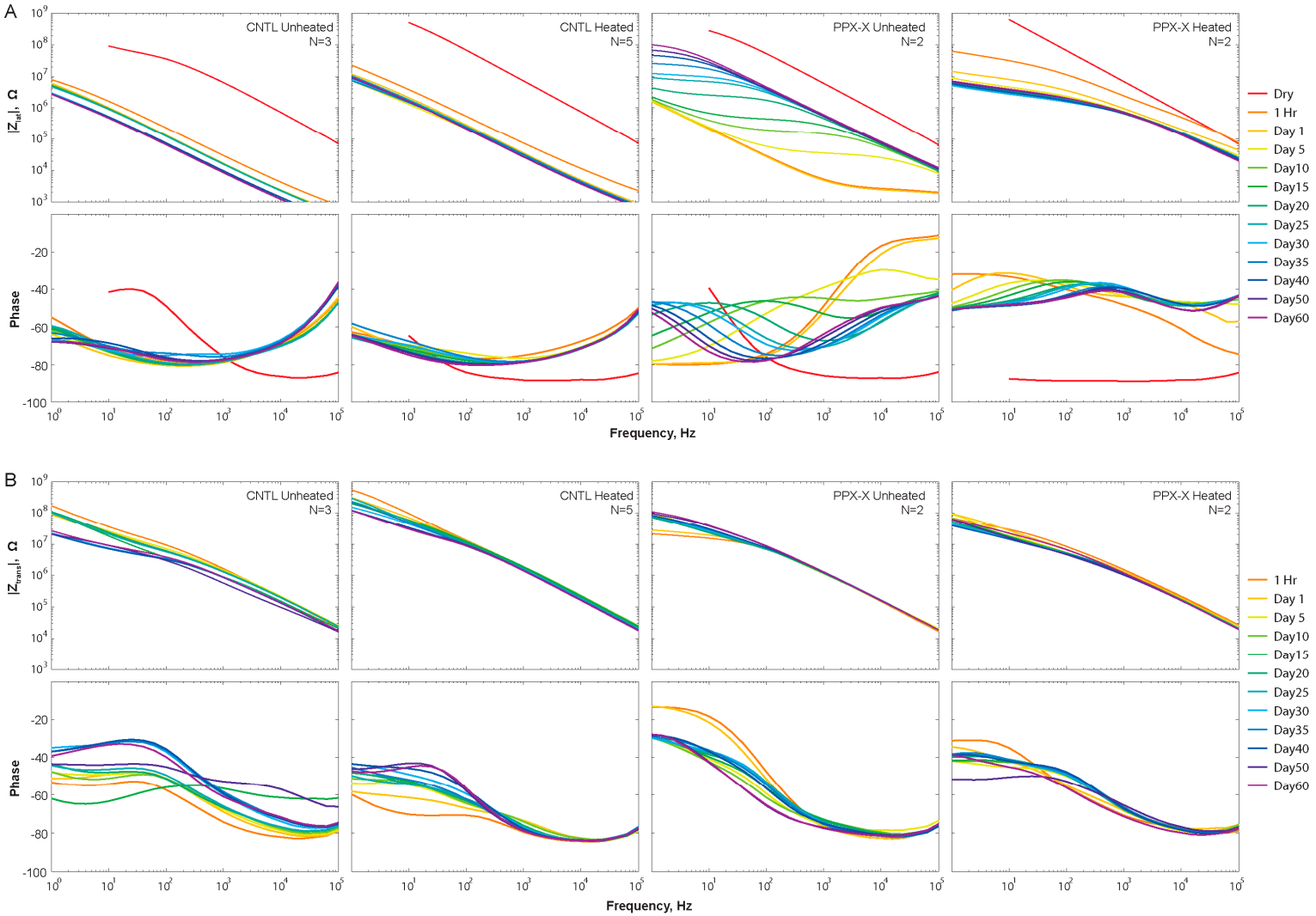

Fig B.S5. Bode plots displaying the temporal response to soaking in 1X PBS at 37°C for the alternative geometry having a 3 µm gap. (A) Lateral impedance, Z_{lat}, and (B) transverse impedance, Z_{trans}. Variables from left to right are CNTL unheated, CNTL heated, PPX-X unheated, and PPX-X heated. Z_{lat} increased over time for unheated PPX-X.

APPENDIX C

Circuit Model for Lateral Impedance Response

Impedance spectra are frequently interpreted in terms of an "equivalent circuit model" or ECM based on a plausible physical model. Three ECMs were used to fit the EIS data discussed in Chapter 3 (Fig. C.1).

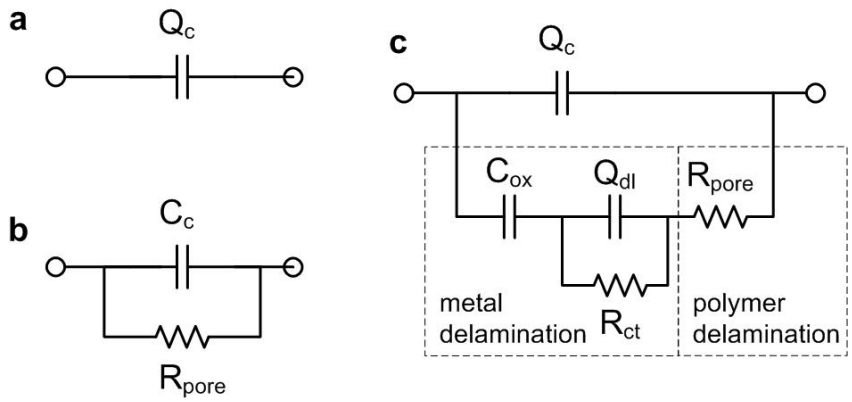

Fig. C.1. Electrochemical impedance spectroscopy data was fit to these three equivalent circuit models .(a) Heated samples fit best to a constant phase element before soaking began. Average error of 1.9%. (b) Unheated samples fit best to an RC circuit before soaking began. Average error of 6.6%. (c) Circuit with the best fit of heated and unheated samples during soaking over 60 days. Components on the lower left were most likely related to metal delamination and R_{pore} were most likely related to polymer-polymer delamination.

The dry impedance measurements were fitted using Boukamp's program, EQUIVCRT (Boukamp 1986). The soaking impedance spectra were interpreted on the basis of Fig. C.1c using EIS Spectrum Analyzer software (28.01.2008). The later package is less widely used than Boukamp's software but has an improved graphical interface and was more stable. Both EIS fitting packages resulted in similar values (~10%). Analysis of the

impedance measurements were performed between 1 Hz and 100 kHz. Extracted capacitance values of dry IDEs were used to verify the test structures had similar geometries and thus useful for comparison (Table 3.3). Dry IDEs not heat treated fit best using a parallel resistor and capacitor (Fig. C.1b). Heated IDEs were fit to a simple constant phase element (CPE) (Fig. C.1a).

The objective of the impedance circuit fitting was to illuminate the possible physical mechanisms corresponding to the response of impedance over time. For example, the differences in heated versus unheated dry lateral impedance suggest that water is still present at the metal interface. Heating the IDEs drives the water out of the device and effectively makes the resistive component an open circuit.

Selection of the equivalent circuit model was based on trial and error testing of ECMs found in the organic-metal coatings literature. Two fundamental rules when choosing the ECM were (1) the model should be as simple as possible while maximizing accuracy, and (2) the model components should have a physical interpretation (Bonora, Deflorian et al. 1995).

Predictions and Implications of ECM for Soak Testing

The model chosen in Fig. C.1c is similar to a circuit used in other organic-metal systems (Aziz-Kerrzo, Conroy et al. 2001; Bastos, Ostwald et al. 2004), except it included the addition of C_{ox}. Q_c corresponds to the coating capacitance, R_{pore} is the resistivity of the coating, Q_{dl} corresponds to the double layer capacitance that forms after micro-

delamination at the metal interface, R_{ct} is the charge transfer resistance. C_{ox} was added because a third time constant became apparent on all four variables especially if the low frequency was further measured lowered to 100 mHz. C_{ox} represents the presence of the native chromium oxide.

Table C.1. ECM component values at Day 1 and Day 60.

	Day 1				Day 60			
	PPX-X Heated	PPX-X Unheated	CNTL Heated	CNTL Unheated	PPX-X Heated	PPX-X Unheated	CNTL Heated	CNTL Unheated
C_{ox}	2.02E-08	5.97E-08	1.05E-08	2.71E-08	8.25E-09	4.11E-08	7.59E-09	2.33E-08
Error	19.1	3.0	13.6	8.3	10.0	2.3	15.5	6.3
R_{pore}	2.90E+06	1.31E+04	2.91E+04	7.21E+02	2.17E+07	1.95E+07	4.96E+04	7.15E+02
Error	7.6	2.0	10.8	9.1	12.0	5.4	68.2	9.0
R_{ct}	8.92E+07	1.65E+06	4.97E+07	4.50E+06	3.71E+08	4.15E+07	1.31E+08	5.82E+06
Error	10.2	102.2	99.1	17.5	6.5	23.8	25.0	16.5
Q_c	8.97E-11	4.04E-08	6.73E-10	7.04E-09	9.90E-11	1.02E-08	5.48E-09	7.03E-09
Error	2.5	6.2	6.0	8.3	1.2	2.6	3.1	9.6
N_c	0.91	0.55	0.85	0.76	0.91	0.72	0.67	0.88
Error	0.2	1.1	0.6	1.3	0.1	0.5	0.4	1.0
Q_{dl}	1.99E-08	3.21E-07	5.59E-09	1.13E-07	1.17E-09	2.06E-07	8.42E-09	6.24E-08
Error	4.4	3.8	3.3	2.6	1.8	9.5	2.5	5.6
N_{dl}	0.43	0.72	0.76	0.78	0.51	0.64	0.81	0.81
Error	1.8	0.8	0.4	0.3	0.6	3.6	0.4	0.7

As with the Bode plots shown in Fig. 3.5, the circuit modeling results indicated that the parylene-C samples were relatively stable after the first hour of soaking (Table C.1, Fig. C.2). Heated PPX-X had a modest decline in the components Q_{dl} and C_{ox}, and a slight

increase in R_{ct}. If the model is accurate, then this suggested limited bonding at the polymer-metal interface was occurring. Unheated PPX-X had a significant decline in Q_c and Q_{dl} including a slight decline in Cox. Also R_{pore} and R_{ct} increased considerably. The combination of these changes suggest that unlike the heated PPX-X, there was bonding at both the polymer-metal and polymer-polymer interface. After 60 days, the component value most different between heated and unheated PPX-X was Q_c. No explanation for this difference has been found. If it were a result of some remnant delamination then why were the other component values so similar?

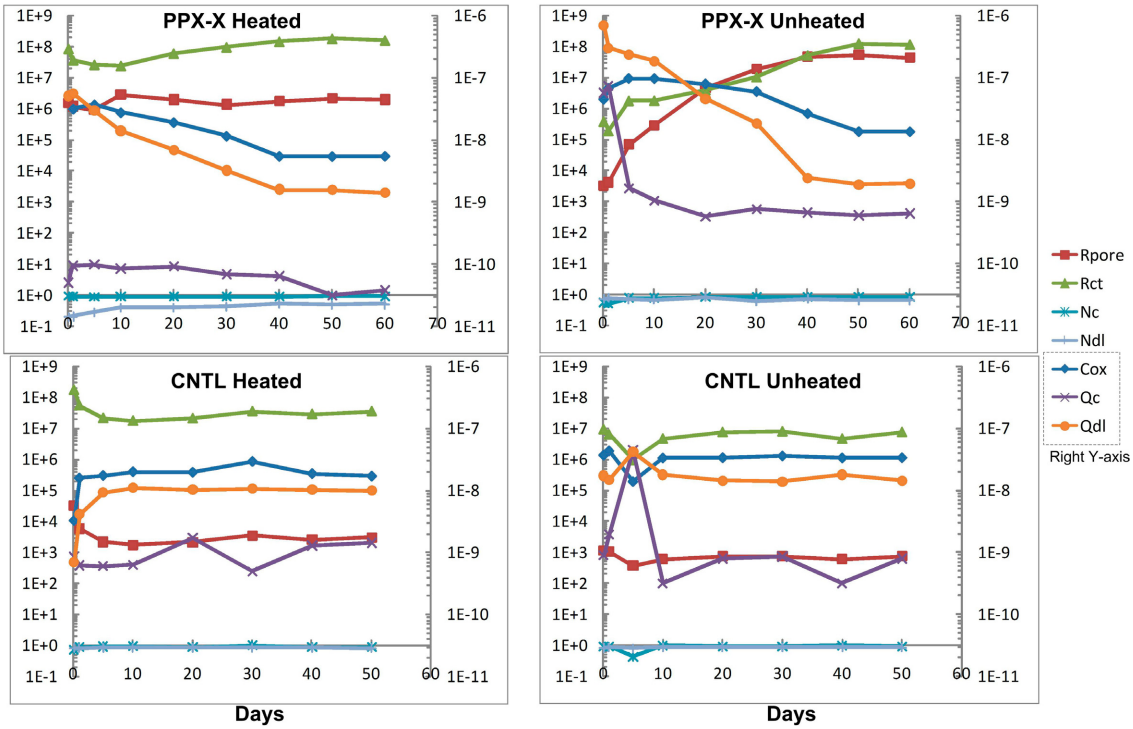

Fig. C.2. Circuit component values over time for each variable. Data is one example from each cohort.

The component value with the greatest correlation to the lateral impedance over time is R_{pore}, which as shown in Fig. C.1c is believed to be related to the polymer-polymer interface. This interpretation is at odds with the adhesion test results from Table 3.1 and 3.2 which suggested the PPX-X devices should have improved metal adhesion. No explanation for this difference is offered, however, we believe the adhesion testing has more credibility than the circuit modeling.

Interpreting the lateral impedance ECM results was more difficult than the dry test ECM. Accuracy of fitting to this circuit model is limited by several factors. First, the low frequency measurement was only 1 Hz, which especially limits the accuracy of the resistive components in the model. Second, the IDE structure is inherently more complex than a typical coating study using transverse impedance measurements. There are two interfaces in an IDE (one interface at each electrode), therefore, the circuit should be mirrored but this would make the solution indeterminate. A simplified half-circuit version was chosen (Fig. C.1c). Also, some of the field lines interact with the solution which may confound the results.

Nyquist plots provide an alternative view of the PPX-X lateral impedance. Heated PPX-X devices had only a minor increase in impedance over time with little shape change. Unheated PPX-X devices revealed a growing semi-circular arc over time (Fig. C.3). This growing arc corresponds well with the increase in R_{pore} found in the circuit modeling. The intercept of this arc with the real axis is equal to the resistance in the corresponding RC circuit, believed to be Q_c and R_{pore}.

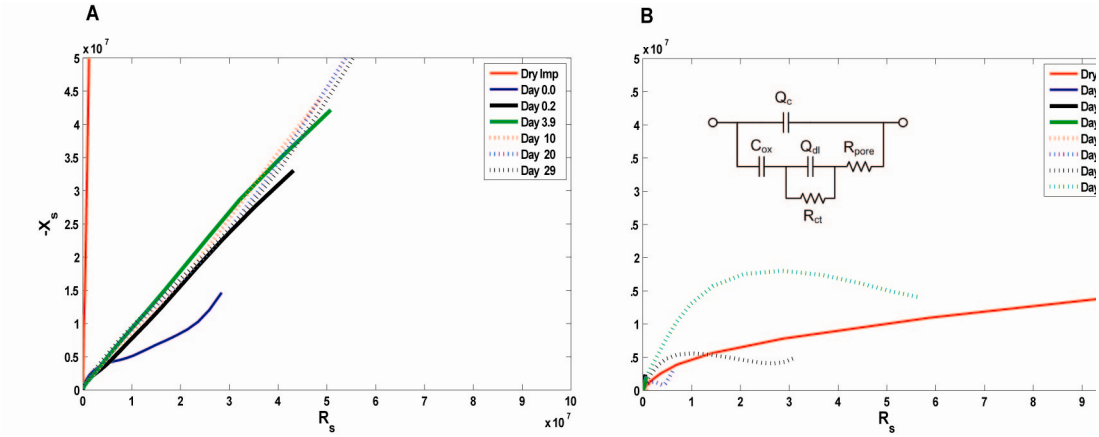

Fig. C.3. Nyquist plots for the PPX-X lateral impedance.(A) Heated PPX-X had relatively little impedance increase over time. (B) Unheated PPX-X samples impedance increased dramatically. Notice at least one RC time constant or semi-circular arc grew over time.

References

Aziz-Kerrzo, M., K. G. Conroy, et al. (2001). "Electrochemical studies on the stability and corrosion resistance of titanium-based implant materials." Biomaterials **22**(12): 1531-1539.

Bastos, A. C., C. Ostwald, et al. (2004). "Formability of organic coatings - An electrochemical approach." Electrochimica Acta **49**(22-23 SPEC ISS): 3947-3955.

Bonora, P. L., F. Deflorian, et al. (1995). EIS study of organic coating performance, Switzerland, Trans Tech Publications.

Boukamp, B. A. (1986). "NONLINEAR LEAST SQUARES FIT PROCEDURE FOR ANALYSIS OF IMMITANCE DATA OF ELECTROCHEMICAL SYSTEMS." Solid State Ionics **20**(1): 31-44.